



**FATIGUE BEHAVIOR OF FORGED INCONEL 718
INCLUDING THE EFFECTS OF AXIAL/TORSIONAL
LOADING AND HIGH TEMPERATURE**

VÍTOR CAIXETA FALLIERI NASCIMENTO

**DISSERTAÇÃO DE MESTRADO EM CIÊNCIAS MECÂNICAS
DEPARTAMENTO DE ENGENHARIA MECÂNICA**

FACULDADE DE TECNOLOGIA

UNIVERSIDADE DE BRASÍLIA

**UNIVERSIDADE DE BRASÍLIA
FACULDADE DE TECNOLOGIA
DEPARTAMENTO DE ENGENHARIA MECÂNICA**

**FATIGUE BEHAVIOR OF FORGED INCONEL 718
INCLUDING THE EFFECTS OF AXIAL/TORSIONAL
LOADING AND HIGH TEMPERATURE**

VÍTOR CAIXETA FALLIERI NASCIMENTO

**Orientador: Prof. Fábio Comes de Castro, PhD. (ENM/UnB)
Coorientador: Prof. José Alexander Araújo, D.Phil (ENM/UNB)**

DISSERTAÇÃO DE MESTRADO EM CIÊNCIAS MECÂNICAS

**PUBLICAÇÃO PPGENM-DM XXX/20XX
BRASÍLIA-DF, 30 DE MARÇO DE 2022.**

**UNIVERSIDADE DE BRASÍLIA
FACULDADE DE TECNOLOGIA
DEPARTAMENTO DE ENGENHARIA MECÂNICA**

**FATIGUE BEHAVIOR OF FORGED INCONEL 718
INCLUDING THE EFFECTS OF AXIAL/TORSIONAL
LOADING AND HIGH TEMPERATURE**

VÍTOR CAIXETA FALLIERI NASCIMENTO

DISSERTAÇÃO DE MESTRADO ACADÊMICO SUBMETIDA AO DEPARTAMENTO DE ENGENHARIA MECÂNICA DA FACULDADE DE TECNOLOGIA DA UNIVERSIDADE DE BRASÍLIA, COMO PARTE DOS REQUISITOS NECESSÁRIOS PARA A OBTENÇÃO DO GRAU DE MESTRE EM ENGENHARIA MECÂNICA.

APROVADA POR:

Prof. Fábio Comes de Castro, PhD. (ENM/UnB)
Orientador

Prof. Waldek Bose Filho, PhD. (USP)
Examinador Externo

Prof. Jorge Luiz de Almeida Ferreira, PhD. (ENM/UnB)
Examinador Interno

BRASÍLIA, 30 DE MARÇO DE 2022.

FICHA CATALOGRÁFICA

VÍTOR CAIXETA FALLIERI NASCIMENTO

Fatigue Behavior of Forged Inconel 718 Including the Effects of Axial/Torsional Loading and High Temperature

[Distrito Federal] 2022.

x, 97p., 201x297 mm (ENM/FT/UnB, Mestre, Engenharia Mecânica, 2022)

Dissertação de Mestrado - Universidade de Brasília

Faculdade de Tecnologia

Departamento de Engenharia Mecânica

- | | |
|----------------------------|---------------------|
| 1. Axial/Torsional Fatigue | 2. High Temperature |
| 3. Critical Plane Models | 4. Inconel 718 |

I. ENM/FT/UnB

II. DM XXX/2022

REFERÊNCIA BIBLIOGRÁFICA

VÍTOR CAIXETA FALLIERI NASCIMENTO (2022) Fatigue Behavior of Forged Inconel 718 Including the Effects of Axial/Torsional Loading and High Temperature. Dissertação de Mestrado em Ciências Mecânicas, Publicação DM-XXX/20XX, Departamento de Engenharia Mecânica, Universidade de Brasília, Brasília, DF, 97p.

CESSÃO DE DIREITOS

AUTOR: Vítor Caixeta Fallieri Nascimento

TÍTULO: Fatigue Behavior of Forged Inconel 718 Including the Effects of Axial/Torsional Loading and High Temperature.

GRAU: Mestre ANO: 2022

É concedida à Universidade de Brasília permissão para reproduzir cópias desta dissertação de Mestrado e para emprestar ou vender tais cópias somente para propósitos acadêmicos e científicos. O autor se reserva a outros direitos de publicação e nenhuma parte desta dissertação de Mestrado pode ser reproduzida sem a autorização por escrito do autor.

Vítor Caixeta Fallieri Nascimento

SQS 114, Bloco A, Ap. 402

Asa Sul, Brasília, DF (CEP: 70377-010)

Acknowledgements

First of all, I would like to acknowledge SAFRAN, the institution that funded this study providing financial support and all necessary material.

I would like to give special thanks to Prof. Fábio Castro, who really was a great advisor. His patience, willingness, and knowledge may make him one of the best advisors at UnB. There has been a lot of learning and growth in this chapter of my life, and he has contributed enormously to this process. I would also like to acknowledge Prof. José Alexander Araújo for his important participation and effort to make this research project possible, always showing himself available for anything. Also, I want to thank Emmanuel Fessler, from Safran Aircraft Engines, for their contributions in the discussions and analyses made from the experimental results.

My colleague and friend Cainã Bemfica also deserve special thanks. Much of what I learned I credit to him. After all, maybe I couldn't even take the first step without him, and in the end, he let me ride my bike without training wheels. He literally was a second mentor to me, and I am so grateful to have the opportunity to work with such a capable and competent person who never went out of his way to teach me anything.

I would also like to thank the technicians Wesley, Rafael, Adriano, and Ivan, and my colleagues Gabriel, Maycol, and Thiago, who always supported me in laboratory activities.

I thank the friends I made along this journey: Canut, Raniere, Guilherme, and Vinícius. I will always be here to go out for a drink with you guys. An additional thanks to all my family and lifetime friends, who also have a share of contribution to this work, even if indirectly.

Por último e mais importante: agradeço aos meus pais, Teldo e Dalma. Me orgulho de ser seu filho e de ter a oportunidade de diariamente poder aprender sobre a vida com vocês; agradeço a minha irmã, Elisa, que sempre me manteve em seus pensamentos, emanando a melhor das energias; e agradeço a Nana, minha namorada e companheira de vida. Juntos, nós dois vamos seguir vencendo os obstáculos e desafios que a vida nos impõem. Obrigado pelo eterno apoio incondicional. Vocês são o que há de mais especial para mim.

Abstract

The goal of this work is to investigate the effects of high temperature on the fatigue behavior of forged Inconel 718 under axial/torsional loading conditions. To this end, strain-controlled traction, torsion, and proportional traction-torsion fatigue tests were performed at room temperature and 450 °C on thin-walled tubular specimens extracted from an as-forged turbine disk. All tests were conducted at a loading frequency of 0.5 Hz with axial and shear strain ratios equal to zero. The applied equivalent von Mises strain was such to result in fatigue lives within the range of 10^4 to 10^6 cycles, which is the typical life of the component of interest in this study. Under these loading levels and regardless of the temperature, Inconel 718 presented elastic shakedown after the first loading cycle. Due to the elastic behavior in the stabilized regime, the test control mode could be switched to load-controlled, enabling the use of higher frequencies, which reached up to 5 Hz. It was observed that for a given loading condition and prescribed equivalent strain, the fatigue lives of tests at 450 °C were longer than the room temperature tests. Moreover, the longest lives were observed in the torsion tests, followed by the proportional and traction tests in all temperature and prescribed equivalent strain tested. The capability of the cyclic plasticity model proposed by Chaboche in describing the cyclic response of Inconel 718 was also addressed. This model successfully simulated the stress-strain behavior of this material under all loading conditions, and for both temperatures investigated. In addition, the cracking behavior of the material was examined. For both temperatures, the traction tests failed by Mode I tensile cracks, while Mode II shear cracks were observed in the torsion and proportional tests. After a scanning electron microscope analysis, it was concluded that the transgranular propagation mode was the predominant failure mechanism of all tested conditions. Despite that, elements of intergranular fracture were identified at the crack initiation site of the proportional tests. The fatigue life of Inconel 718 was predicted by the Fatemi–Socie (FS) and the multiaxial version of the Smith–Watson–Topper (SWT) fatigue models, resulting in

estimations within a factor-of-two and a factor-of-four, respectively. Moreover, crack directions were also determined by the critical plane models and compared with the orientation of the observed cracks. The SWT model correctly predicted the crack direction of the traction tests, while the FS model was more accurate in determining the orientation of the cracks seen in the torsion tests. None of the two models was able to correctly predict the angles of the critical plane in all tested loading conditions.

Keywords : multiaxial fatigue, high temperature, Inconel 718, critical plane models, cyclic plasticity

Resumo

O objetivo deste trabalho é investigar os efeitos da alta temperatura no comportamento à fadiga do Inconel 718 forjado sob condições de carregamento axial/torcional. Para tanto, testes de fadiga controlados por deformação foram realizados à temperatura ambiente e 450 °C em corpos de prova tubulares de paredes finas extraídos de um disco de turbina forjado. Trajetórias de carregamento axial, torcional e proporcional foram testadas e todos os testes foram conduzidos a uma frequência de carregamento de 0.5 Hz com razões de deformação axial e de cisalhamento iguais a zero. A deformação equivalente de von Mises aplicada resultou em vidas de fadiga dentro da faixa de 10^4 a 10^6 ciclos, que é a vida típica do componente de interesse neste estudo. Sob esses níveis de carregamento e independente da temperatura, o Inconel 718 apresentou acomodamento elástico após o primeiro ciclo de carregamento. Devido ao comportamento elástico no regime estabilizado, o modo de controle de teste pôde ser alterado, passando a ser controlado por carga. A mudança no modo controle possibilitou o uso de frequências mais altas, que chegaram a até 5 Hz. Observou-se que para uma dada trajetória de carregamento e deformação equivalente prescrita, as vidas de fadiga dos testes a 450 °C foram maiores que a dos testes à temperatura ambiente. Além disso, as vidas mais longas foram observadas nos ensaios torcionais, seguidos dos ensaios proporcionais e axiais em todas as temperaturas e deformações equivalentes prescritas testadas. A capacidade do modelo de plasticidade cíclica proposto por Chaboche em descrever o comportamento cíclico do Inconel 718 também foi abordada. Este modelo simulou com sucesso o comportamento tensão-deformação deste material sob todas as condições de carregamento e temperaturas investigadas. Além disso, o comportamento de fratura do material foi examinado. Para ambas as temperaturas, os ensaios axiais falharam por trincas de tração Modo I, enquanto trincas de cisalhamento Modo II foram observadas nos ensaios torcionais e proporcionais. Após análises em microscópio eletrônico de varredura, concluiu-se que o modo de propagação transgranular foi o mecanismo de falha predominante em todas as condições testadas.

Apesar disso, elementos de fratura intergranular foram identificados no local de iniciação das trincas dos ensaios proporcionais. A vida em fadiga do Inconel 718 foi estimada pelo critério de fadiga de Fatemi–Socie (FS) e pela versão multiaxial do modelo de Smith–Watson–Topper (SWT), resultando em estimativas dentro de um fator-de-dois para FS e de um fator-de-quatro para SWT. Além disso, as direções das trincas também foram determinadas pelos dois modelos de plano crítico usados e comparadas com a orientação das trincas observadas experimentalmente. O modelo SWT previu corretamente a direção das trincas dos ensaios axiais, enquanto o modelo FS foi mais preciso na determinação da orientação das trincas observadas nos ensaios torcionais. Nenhum dos dois modelos conseguiu prever corretamente os ângulos do plano crítico em todas as condições de carregamento testadas.

Palavras-chave : fadiga multiaxial, alta temperatura, Inconel 718, modelos de planos críticos, plasticidade cíclica

Contents

1	Introduction	1
1.1	Background and motivation	1
1.2	Objectives	3
2	Literature Review	5
2.1	Chemical composition and tensile properties	5
2.2	Microstructure	6
2.3	Fatigue behavior of Inconel 718	10
3	Experimental program	26
3.1	Material and specimen	26
3.2	Fatigue testing system	28
3.3	Procedure for calibration of the test temperature	32
3.4	Fatigue test procedure	34
4	Results and discussion	38
4.1	Fatigue test results	38
4.2	Cyclic stress-strain behavior	43
4.3	Modeling of the constitutive behavior	45
4.4	Observation of macroscopic fatigue cracks	49
4.5	Fracture surface examination	51
4.6	Evaluation of critical plane fatigue criteria	58
5	Conclusions	68
A	Observed Fatigue Cracks	I
A.1	Traction, 20 °C	I
A.2	Traction, 450 °C	II
A.3	Torsion, 20 °C	III
A.4	Torsion, 450 °C	IV
A.5	Proportional, 20 °C	V
A.6	Proportional, 450 °C	VI

List of Figures

1.1	Temperature and pressure distribution inside an turbofan engine. Image taken from Stuesson [4].	2
1.2	Materials typically used in turbofan engines [5].	3
2.1	(a) Micrographs taken by Collier et al. [32] registering the γ' and γ'' precipitates in Inconel 718 samples. Note the two different geometric shapes in the image: the spherical format is related to the γ' phase, and the disk-shaped associated with the γ'' phase; (b) Image taken from Chamanfar et al. [33] showing the γ' and γ'' phases surrounding δ precipitates.	7
2.2	(a) Needle-like δ phase surrounded by γ' and γ'' phases, represented by the small white structures [34]; (b) δ phase within and at the grain boundaries with both the needle-like and fine block morphology [38].	8
2.3	(a) Distribution of MC carbides along the grains of an Inconel 718 sample [40]; (b) Comparison between the geometrical aspects of the γ' , γ'' , δ , and MC phases [33].	9
2.4	(a) Morphology of Laves phase surrounded by δ phase precipitates in a Inconel 718 sample [43]; (b) Preferential crack initiation and propagation through Laves phase [42].	9
2.5	Cyclic softening of Inconel 718 from fully reversed uniaxial tests reported by Fournier and Pineau [7] at different temperatures conditions.	11
2.6	Effects of the loading frequencies on the evolution of axial stress with the number of cycles on uniaxial fatigue tests conducted on Inconel 718 at 823 K (550 °C) [7].	11
2.7	Effects of temperature on the strain-life behavior of Inconel 718. The plot presents the plastic strain range versus the number of cycles. Figure taken from Sanders et al. [8].	12
2.8	Effects of temperature on the plot of stabilized mean stress versus plastic strain range presented by Cook [9]. The strain ratio used was $R_\epsilon = 0$	13
2.9	Deformation bands in aged Inconel 718 cyclically deformed for (a) three reversals and (b) 1656 cycles (failure). The bands distribution is similar in both cases, although bands are better defined in the failed sample. Images taken from Worthem et al. [10].	14

2.10	Serrated flow in plastic portions of hysteresis loops during fatigue tests with a 2% strain range: (a) solution annealed (first 8 cycles), (b) double aged alloy (first 7 cycles), (c) double aged alloy (218th cycle). Image taken from Rao et al. [11].	15
2.11	Ramberg-Osgood alternating stress versus fatigue life for test temperatures ranging from 149 to 537 °C, as reported by Warren and Wei [12]. Note the crossover of 149-454 °C fatigue curves at an alternating stress level about 840 MPa.	16
2.12	Failure mechanisms of fatigue tests carried out with $R_\epsilon = 0$ under different temperature conditions. Reported by Marderbacher et al. [13].	17
2.13	Schematic representation of the hysteresis loops of direct aged (red - A) and solution treated (blue - B) Inconel 718 [13]. Note the higher mean stresses achieved with the DA alloy as a consequence of the increased concentrations of γ' and γ'' precipitates.	18
2.14	Hysteresis loops showing serrated flow in plastic portions of its branch with the lower strain rate under (a) slow-fast and (b) fast-slow waveforms. Reported by Prasad et al. [14].	19
2.15	Loading paths used by Socie and co-authors [16–18] to investigate the fatigue behavior of Inconel 718.	21
2.16	Influence of mean stress on the crack growth rate. Image taken from Socie and Shield [17].	22
2.17	Correlation of Inconel 718 fatigue test data with the fatigue damage model proposed by Socie et al. [16] (Eq. 2.1). Image taken by Socie et al. [18].	22
2.18	Loading paths tested by Filippini et al. [23].	24
3.1	Thin-walled tubular specimen used in the fatigue tests, all dimensions in mm.	26
3.2	Stereographic microstructure of forged Inconel 718.	27
3.3	As-polished (a) and chemically attacked (b) microstructure of Inconel 718.	28
3.4	High-temperature axial/torsional testing system used in the fatigue tests.	30
3.5	High-temperature axial/torsional extensometer used to measure and control the axial and shear strains over the gage length of the specimen.	30
3.6	Failure at the indentation mark made on specimen 4A2, which was tested at room temperature under uniaxial loading. The indentation marks are used as a reference for positioning the extensometer on the specimen.	31
3.7	Photos of the attachment of the indentation tool on the specimen and its assembly in the bench vise.	32
3.8	Fixed K-type thermocouple used to control temperature during tests.	33
3.9	Position of the K-type thermocouples welded into the specimen: Upper End (UE), Upper Gauge (UG), Middle Gauge (MG), Lower Gauge (LG), and Lower End (LE).	33
3.10	Loading paths used in the fatigue tests.	35
3.11	Stress-strain response of a uniaxial test conducted at $\epsilon_a = 0.35\%$ and $R_\epsilon = 0$, which shows elastic shakedown after the first loading cycle.	36

3.12	Schematic of the load-drop criterion used to stop a strain-controlled fatigue test. The inset shows the crack observed in the specimen after the interruption of the test.	37
4.1	Normalized strain-life data of Inconel 718 under different axial/torsional loading paths, at room temperature and 450 °C.	40
4.2	Normalized pseudo stress-life data of Inconel 718 under different axial/torsional loading paths, at room temperature and 450 °C.	40
4.3	Normalized stress-strain hysteresis loops of traction tests at (a) 20 and (b) 450 °C.	43
4.4	Normalized stress-strain hysteresis loops of torsion tests at (a) 20 and (b) 450 °C.	44
4.5	Normalized stress-strain hysteresis loops of proportional tests at (a) 20 and (b) 450 °C.	44
4.6	Normalized experimental data used to determine the Chaboche parameters at room temperature. Data was taken from a traction test carried out on specimen 7A1.	47
4.7	Normalized experimental data used to determine the Chaboche parameters at 450 °C. Data was taken from a traction test carried out on specimen 2B1.	47
4.8	Simulated and experimental von Mises stress components from traction tests at (a) room temperature and (b) 450 °C. Stress values were normalized.	48
4.9	Simulated and experimental von Mises stress components from torsion tests at (a) room temperature and (b) 450 °C. Stress values were normalized.	49
4.10	Simulated and experimental von Mises stress components from proportional tests at (a) room temperature and (b) 450 °C. Stress values were normalized.	49
4.11	(a) Coordinate system attached to a representative volume of material of the thin-walled tubular specimen, (b) definition of the angles ϕ and θ , (c) examples of critical planes perpendicular to the surface.	50
4.12	Macroscopic crack of a traction test conducted at room temperature on specimen 7A1. In detail, the angles observed in the crack propagation region, defined by the blue color.	52
4.13	Macroscopic crack of a traction test conducted at 450 °C on specimen 2B1. In detail, the crack initiation, propagation, and final failure regions are defined by the colors red, blue, and pink, respectively.	52
4.14	Macroscopic cracks of torsion tests at (a) room temperature and (b) 450 °C.	53
4.15	Macroscopic cracks of proportional traction-torsion tests at (a) room temperature and (b) 450 °C.	53
4.16	Ti-rich metal carbide at the crack initiation locus of specimen 2B1, used in a high-temperature traction test. An EDX image in the lower-left corner shows the titanium distribution in the figure.	54

4.17	Scanning electron micrograph of facets structures near the failure initiation locus, indicating the transgranular propagation mode as the main crack growth mechanism from a room temperature torsion test performed on specimen 4B1.	55
4.18	Striation marks were observed in a high-temperature traction test conducted on specimen 2B1.	56
4.19	Striation marks were observed in a high-temperature torsion test conducted on specimen 9A1.	56
4.20	Striation marks were observed in a room temperature proportional traction-torsion test conducted on specimen 7A2.	57
4.21	Intergranular propagation aspects of a high-temperature proportional traction-torsion test performed on specimen 4B3.	57
4.22	The transition from crack propagation to final failure of a high-temperature proportional test performed on specimen 4B3.	58
4.23	Calibration of Fatemi–Socie model using room temperature fatigue data.	61
4.24	Calibration of Fatemi–Socie model using high-temperature fatigue data.	61
4.25	Calibration of Smith–Watson–Topper model using room temperature fatigue data.	63
4.26	Calibration of Smith–Watson–Topper model using high-temperature fatigue data.	63
4.27	Observed lives vs. predictions made using the Fatemi–Socie criterion, considering Inconel 718 test data at room temperature and 450 °C.	64
4.28	Observed lives vs. predictions made using the Smith–Watson–Topper criterion, considering Inconel 718 test data at room temperature and 450 °C.	65

List of Tables

2.1	Chemical composition of Inconel 718, weight % [28].	5
2.2	Monotonic tensile properties of Inconel 718 at different temperatures [29].	6
2.3	Command signal and strain rates in tension and compression of the two asymmetrical waveforms used in the fatigue tests performed by Prased et al. [14].	18
3.1	Inner and outer diameters and roughness measured in the gauge length of some specimens	29
3.2	Temperature [°C] measured by the fixed (T_{UFix} and T_{LFix}) and welded (T_{UE} , T_{UG} , T_{MG} , T_{LG} , and T_{LE}) thermocouples for a furnace temperature control of 550 °C.	33
4.1	Inconel 718 fatigue test data.	41
4.2	Elastic moduli of Inconel 718 at room temperature and 450 °C. Units in GPa.	44
4.3	Constants of the Chaboche model for Inconel 718 at room temperature and 450 °C.	46
4.4	Critical plane angles.	51
4.5	Material constants of the Fatemi–Socie strain-life relation (Eq. 4.10) obtained after the calibration process that used pure traction and torsion fatigue data at room temperature and 450 °C.	60
4.6	Material constants of the Smith–Watson–Topper strain-life relation (Eq. 4.11) obtained from traction and torsion fatigue data at room temperature and 450 °C.	62
4.7	Observed and estimated critical plane directions of the valid tests carried out in the fatigue campaign.	67

1 | Introduction

1.1 Background and motivation

The aeronautic industry is a relevant economic area that involves vanguard technology to handle the challenges associated with aviation. Over the years, aiming to produce airplanes more efficient and effective for the various demands and applications that arose, engineers developed knowledge and technologies relative to the different aspects associated with the design of an airplane. In particular, enormous efforts were made in the development of lighter and stronger materials to be used in components of different structures of an airplane. One of the challenges faced by the designers was the severe conditions experienced by many aircraft components, some being safety-critical components subjected to extremely degrading environments, such as those that compose gas turbines. In this scenario, maintaining the strength of materials under high-temperature conditions was found to be an important issue to overcome. Within this context, metal superalloys were developed at the beginning of the 20th century to withstand such conditions. These materials are characterized by preserving some of their mechanical properties at elevated temperatures, allowing them to be used at high fractions of their melting point [1]. As a consequence, superalloys made much of the high-temperature engineering technology possible over time. In the present work, an important superalloy will be studied: INCONEL[®] alloy 718 (Inconel 718).

Inconel 718 is a Ni-based superalloy introduced in forged and cast form by INCO's Huntington Alloys Division in the late '50s [2]. At that time, with the accelerated development of jet engines, many superalloys were launched and tested for aeronautical purposes. The industry was looking for materials capable of resisting the mechanical loads and temperature variations suffered by turbines components. In addition, considering the complex geometries of the components involved, the machinability of materials was also an important parameter to be taken into account.

Like other superalloys of the time, Inconel 718 showed enhanced strength and temperature capabilities. However, its good weldability and lack of sensitivity to strain-age cracking during heat treatment of weldments set it apart from the others [3]. As a result, this superalloy was widely used in components that operate at high temperatures, representing a major advancement in its class of materials. Thus, this alloy can represent more than 30% by weight of the material used in some turbofan engines [2] and is positioned mainly in the higher temperature regions. Figs. 1.1 and 1.2 illustrate this condition, emphasizing that the highest concentrations of Ni-based alloys are located in the higher temperatures regions of the turbine.

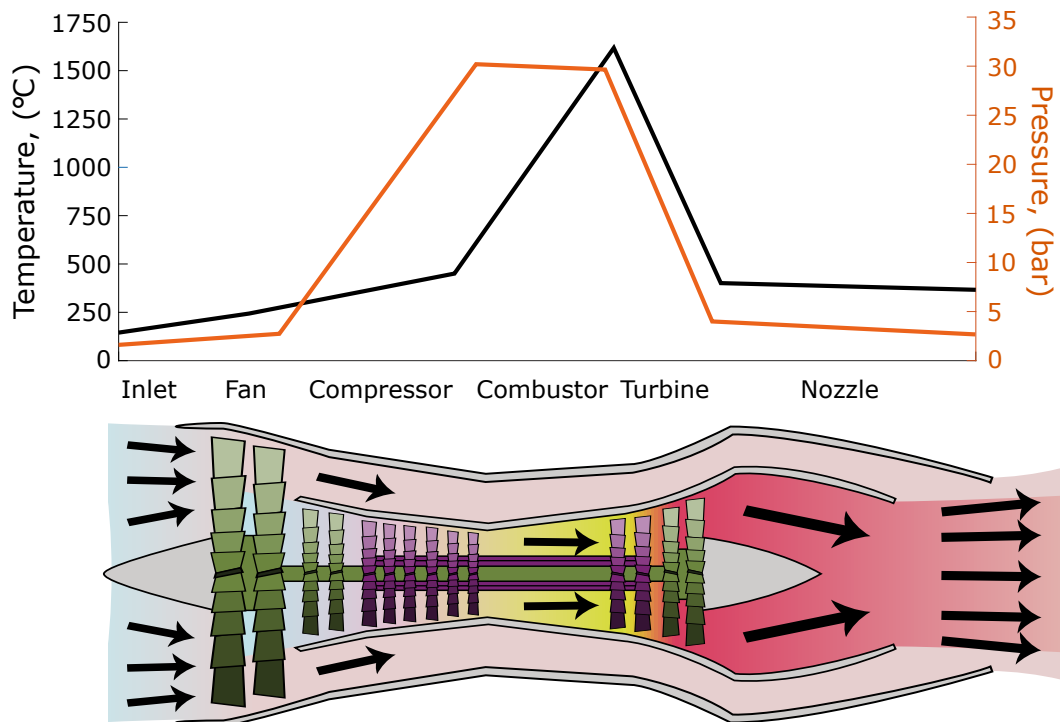


Figure 1.1 Temperature and pressure distribution inside an turbofan engine. Image taken from Sturesson [4].

Noting that repeated loading is usually involved in Inconel 718 applications, determining its fatigue behavior is crucial to use this material in a safer and more profitable way. This alloy was extensively studied due to its importance, mainly during the '80s, and significant advances were made in the characterization of its mechanical properties. Several works investigated the uniaxial fatigue behavior of Inconel 718 [6–15], but few addressed the multiaxial loading conditions [16–21]. Moreover, the axial-torsional fatigue behavior at high temperatures has received even less attention [22–24]. However, it should be noted that the multiaxial stress state at elevated temperatures more accurately describes a wider range of operating conditions

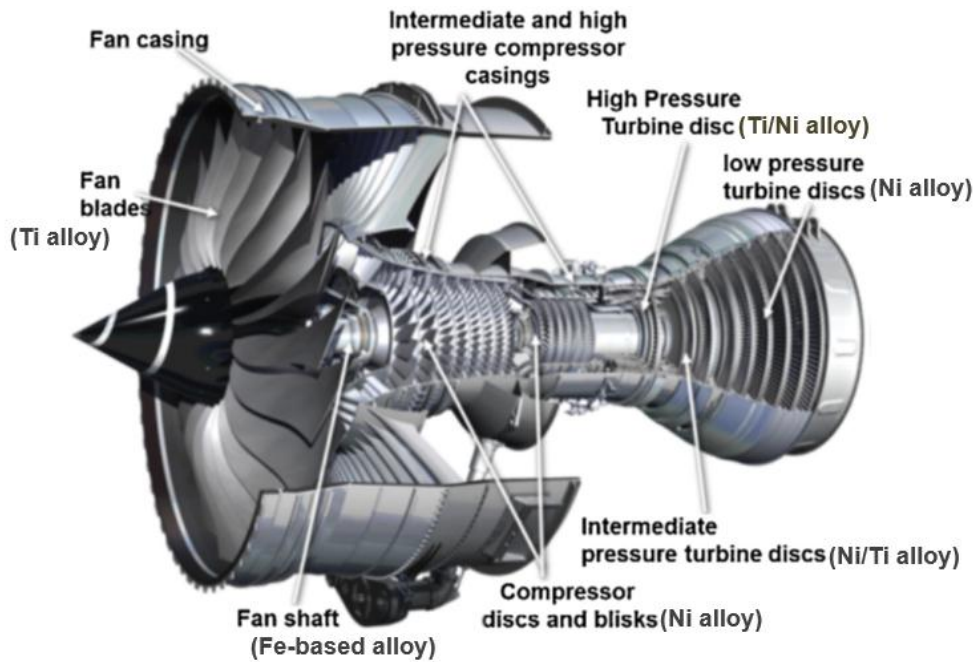


Figure 1.2 Materials typically used in turbofan engines [5].

to which Inconel 718 components are submitted. Under these circumstances, the lack of high-temperature multiaxial fatigue data on forged Inconel 718 motivates this work since the fatigue behavior of this material under these conditions has not yet been well established. In addition, recent developments regarding the additive manufactured (AM) Inconel 718 are also a motivator, once actual demands from the industry are related to the comparison between the mechanical properties obtained with the modern (AM) and traditional (Forged) manufacturing methods.

1.2 Objectives

The general objective of the present research is to investigate the fatigue behavior of forged Inconel 718, with an emphasis on the effects of axial/torsional loading and high temperature. For comparison purposes and aiming to enrich the analysis, the fatigue behavior of this material will also be characterized at room temperature. To achieve the main objective, the following specific goals were established:

- To perform traction, torsion, and proportional traction-torsion fatigue tests on thin-walled tubular specimens at room temperature and 450 °C.
- To investigate the cyclic stress-strain behavior of Inconel 718, and simulate it using the

Chaboche plasticity model [25].

- To conduct scanning electron microscopy (SEM) analysis to determine the failure mechanism and the crack initiation site for each loading condition.
- To assess the fatigue lives predicted by using the Fatemi–Socie criterion [19] and the multiaxial version of the Smith–Watson–Topper criterion [26, 27].

2 | Literature Review

This section introduces a brief literature overview regarding the monotonic tensile properties and the fatigue properties of Inconel 718 at room and high temperatures. Initially, the composition of this material is presented, focusing on the influence that its microstructural elements have on its mechanical properties. Then, the uniaxial and multiaxial fatigue behavior of Inconel 718 is discussed, presenting the principal studies carried out in this regard.

2.1 Chemical composition and tensile properties

Inconel 718 is a superalloy composed of several components that has nickel as its main chemical element. Among the others, iron, chromium and niobium stand out for having higher percentages of mass and for composing precipitates that substantially alter the mechanical strength of this material. According to the American Society for Metals [28], the chemical composition of Inconel 718 must comply with the specifications presented in Table 2.1.

Table 2.1 Chemical composition of Inconel 718, weight % [28].

Element	Min.	Max.
Ni	50.000	55.000
Cr	17.000	21.000
Nb+Ta	4.750	5.500
Mo	2.800	3.300
Ti	0.650	1.150
Al	0.200	0.800
Co	-	1.000
Mn	-	0.350
Si	-	0.350
Cu	-	0.300
C	-	0.080
S	-	0.015
B	-	0.006
Fe	Remainder	

Considering that Inconel 718 is widely used in propulsion components in the aeronautical industry, the importance of determining its properties under different temperature conditions becomes clear. The monotonic tensile properties of Inconel 718 were obtained by Sun and Yuan [29] for different temperatures and are presented in Table 2.2. It should be noted that temperature directly affects the values of some mechanical properties, which generally decrease when temperature increases. In this regard, an increase in temperature from 20 to 650 °C resulted in a relative decrease of 17% in Young’s modulus, 11% in yield stress, and 12% in ultimate tensile strength.

Table 2.2 Monotonic tensile properties of Inconel 718 at different temperatures [29].

Temperature [°C]	Young’s modulus E [GPa]	Yield stress σ_y [MPa]	Ultimate tensile strength σ_u [MPa]	True strain at fracture ε_f [%]
20	206.3	1192	1433	26.4
300	190.2	1140	1334	21.2
550	180.2	1090	1282	21.5
650	171.6	1064	1255	23.4

2.2 Microstructure

From a microscopic perspective, Inconel 718 consists of a matrix phase γ , composed exclusively of nickel, and some secondary phases formed from different compositions between the alloying elements, identified as γ' , γ'' , δ , MC, and Laves. The mechanical behavior of this material is strongly affected by the presence and distribution of the secondary phases. Therefore, this section introduces a brief presentation of each of these secondary phases, summarizing its main properties and characteristics.

2.2.1 γ' and γ'' phases

The strength of this superalloy is derived from the precipitates γ' and γ'' , which are strengthening phases formed from the combination of Al, Ti, and Nb with Ni, being chemically formulated as $\text{Ni}_3(\text{Al,Ti})$ and $\text{Ni}_3(\text{Nb})$, respectively. The strengthening of this alloy by precipitates particles is related to many factors: the coherence of both precipitates with the γ matrix, their intrinsic strengths, and volume fraction. Furthermore, the anti-phase boundary energy in the ordered γ' and γ'' phases, which is proportional to the energy required for the passage of

dislocations, is also a strengthening mechanism [30]. These phases often precipitate together in Inconel 718, although the morphology of the γ' phase is spherical, while the γ'' phase precipitates as disk-shaped particles, as shown in Figs. 2.1 (a) and (b). According to Paulonis et al. [31], the volume fraction of γ' and γ'' can reach up to 4% and 15%, respectively. As a result, it should be noted that γ' precipitates contribute to the strength of the alloy to a lesser degree than the γ'' precipitates, found to be the principal strengthening phase in this material.

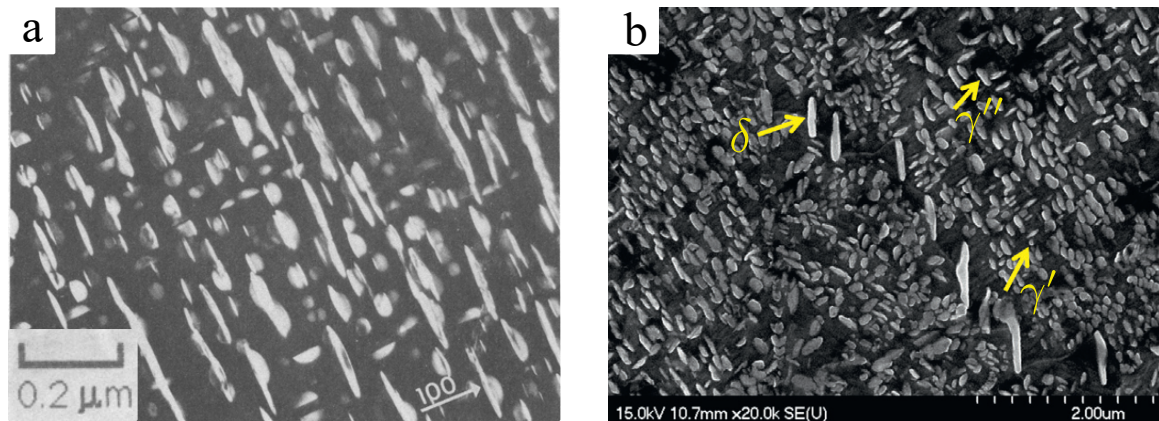


Figure 2.1 (a) Micrographs taken by Collier et al. [32] registering the γ' and γ'' precipitates in Inconel 718 samples. Note the two different geometric shapes in the image: the spherical format is related to the γ' phase, and the disk-shaped associated with the γ'' phase; (b) Image taken from Chamanfar et al. [33] showing the γ' and γ'' phases surrounding δ precipitates.

2.2.2 δ phase

Under thermal exposure, the metastable γ'' phase can be converted into the thermodynamically stable δ phase, noting that both of them are formed with Ni and Nb and denoted by the same chemical formula: $\text{Ni}_3(\text{Nb})$. Incoherent with the γ matrix and having a needle or plate-like morphology, the δ phase usually confers a loss of strength in the material since its precipitation consumes Nb, resulting in a reduction in the principal alloy strengthening precipitate γ'' [34]. At 650 °C, the conversion from γ'' to δ substantially increases, limiting the main applications of this material above this temperature range [35]. However, depending on the application, this phase can induce favorable effects on the microstructure and mechanical properties. Noting that the δ phase is often deposited at the grain boundaries, it can inhibit the grain growth during heat treatments and machining processes and also retard intergranular crack propagation [30], being beneficial to stress rupture and creep properties [36, 37]. Fig. 2.2(a) illustrates the needle-like δ phase close to grain boundaries and surrounded by γ' and γ'' phases, represented

by the small white structures. Despite that, the δ phase can also be present inside the grain, depending on its volume fraction [34]. This situation is illustrated in Fig. 2.2(b), where the δ phase is found within and at the grain boundaries.

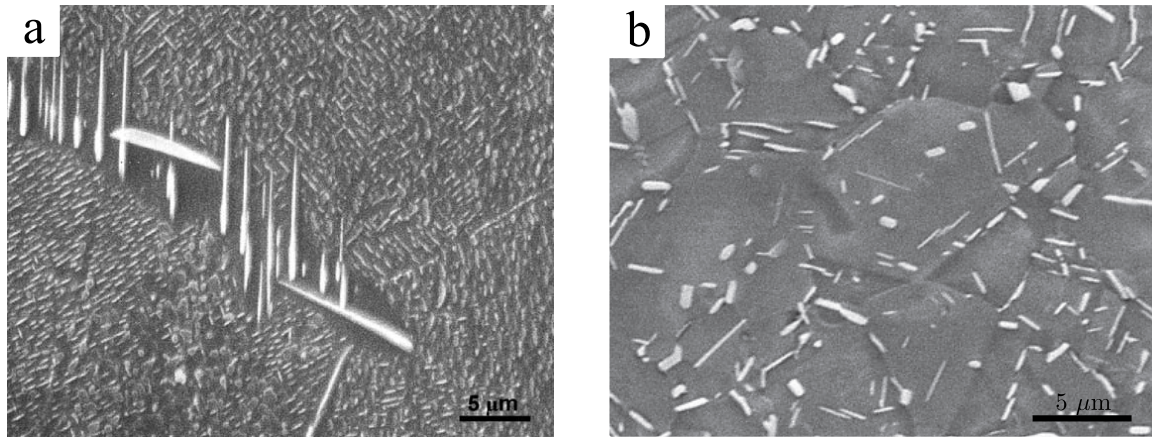


Figure 2.2 (a) Needle-like δ phase surrounded by γ' and γ'' phases, represented by the small white structures [34]; (b) δ phase within and at the grain boundaries with both the needle-like and fine block morphology [38].

2.2.3 MC carbides

MC-type carbides are another phase seen in Inconel 718, in which M stands for an alloying element that bonds with carbon to form a carbide. The MC phase rich in Nb, denoted as NbC, is the predominant carbide in this material, although Ti-rich carbides are also commonly found. These carbides usually have an irregular globular shape non-uniformly distributed, located both inside the grains and at their boundaries [30, 39]. The influence of the MC phase in the mechanical properties of Inconel 718 can be affected by the carbide size, its distribution, the presence of oxidation or a pre-crack, and even the mechanical test condition. If the carbide is located inside the grain, it can block dislocation movement and confer a small increase in matrix strength. However, if this intragranular carbide is positioned at the surface of any component, it may pre-crack or oxidize under unfavorable ambient conditions, degrading the fatigue properties [30]. On the other hand, the carbides that precipitate at grain boundaries can transition the fracture mode from transgranular to intergranular under room temperature conditions [39]. Furthermore, these carbides can result in longer fatigue lives at high temperatures depending on their size and distribution along the grain boundaries. Fig. 2.3(a) shows MC-type carbides distributed within and on the grain boundaries of an Inconel 718 sample, while in Fig. 2.3(b), the geometrical differences between the γ' , γ'' , δ , and MC phases are presented.

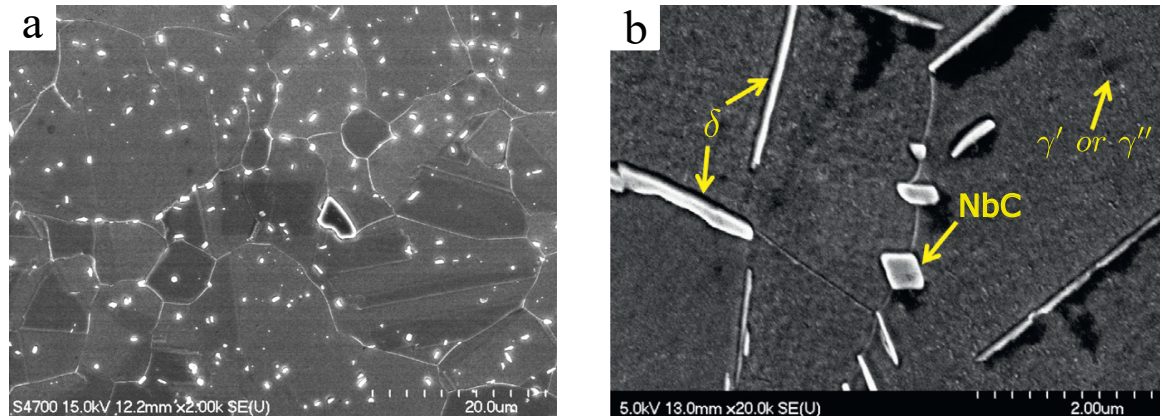


Figure 2.3 (a) Distribution of MC carbides along the grains of an Inconel 718 sample [40]; (b) Comparison between the geometrical aspects of the γ' , γ'' , δ , and MC phases [33].

2.2.4 Laves

Characterized to be a brittle intermetallic phase, the Laves phase is detrimental to the mechanical properties of Inconel 718. The Nb, Si, and Mo segregated during solidification and the high contents of Cr and Fe result in the necessary conditions for the formation of this phase, whose chemical composition is usually written as $(\text{Ni,Fe,Cr})_2(\text{Nb,Mo,Ti})$ [41]. Thus, when it is being formed, the Laves phase consumes the Nb reserves, limiting the precipitation of γ'' , which is the principal strengthening phase. According to Schirra et al. [42], Laves phase precipitates at grain boundaries as a continuous or semicontinuous network, so that the former accelerates fatigue crack propagation while the latter does not significantly affect the crack growth properties at high temperatures. Moreover, the strength and toughness are significantly reduced at room temperature, in addition to ductility, which decreases independently of temperature. Fig. 2.4(a) shows the morphology of the Laves phase in Inconel 718, while Fig. 2.4(b) illustrate a crack propagating through a Laves phase on a notched specimen.

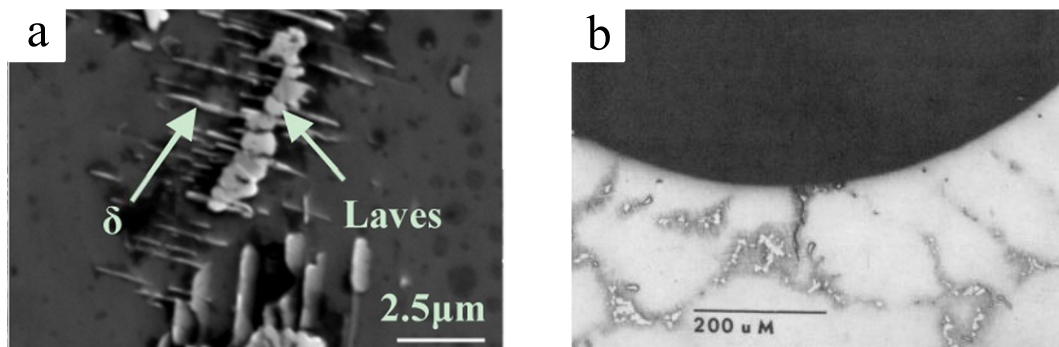


Figure 2.4 (a) Morphology of Laves phase surrounded by δ phase precipitates in a Inconel 718 sample [43]; (b) Preferential crack initiation and propagation through Laves phase [42].

2.3 Fatigue behavior of Inconel 718

Aiming to present the state of the art related to the fatigue behavior of Inconel 718, several research papers detailing the development of uniaxial and multiaxial fatigue studies in this material were summarized in this section and presented in chronological order. It should be noted that the Inconel 718 behavior at high temperatures has already been explored in the first publications due to the demands of the applications to which this material is submitted. Considering the test parameters that will be used in this work, special attention was given to fatigue studies that obtained its data from strain-controlled tests.

2.3.1 Uniaxial fatigue

In the first half of the 70s, Merrick [6] published a paper examining the low cycle fatigue (LCF) behavior of three wrought nickel-base alloys, including Inconel 718. The results of fully reversed strain-controlled tests performed at room temperature and 811 K (538 °C) were expressed in terms of a Coffin-Manson type equation, highlighting that, for all alloys, a life reduction was observed when increasing temperature. According to him, fatigue softening, characterized by a decay of the stress amplitude values along with the cycles, occurred at both temperatures and was attributed to the shear of γ' or γ'' precipitates. In addition, he observed that crack propagated by a mixture of transgranular and intergranular modes.

In 1977, Fournier and Pineau [7] continued the studies on the low cycle fatigue characterization of Inconel 718 at high temperatures introducing more fatigue data on this regards. The LCF behavior of this material was also obtained from fully reversed strain-controlled uniaxial tests conducted not only at high temperature (823 K/550°C), but also at room temperature (298 K/25°C) for comparison purposes. Confirming the results obtained by Merrick, the authors observed that the fatigue life lasted less at 823 K (550°C) and that this material experienced cyclic softening, especially at high temperatures (Fig. 2.5). Life reduction between temperatures tested was attributed principally to the acceleration of the crack initiation period. The impact of the loading frequency on the fatigue life was assessed under high-temperature conditions, and the authors observed that the number of cycles to fracture decreases as the cycling frequencies get lower, as shown in Fig. 2.6. They found out that, at low frequencies, cracks nucleation

is mainly along the twin deformation bands and at grain boundaries, while propagation is by transgranular mode at room temperature and by mixture mode at elevated temperatures, especially at low strain rates.

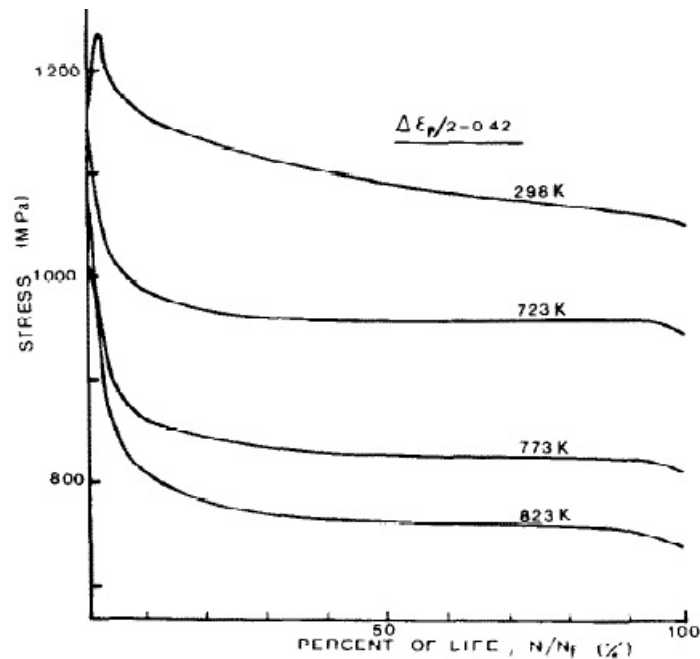


Figure 2.5 Cyclic softening of Inconel 718 from fully reversed uniaxial tests reported by Fournier and Pineau [7] at different temperatures conditions.

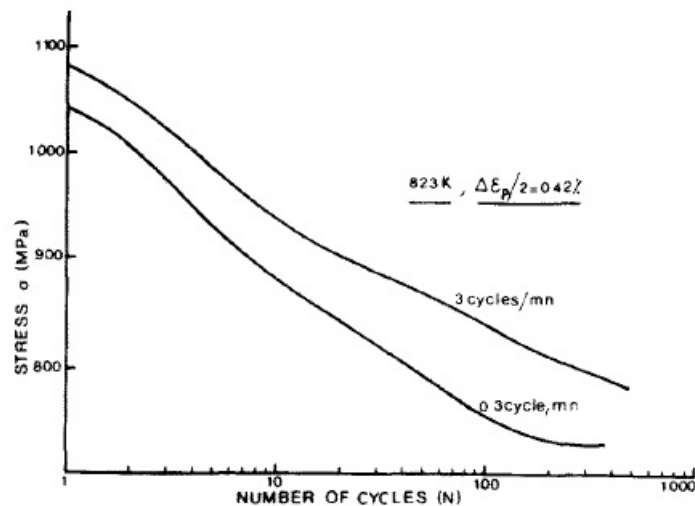


Figure 2.6 Effects of the loading frequencies on the evolution of axial stress with the number of cycles on uniaxial fatigue tests conducted on Inconel 718 at 823 K (550 °C) [7].

In the early 1980s, Sanders et al. [8] produced more Inconel 718 low cycle fatigue data in a temperature range from 204 to 649 °C aiming to investigate the dependency of the deformation mechanisms of this material on temperature. The authors noted a crossover in fatigue lives depending on temperature. At the low cycle regime, the lowest fatigue life was exhibited on tests

carried out at high temperatures. This trend reversed at the high cycle regime, though, when the fatigue life in a given strain range reached its highest values at intermediate temperatures. This phenomenon is shown in Fig. 2.7, which plots, for five different temperatures, the plastic strain range against the number of cycles to the initiation, defined as the cycles necessary to obtain the first noticeable increase in plastic strain after the initial softening. The difference in fatigue behavior for temperatures from 538 °C is remarkable, being possible to see the crossover point when fatigue life exceeds about 10^4 cycles. From this point, the lifetime at a given plastic strain range was greater for tests conducted on the two high temperatures conditions than on the three lower ones. Based on microscopy analysis, the authors observed a difference in the deformation structures of the higher and lower temperature tests. They postulated that the cyclic plastic behavior at 204, 316, and 427 °C is governed by twinning deformation, while at 538 and 649 °C, the predominant deformation mode is slip. According to them, these deformation mechanisms are responsible for the differences and similarities observed in the strain-life response of each temperature condition tested.

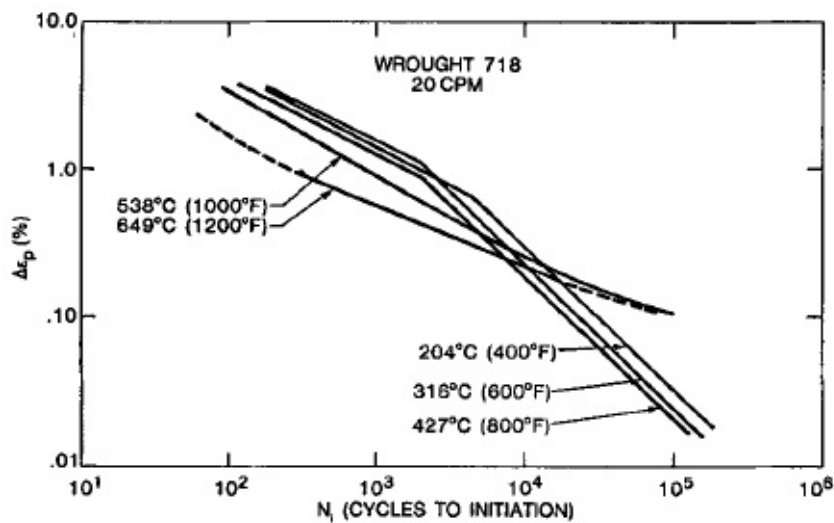


Figure 2.7 Effects of temperature on the strain-life behavior of Inconel 718. The plot presents the plastic strain range versus the number of cycles. Figure taken from Sanders et al. [8].

In 1982, Cook [9] investigated the effects of temperature and strain ratio on the cyclic stress-strain behavior of Inconel 718. The strain ratio relates the minimum and maximum prescribed strains and is defined as $R_\epsilon = \epsilon_{\min}/\epsilon_{\max}$ so that $R_\epsilon = -1$ represents a fully reversed loading, while $R_\epsilon = 0$ represents a zero-tension condition. It is worth noting that if the value of R_ϵ is other than -1, a mean strain state is imposed in the test, initially resulting in non-null

mean stresses. This mean stress state may change throughout the test due to the effects of mean stress relaxation, a phenomenon characterized by the decay of the mean stress component over the cycles and only seen in strain-controlled tests with plastic deformations involved. Cook tested several strain ratios under different temperatures conditions, including cases with R_ϵ equals -1 and 0, noting their effects on the stabilized stress state. He observed that this material presented mean stress relaxation in all tested temperatures, pointing out that total mean stress relaxation occurs for strain ranges larger than 1%, meaning that the mean stress relaxes toward zero after some loading cycles in those situations. Cook also assessed the relation of the stress relaxation with temperature by plotting the mean stress versus the plastic strain for different test temperatures, as shown in Fig. 2.8. He observed that regardless of the test temperature, the same amount of stress relaxation is achieved in tests with plastic strains greater than 0.1%. On the other hand, when lower plastic strain values are considered, the stress relaxation of room temperature tests tends to behave a little differently. The difference in this behavior is caused by the effects generated from the influence of temperature on elastic properties, where the higher yield stress leads to higher maximum stress.

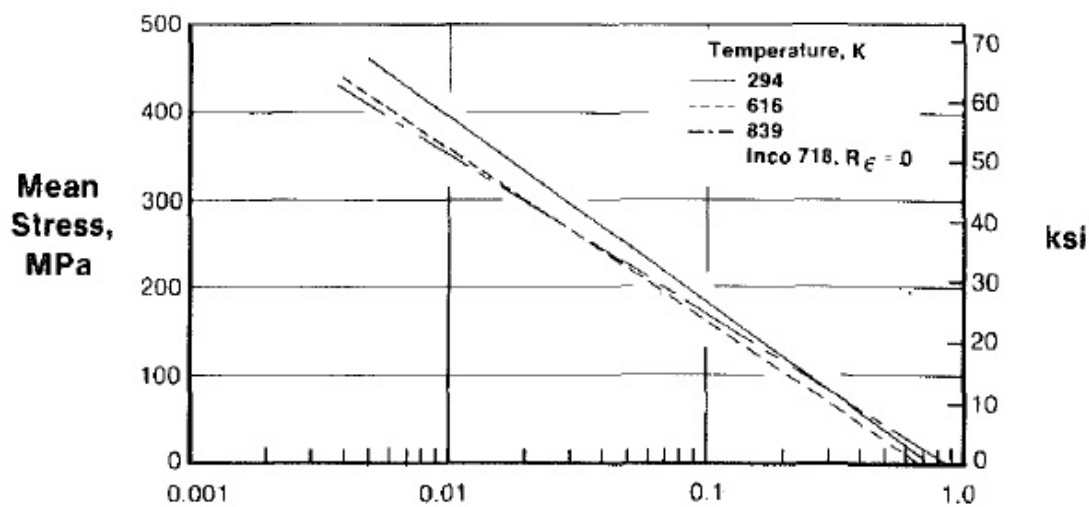


Figure 2.8 Effects of temperature on the plot of stabilized mean stress versus plastic strain range presented by Cook [9]. The strain ratio used was $R_\epsilon = 0$.

Already in the 1990s, Worthem et al. [10] related microstructural observations of the dislocation structures to the macroscopic deformation response of aged (precipitate-hardened) Inconel 718 in room temperature monotonic and fatigue tests. At that time, it was well established that in this material, cracks initiate and propagate along with planar deformation bands that lie on $\{111\}$ planes and are regularly spaced across the grain, as seen in Fig. 2.9. Under monotonic

loading, the authors observed that the dislocation structure inside a deformation band formed an inverse pileup at a grain boundary, which indicates that the boundary was the probable dislocation source. On the other hand, after a few cycles during fatigue loading, the bands contained a high density of dislocations in a complex arrangement. For comparisons purposes, monotonic tests were performed in homogenized samples of Inconel 718, characterized to be a precipitate-free material. At lower deformation levels, authors observed only one deformation band per grain and little evidence of work hardening. With the increase in deformation levels, work hardening began, and more bands nucleated, turning their spacing to become similar to that in the aged material. By this result, the authors concluded that precipitates have no role in the degree of coarseness of inhomogeneous deformation in this material, which was primarily a function of the amount of work hardening within the bands.

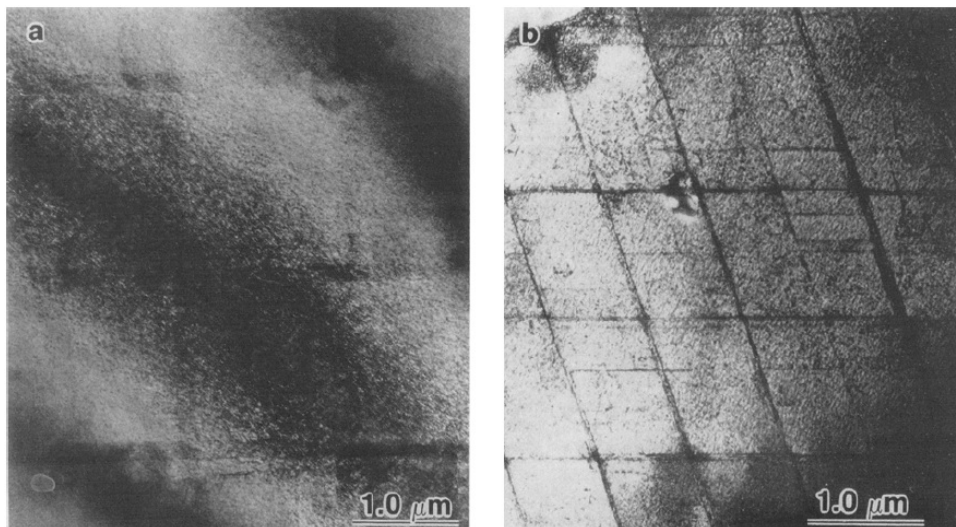


Figure 2.9 Deformation bands in aged Inconel 718 cyclically deformed for (a) three reversals and (b) 1656 cycles (failure). The bands distribution is similar in both cases, although bands are better defined in the failed sample. Images taken from Worthem et al. [10].

In 1995, Rao et al. [11] performed low cycle fatigue tests to study the occurrence of serrated flow in Inconel 718 under room temperature conditions. Serrated flow is a phenomenon characterized by "serrations" that occur on the stress-strain curve and is observed over a characteristic range of strain rate and temperature, which depends on the material composition. Aiming to determine the serrated flow mechanism, the specimens used in the fully reversed strain-controlled fatigue tests were submitted to two different heat treatments: some of them were double aged (DA), while others were solution annealed (SA). The authors observed cyclic softening since the first cycles in the DA alloy, while initial hardening followed by softening

characterized the room temperature stress response of Inconel 718 in the SA condition. During all fatigue life, unlocking type serrations were reported in the plastic portions of the hysteresis loops in both heat treatment conditions, as shown in Fig. 2.10. After transmission electron microscopy (TEM) analysis, the authors concluded that the cyclic deformation of this material occurred primarily by planar slip. Finally, they propose that the serrated flow was caused by the back stress exerted by accumulated parallel pileups of dislocations in planar slip bands added to the subsequent relaxation of internal stress resulting from the initiation of new plastic flow in adjacent grains.

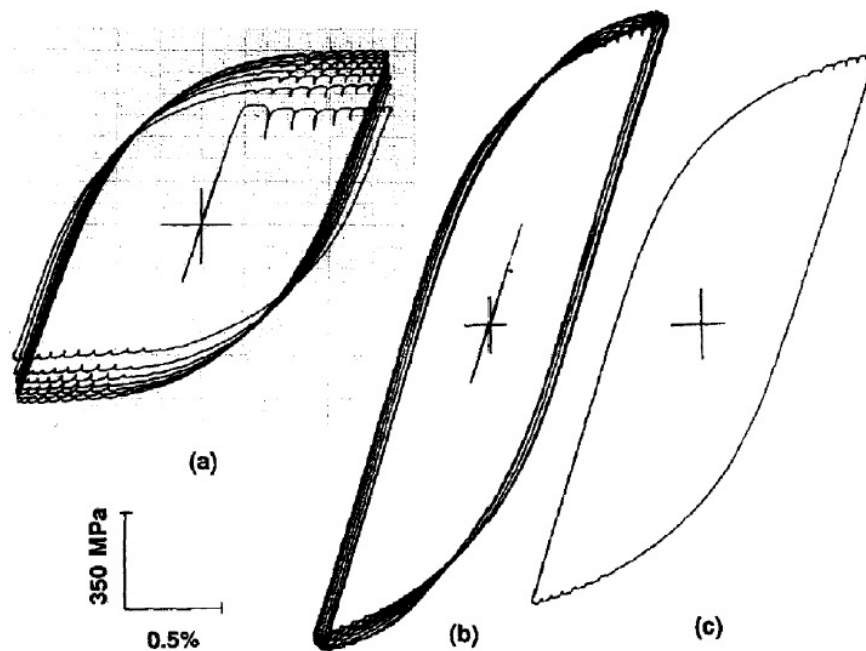


Figure 2.10 Serrated flow in plastic portions of hysteresis loops during fatigue tests with a 2% strain range: (a) solution annealed (first 8 cycles), (b) double aged alloy (first 7 cycles), (c) double aged alloy (218th cycle). Image taken from Rao et al. [11].

Years later, in 2006, Warren and Wei [12] conducted axial strain-controlled fatigue tests on direct age Inconel 718, aiming to assess its fatigue behavior at 149, 315, 454, and 537 °C. Fatigue lives were plotted as a function of the Ramberg-Osgood alternating stress for all temperatures, as shown in Fig. 1. The authors observed a crossover in the stress-life responses at an alternating stress level of approximately 840 MPa. The fatigue life increased with temperature when stresses were below this point, while a reversion on this relation was noted when the stresses were above it, turning the fatigue life to decrease with increasing temperature. This conclusion is consistent with the results reported by Sanders et al. [8], confirming that a change in the stress/strain-life behavior is expected depending on temperature. Based on a thermally activated process that

reduces the generation of defects associated with grain boundaries stress concentrations, the authors proposed a mechanistic model seeking to describe the increase in fatigue life as a function of increasing test temperature. The predictions made by this model were in reasonable agreement with experimental data.

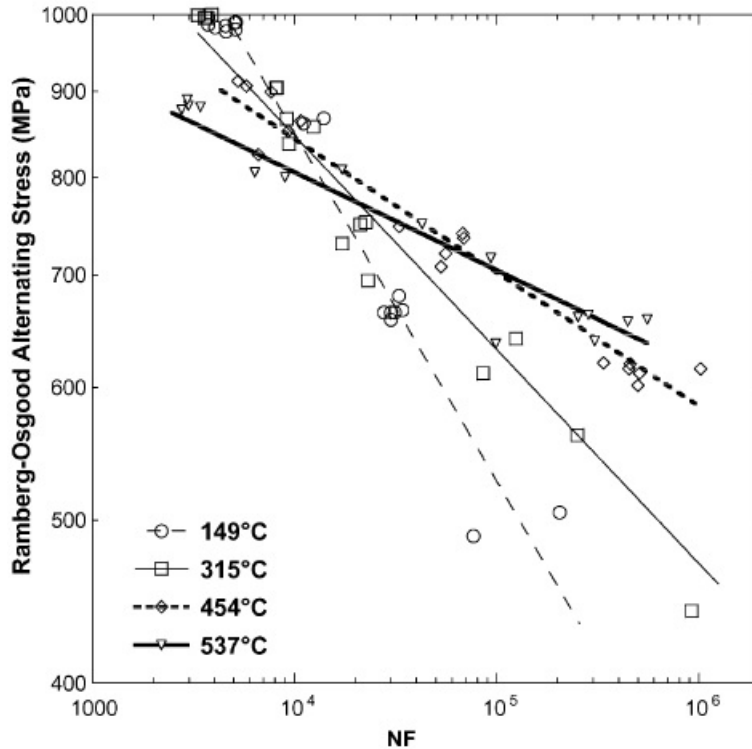


Figure 2.11 Ramberg-Osgood alternating stress versus fatigue life for test temperatures ranging from 149 to 537 °C, as reported by Warren and Wei [12]. Note the crossover of 149-454 °C fatigue curves at an alternating stress level about 840 MPa.

In 2013, Marderbacher et al. [13] performed a deep investigation into the influence of temperature and microstructure on the fatigue endurance of hot-forged Inconel 718 aircraft components. To this end, they performed several fatigue tests under a large variety of test temperatures up to 650 °C. Tests were mainly strain-controlled using strain ratios $R_\epsilon = 0$ and $R_\epsilon = -1$ and were carried out in direct aged (DA) and solution treated (ST) specimens. Such heat treatments were considered to enrich the assessment of the microstructural parameters since its different temperature and deformation ranges affect the process of precipitation and, consequently, the resulting strength. When compared to solution treated, it must be highlighted that both the yield and tensile strength are significantly raised in direct aging. The authors concluded that the failure mechanisms are the same for all temperatures and strain amplitudes tested. The exception is related to carbides, where cracks become more likely to initiate when

the upper strain increases and the operating temperature decreases, as shown in Fig. 2.12. They observed that the fatigue strength increases with temperature and decreases with grain size, although increasing strain amplitude reduces the positive influence of temperature. Furthermore, they also observed that the particle strengthening caused by the γ' and γ'' precipitates, more present in materials with DA heat treatment than in those with ST, has a negative effect on the fatigue strength. This effect is justified by an increase in the mean stress proportional to increasing the yield strength, as schematically illustrated in Fig 2.13. Finally, a temperature and microstructure-dependent fatigue model was proposed in order to predict the $\varepsilon - N$ curves. This model showed good agreement with the experimental data for both DA and ST alloys.

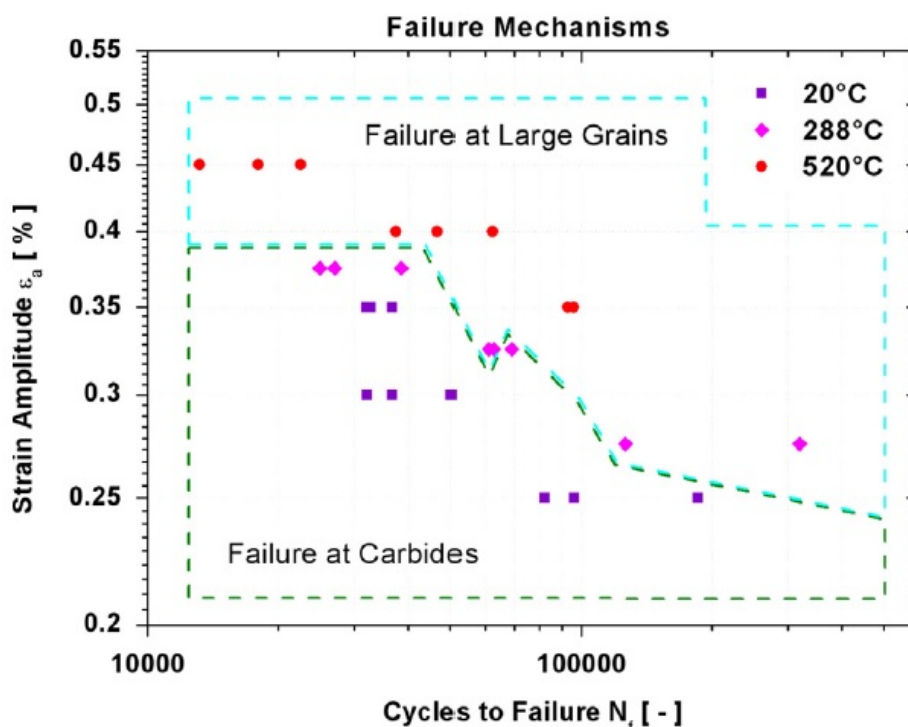


Figure 2.12 Failure mechanisms of fatigue tests carried out with $R_\varepsilon = 0$ under different temperature conditions. Reported by Marderbacher et al. [13].

In the same year, Prasad et al. [14] studied the effects of loading rate on the fatigue behavior of Inconel 718 at high temperatures. To this end, two asymmetrical waveforms were applied in strain-controlled fatigue tests carried out at 650 °C on specimens taken from a forged turbine disk. Table 2.3 shows the waveforms used in the tests, indicating that one of them was named fast-slow (f-s) and had a faster tension rate compared with the compression rate, while the other, called slow-fast (s-f), had a faster compression rate than the tension rate. For all tests, regardless of the waveform used, the authors observed a serrated flow in the lower strain rate

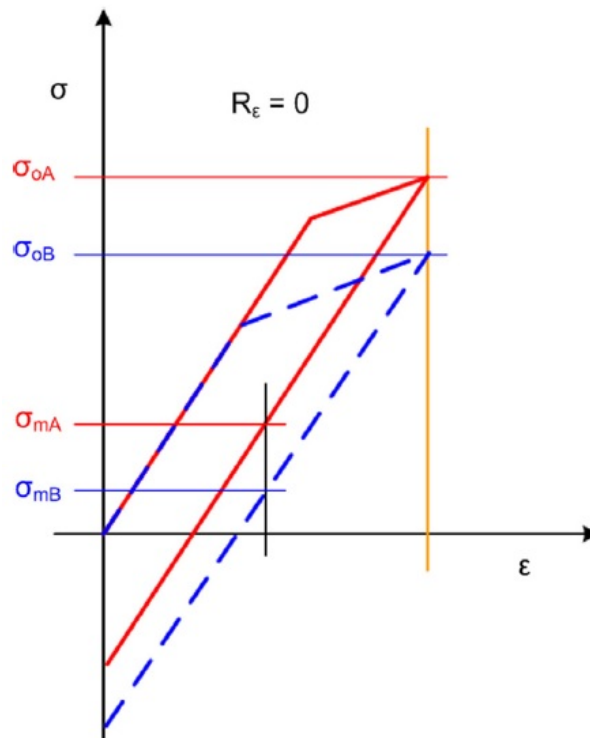




Figure 2.13 Schematic representation of the hysteresis loops of direct aged (red - A) and solution treated (blue - B) Inconel 718 [13]. Note the higher mean stresses achieved with the DA alloy as a consequence of the increased concentrations of γ' and γ'' precipitates.

branch of the hysteresis loops, indicating the occurrence of dynamic strain aging (DSA). The same is not seen in the branch with the higher strain rate. Fig. 2.14 illustrates this phenomenon in three different loading cycles of tests that used s-f (a) and f-s (b) waveforms. The authors concluded that under s-f waveforms, there was more accumulation of fatigue damage in terms of planar slip band spacing, justified by the high propensity seen in this waveform on exhibiting DSA. As a consequence, shorter fatigue lives were seen in tests conducted with the s-f waveform than in those that used the f-s waveform.

Table 2.3 Command signal and strain rates in tension and compression of the two asymmetrical waveforms used in the fatigue tests performed by Prased et al. [14].

Command signal	Total strain rate in tension (s^{-1})	Total strain rate in compression (s^{-1})
Fast-slow 	6.67×10^{-3}	6.67×10^{-5}
Slow-flow 	6.67×10^{-5}	6.67×10^{-3}

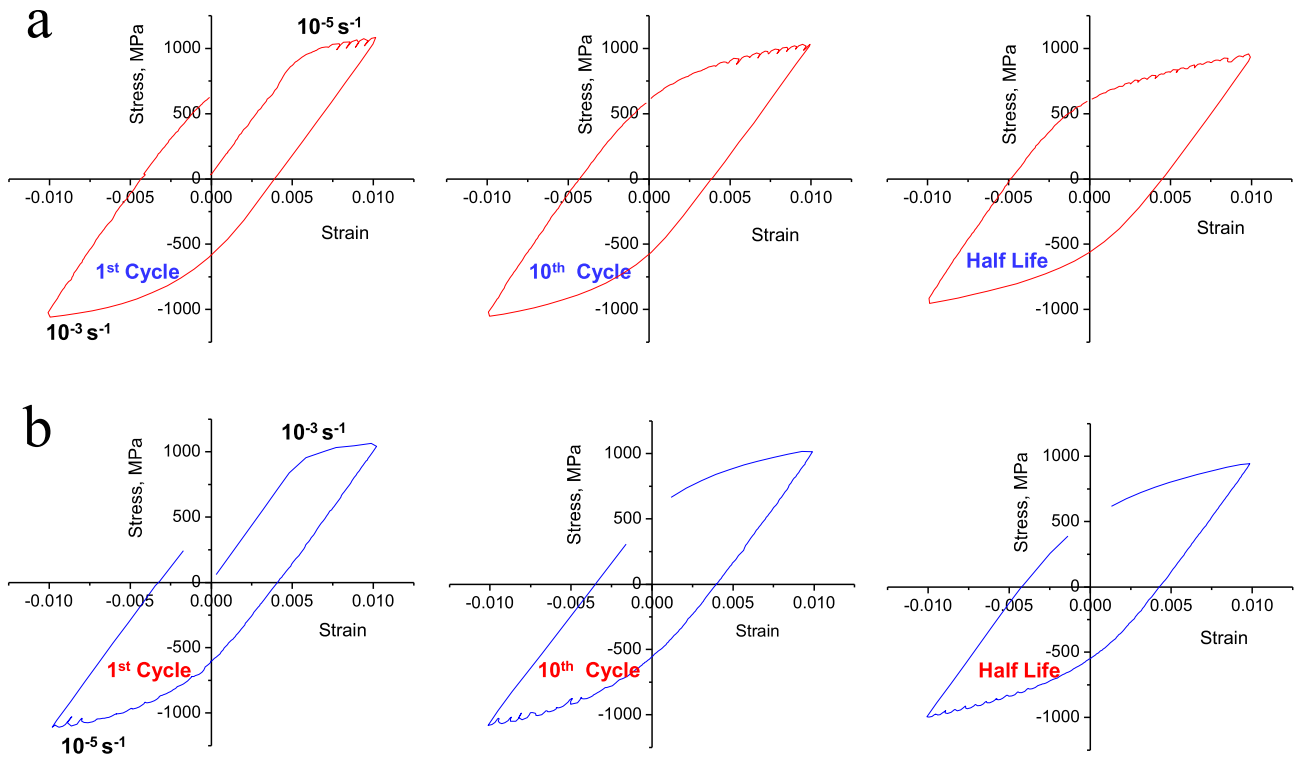


Figure 2.14 Hysteresis loops showing serrated flow in plastic portions of its branch with the lower strain rate under (a) slow-fast and (b) fast-slow waveforms. Reported by Prasad et al. [14].

More recently, in 2019, Huang et al. [15] compared the fatigue behavior of Inconel 718 under isothermal (IF) and thermomechanical (TMF) conditions. Thermomechanical fatigue occurs when a cyclic mechanical load is applied concurrently with a cyclic thermal load, resulting from thermal expansion/compression of the material as an effect of temperature variation. Under isothermal conditions, fully reversed strain-controlled low cycle fatigue tests were conducted at 350 and 650 °C. The TMF tests were performed within this temperature range under in-phase and out-of-phase modes, characterized by applying mechanical and thermal loads with a phase angle of 0° and 180°, respectively. The authors observed that the TMF tests imposed a more severe damage environment, especially under in-phase conditions, resulting in shorter fatigue lives. They also observed that intergranular fracture was the failure mode in isothermal tests at 650 °C and in-phase TMF tests, while transgranular fracture was the predominant failure mode of 350 °C isothermal tests and out-of-phase TMF tests. Lastly, the authors used the Coffin-Manson equation to fit the isothermal fatigue data. The fatigue life of the TMF tests exhibited better suitability with a hysteresis loop energy model, which was more efficient in considering the mechanical and thermal strains associated with this loading condition.

2.3.2 Multiaxial fatigue

In 1984, Socie et al. [16] performed axial-torsional strain-controlled fatigue tests at room temperature on tubular specimens taken from a forged ring of Inconel 718. Fully reversed and zero-tension tests were conducted, noting that the latter resulted in non-zero mean strain throughout the fatigue life. In these tests, the authors observed that at strain amplitudes equal to 1.0%, the resultant mean stress at half-life relaxed to zero both in tension and torsion. On the other hand, for tests with a lower strain amplitude (0.5%), they observed that the mean stresses did not completely relax. When the authors compared the fatigue data of fully reversed and zero-tension tests, they observed that the fatigue life of the latter substantially reduced on tests under the lower strain amplitude, and no difference was noted on tests conducted with the higher strain amplitude. Based on this, the authors suspected that the mean stresses could affect fatigue life, although no fatigue model accounted for this effect at the time. To this end, they modified the model proposed by Kandil, Brown, and Miller [44], including a term that would represent the mean stresses effects. The parameter proposed was based on Brown and Miller's critical plane approach [45] and is presented below,

$$\hat{\gamma}_p + \hat{\varepsilon}_{pn} + \frac{\hat{\sigma}_{n0}}{E} = \text{constant}, \quad (2.1)$$

where $\hat{\gamma}_p$, $\hat{\varepsilon}_{pn}$ and $\hat{\sigma}_{n0}$ are the plastic shear strain amplitude, the normal strain amplitude, and the normal mean stress on the plane of maximum shear strain amplitude, respectively, and E is the Young's modulus. As a result, the fatigue parameter successfully correlated the fatigue life of Inconel 718, despite the limited amount of data available. Moreover, the authors observed that the resulting equation was consistent with their conclusion that mean stresses do not change the crack direction, only influencing fatigue life.

In the same year, aiming to investigate the effects of the mean stress on fatigue crack growth, Socie and Shield [17] performed axial-torsional fatigue tests on tubular specimens taken from a forged ring of Inconel 718. They intended to submit this material to different loading conditions with non-zero prescribed mean strains to validate the model proposed by Socie et al. [16], which captured the effects of mean stresses. A year later, continuing the fatigue testing campaign on Inconel 718, Socie et al. [18] tested a wider variety of multiaxial loading paths to validate

this model for lower strain levels, conditions in which the plastic strains are negligible. To this end, the authors conducted proportional and non-proportional strain-controlled fatigue tests at room temperature, using fifteen loading paths with different combinations of axial and shear strain ratios, including out-of-phase loadings, as seen in Fig. 2.15. In all tests, they observed

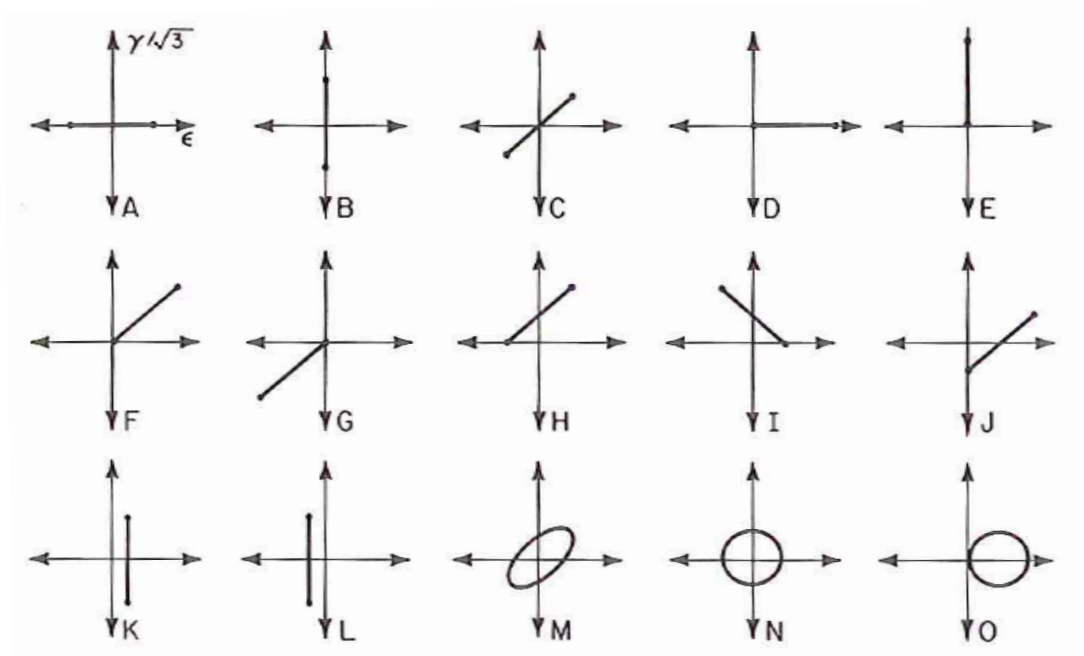


Figure 2.15 Loading paths used by Socie and co-authors [16–18] to investigate the fatigue behavior of Inconel 718.

that failure and other cracks formed on or near the maximum shear strain amplitude plane that had the largest normal mean stress. According to the authors, this result is consistent with the failure mode of Inconel 718, which fails by Mode II shear cracks for tension, torsion, and proportional loadings. Furthermore, the crack growth behavior of each test was monitored using a replicating technique, which allows determining the crack characteristics for a given loading cycle. Based on this, the authors determined the influence of the mean stress on crack growth over fatigue life, in which different growth rates were observed for tests with positive and negative mean stresses, as shown in Fig. 2.16. The authors noted that shear loads could be transmitted by the irregularly shaped crack surfaces as a result of a mechanical interlocking effect. Consequently, they concluded that the tensile mean stresses normal to the crack should decrease this effect, resulting in a higher growth rate. Moreover, they observed that the cyclic tensile strain perpendicular to a shear crack enhances its growth, especially if the mean normal strain produces a mean stress. The authors confirmed that mean stresses determined the preferred

maximum shear amplitude plane, crack distribution, and fatigue life, not affecting the failure mode and crack directions. Finally, Eq. (2.1) was expressed in terms of a Coffin–Manson type equation and calibrated with fully reversed torsional data. Most tests demonstrated a good correlation with the damage model proposed, as seen in Fig. 2.17. Exceptions were the out-of-phase tests, in which the model was not able to account for the large amounts of plasticity.

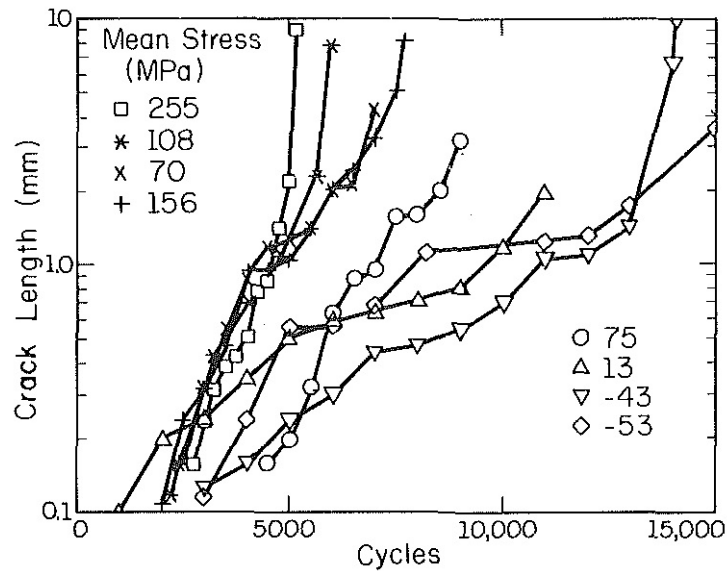


Figure 2.16 Influence of mean stress on the crack growth rate. Image taken from Socie and Shield [17].

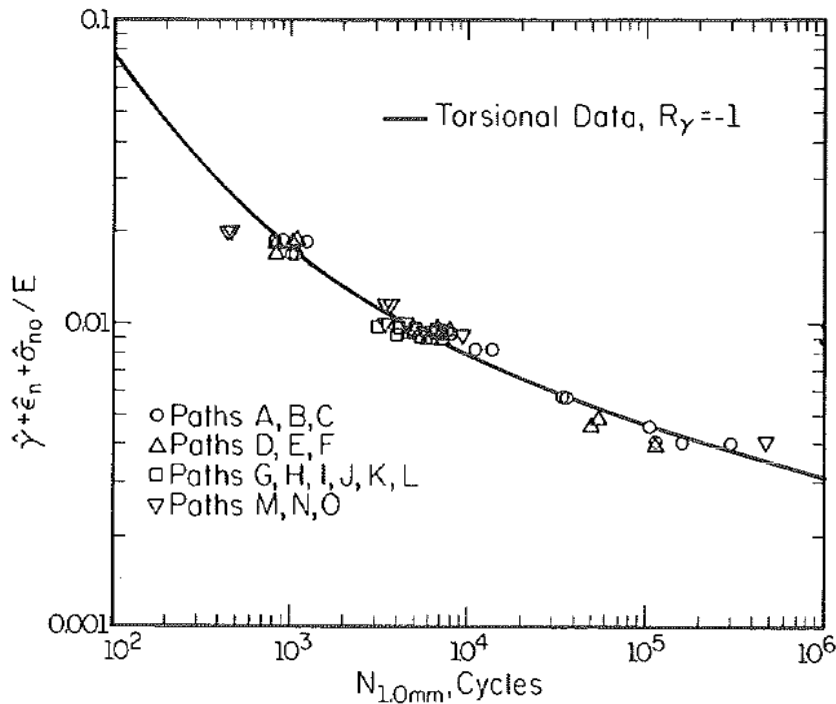


Figure 2.17 Correlation of Inconel 718 fatigue test data with the fatigue damage model proposed by Socie et al. [16] (Eq. 2.1). Image taken by Socie et al. [18].

In 1988, Fatemi and Socie [19] proposed one relevant multiaxial fatigue parameter, also based on the critical plane approach. The parameter applies to materials and/or loading conditions that result in failure by shear cracks, which is the failure mode of Inconel 718. In this case, fatigue cracks initiate at the maximum shear strain planes under different loading conditions. The authors found that non-proportional or out-of-phase loading conditions were more damaging than the equivalent in-phase loading in the low cycle region. In addition, they observed that some materials presented the phenomenon of cyclic hardening during out-of-phase loading, resulting in substantial fatigue damage. Aiming to account for this effect, they proposed that the fatigue parameter must include the maximum normal stress σ_{nmax} present at the maximum shear plane, which contains the maximum shear strain, γ_{max} . Note that the influence of the mean stress is taken into account in this criterion since the maximum normal stress σ_{nmax} is the sum of the mean value and amplitude of the normal stress. To confirm this parameter particularity, the authors successfully correlated this approach with Inconel 718 mean stress data taken from axial-torsional fatigue tests carried out by Socie et al. [16] and Socie and Shield [17]. Lastly, the authors pointed out that the combination of materials and loading conditions result in different cracking modes, making it unlikely that any theory with fixed parameters would be applicable in all multiaxial fatigue situations.

Shortly after, Fatemi and Kurath [20] published a study assessing the influence of the mean stress on life prediction using the Fatemi-Socie fatigue parameter. To this end, fatigue data from a wide variety of loading paths applied to Inconel 718 and 1045 steel were compared with life predictions made with this parameter, formulated with the Coffin–Manson relation. Non-zero mean stress or strain conditions were prescribed among the loading paths tested. Corroborating some of the conclusions obtained by Fatemi and Socie [19], the authors observed that data were successfully correlated with the parameter for these materials, indicating that the effects of mean-stresses were also well described. Apart from that, they noted that mean-stresses could influence fatigue life significantly if they do not relax, although the mean-strains were not detrimental to fatigue life if total mean stress relaxation occurs. According to the authors, this behavior was also accounted for in the fatigue parameter proposed.

Years later, in 2010, Filippini et al. [23] investigated the multiaxial fatigue behavior of Inconel 718 at high temperatures. Intending to simulate the operational conditions of this

material in turbine engine components, the authors conducted axial-torsional fatigue tests at 540 °C within the fatigue life limits from 2×10^3 to 2×10^5 cycles. A large variety of loading paths were carried out with different combinations of axial and shear strain ratios, including non-proportional in-phase and out-of-phase tests, as shown in Fig. 2.18. Observing the cyclic behavior of this material, the authors registered elastic shakedown during all strain amplitudes tested and concluded that the transition from a predominantly elastic-plastic to a mainly elastic behavior occurs in less the 5×10^2 cycles. The authors also drew attention to the use of pseudo-stresses in fatigue life prediction criteria. When the material behaves within the linear elastic regime, pseudo-stress components can be obtained by multiplying the applied strain by the appropriate elastic moduli. Considering the cyclic behavior of this material in the fatigue life range of interest, the authors defended the consistency of using a damage parameter applied in terms of pseudo-stresses due to the simplicity of its calculation. Therefore, life estimates were performed using the Fatemi–Socie [19] and Smith–Watson–Topper (SWT) [26] fatigue parameters. The former model was selected for cases in which the material fails by shear cracks, characterized to be the typical behavior of Inconel 718 according to Socie and Shield [17]. However, the SWT parameter was selected for cases in which the failure mode is governed by tensile cracks. According to Filippini et al., early life is controlled by cracks that grow on planes perpendicular to the maximum principal stress and strain, which naturally leads to the SWT model, defined by the maximum stress and the cyclic strain range. The authors also used the Manson–McKnight model to make life predictions. As a result, it was shown that all models predicted more conservative fatigue life estimations.

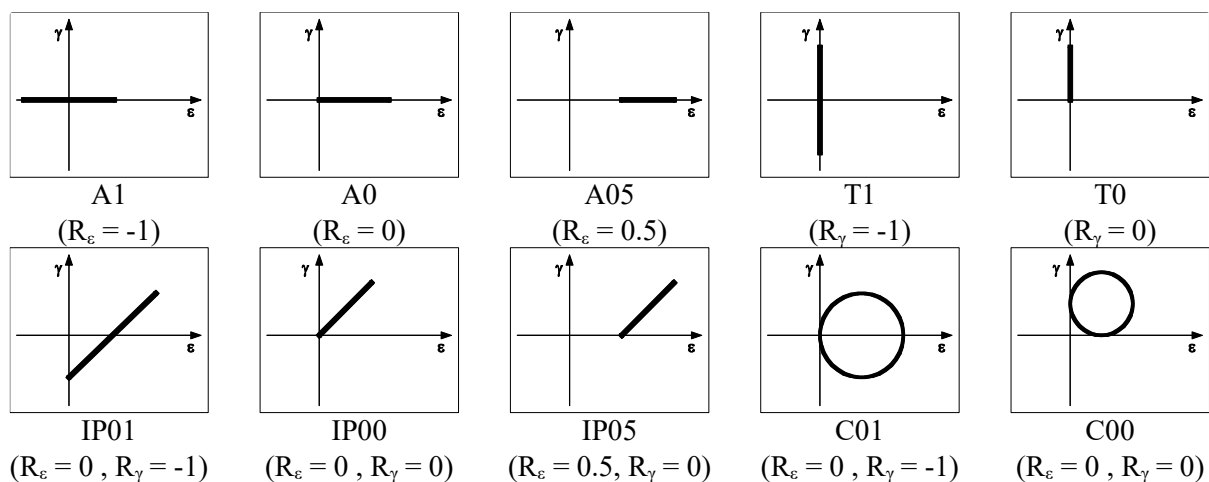


Figure 2.18 Loading paths tested by Filippini et al. [23].

In 2019, Sun and Yuan [21] conducted several experiments to assess the effects of multiaxial thermomechanical fatigue (TMF) on Inconel 718. Strain-controlled proportional and non-proportional axial-torsional fatigue tests were conducted within a temperature range from 300 to 650 °C. In addition, the authors also considered conditions in which the mechanical and thermal loadings were applied in-phase and out-of-phase. Since creep is not seen in this material up to 650 °C, the authors ignored the strain rate effects and treated Inconel 718 as rate-independent. They also observed that temperature variation changed the fatigue performance of the material significantly. After scanning electron microscope (SEM) analysis, the authors determined a trend for the failure mechanism of Inconel 718 under multiaxial thermomechanical fatigue: they noted that transgranular fracture occurs mainly at low temperatures, while intergranular fracture occurs predominantly under high tensile stress and high temperatures. The multiaxial TMF life of Inconel 718 was predicted by some well succeed isothermal fatigue parameters, such as the Brown–Miller, Fatemi–Socie, Smith–Watson–Topper, among others models. As a result, the data of all tests were widely scattered in the predicted life versus experimental life plot, indicating that all models were unsatisfactory in predicting multiaxial TMF life. Aiming to include the effects of varying temperatures and predict thermomechanical fatigue life more accurately, the authors proposed a new fatigue model based on Liu’s virtual strain energy model [46]. After introducing a correction term for the multiaxial TMF load, this model provided a significantly better agreement with the experimental data, also giving a uniform prediction for both isothermal and thermomechanical fatigue.

3 | Experimental program

3.1 Material and specimen

The material investigated in this study is the Inconel 718 nickel-based superalloy which is widely used in the aircraft industry due to its superior mechanical properties at high temperatures. Thin-walled tubular specimens were extracted from the tangential direction of an as-forged turbine disk. This type of specimen was chosen because the axial and shear stress distributions over the wall thickness can be considered uniform and, consequently, is well-known over the entire gauge length. The geometry and dimensions used during its machining process were based on the ASTM E2207 [47] standard and are presented in Fig. 3.1. The inner and outer diameters of the tubular test specimen are $\phi_i = 10$ and $\phi_o = 12$ mm, respectively, resulting in a thickness of 1 mm. Furthermore, the disk was heat-treated by direct age as follows: first, the specimen was aged at 720 °C for 8 h, followed by another ageing at 620 °C for 8 h, and finally air-cooled.

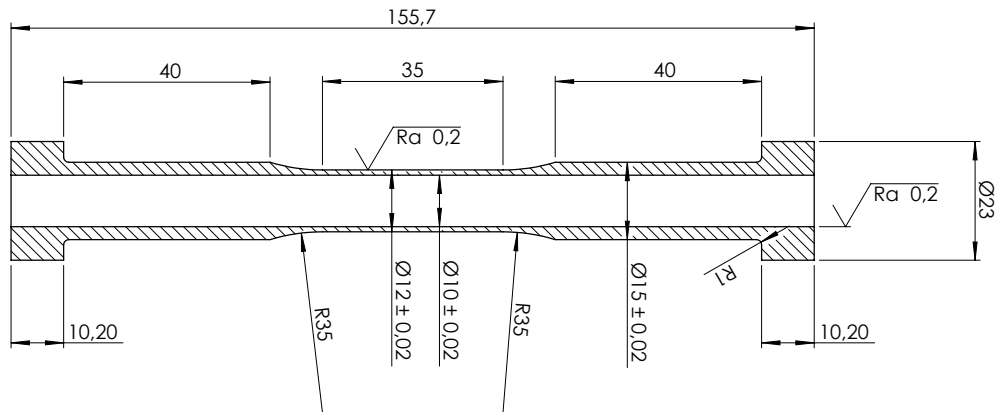


Figure 3.1 Thin-walled tubular specimen used in the fatigue tests, all dimensions in mm.

The microstructure of Inconel 718 was characterized from the observation of the three metallographic planes perpendicular to the axial, tangential, and radial directions of the specimen, as shown in Fig. 3.2. The surfaces of a sample taken from the gauge section of a specimen were ground using sandpapers with the following grits: 120, 220, 320, 400, 600, 800,

1200, and 2000. Finally, the surfaces were polished with 1 μm diamond paste and 0.1 μm colloidal silica and chemically attacked to reveal the grain boundaries. To this end, samples remained immersed for one minute in the Kalling compound n^o 2 recommended in Ref. [48], whose composition is: 100 mL ethanol + 100 mL HCl + 5 g CuCl_2 . Figure 3.2 also presents the microstructure of Inconel 718, showing homogeneous and equiaxed grains in all directions, with no preferential texture usually generated during the machining process. The average grain size, determined from the lineal intercept method described by the ASTM E112-13 [49], was equal to 5 μm for all planes considered. Thus, there are approximately 200 grains along the thickness, which is above the minimum value of 10 grains recommended by the ASTM 2207. Fig. 3.3 shows in detail as-polished and chemically attacked microstructures of Inconel 718, recorded by an Olympus LEXT OLS4100 optical microscope. Inclusions can be seen in the nickel matrix, located mainly at grain boundaries and characterized by different shapes, sizes, and colors. Although we were not able to accurately identify each of the precipitates, we defined some of them based on comparisons with works of literature that performed a more rigorous metallographic analysis. According to the proposition of some authors [12, 38, 40, 50, 51], we suggest that the largest precipitates are MC-type carbides, M being mostly Nb and Ti, while the smallest ones are the orthorhombic δ -phase (Ni_3Nb), which present a needle-like morphology at the grain boundaries and the form of a fine block inside the grains.

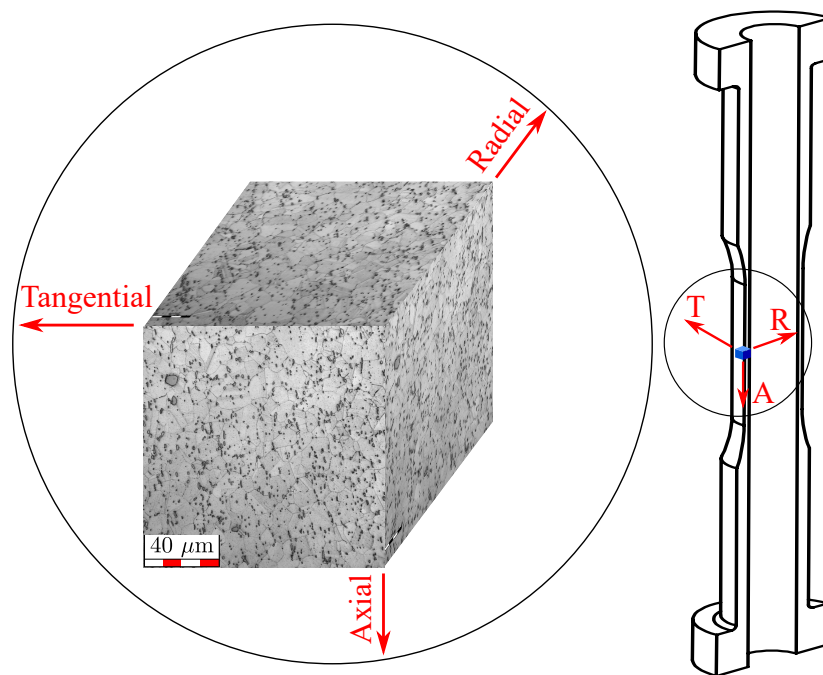


Figure 3.2 Stereographic microstructure of forged Inconel 718.

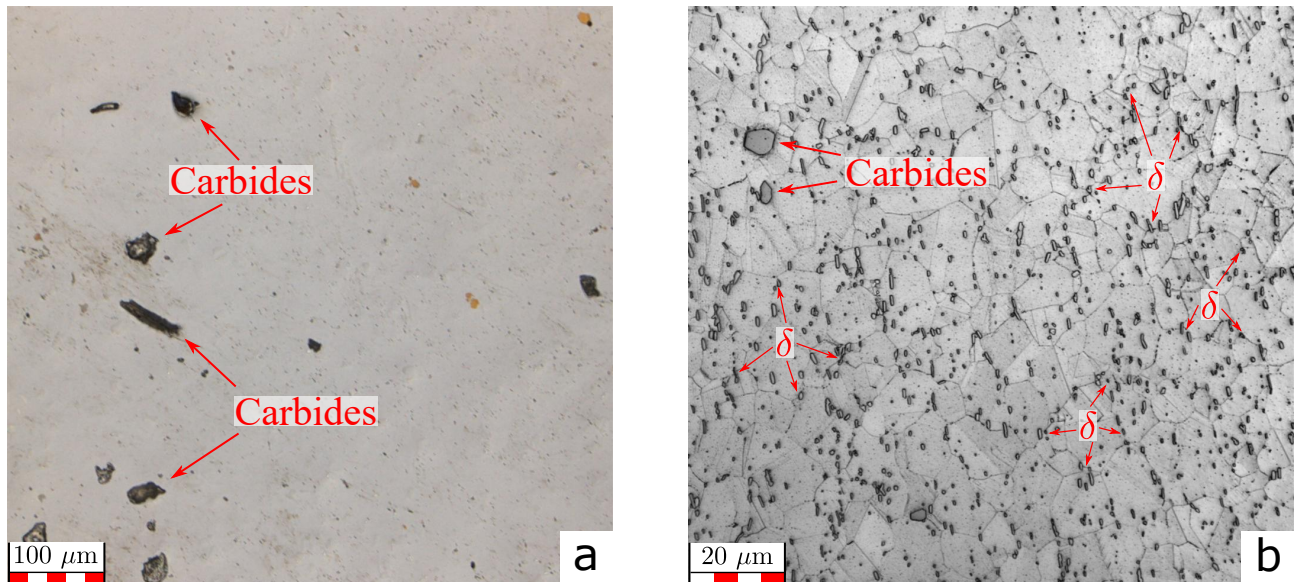


Figure 3.3 As-polished (a) and chemically attacked (b) microstructure of Inconel 718.

A total of 36 specimens were received from Safran. To check if its dimensions followed the specifications, the diameters and roughness of some specimens were measured repeatedly. A TESA analog micrometer with 0.01 mm resolution was used to take three measurements of the inner and outer diameter of the specimens selected, confirming their correct fabrication. The surface roughness R_a was verified at an Olympus LEXT OLS4100 3D laser measuring microscope by three roughness measurements taken from the external diameter of the gauge region of each specimen. All measurements were within the range of 0.02 - 0.15 μm , below the maximum value of 0.2 μm recommended by the ASTM 2207. Table 3.1 shows the diameters and roughness values measured during the quality control process of the received specimens. Very low variability was observed for the measurements made in each specimen.

3.2 Fatigue testing system

The fatigue tests were conducted on a high-temperature testing system developed by MTS (Fig. 3.4). Mechanical loading was applied using an MTS Model 809 servo-hydraulic machine, which can impose axial/torsional loading on the specimen under analysis. This machine has a capacity of ± 100 kN for axial force and ± 1100 N·m for torque. An MTS 653 dual-zone resistance furnace capable of operating at temperatures up to 1400 °C was used as the heating system, responsible for increasing the temperature of the specimen. This furnace surrounds the

Table 3.1 Inner and outer diameters and roughness measured in the gauge length of some specimens

Specimen ID	ϕ_i [mm]	ϕ_o [mm]	R_a [μm]
4A1	9.99	12.01	0.11
	9.99	11.98	0.13
	9.99	12.00	0.12
7A1	9.99	11.99	0.14
	9.99	12.01	0.11
	9.99	11.99	0.12
1D3	9.99	11.99	0.03
	9.99	11.99	0.04
	9.99	11.98	0.04
3C2	9.99	11.99	0.04
	9.99	11.98	0.05
	9.99	11.98	0.03
5C4	9.99	12.00	0.03
	9.99	11.98	0.02
	9.99	11.98	0.02
1D1	9.99	11.99	0.02
	9.99	11.97	0.03
	9.99	11.99	0.03

specimen and has a refractory material inside, ensuring an adequate thermal seal. In addition, it is capable of generating a temperature gradient between the two zones, although all tests were conducted under isothermal condition. Considering that all tests started in strain-control mode, strain measurement was performed using an MTS high-temperature axial/torsional extensometer model 632.68 (Fig. 3.5), which has an axial and torsional range of $\pm 10\%$ and $\pm 5^\circ$, respectively. There are also two cooling systems installed: one for the high-temperature axial/torsional extensometer and other for the collet grip.

The extensometer rod tip is assembled in the specimen over small indentations made with an indentation tool provided by MTS. According to the guidelines provided by the manufacturer, the indentation tool is positioned in the middle of the gauge length and the metallic half-sphere located on its upper part is stroke by a hammer, generating the indentation marks on the specimen. Remembering that the wall thickness in the gauge section is 1 mm, special attention must be given to this step since a stress concentration point can be created depending on the depth of the indentation mark made. As a result, cracks may nucleate at the indentation marks, invalidating the test. Fig. 3.6 shows an invalid room temperature traction test where the failure



Figure 3.4 High-temperature axial/torsional testing system used in the fatigue tests.

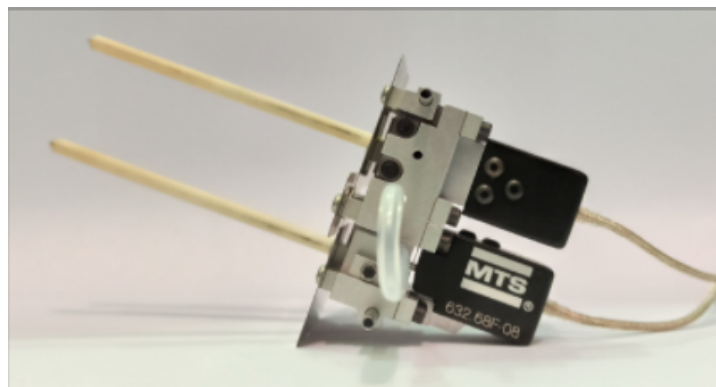


Figure 3.5 High-temperature axial/torsional extensometer used to measure and control the axial and shear strains over the gage length of the specimen.

crack is located at a deep indentation mark which possibly became a stress concentrator that affected the fatigue life. Therefore, the force applied in the tool must be well controlled in order to generate the smallest possible marks capable of safely positioning the extensometer.

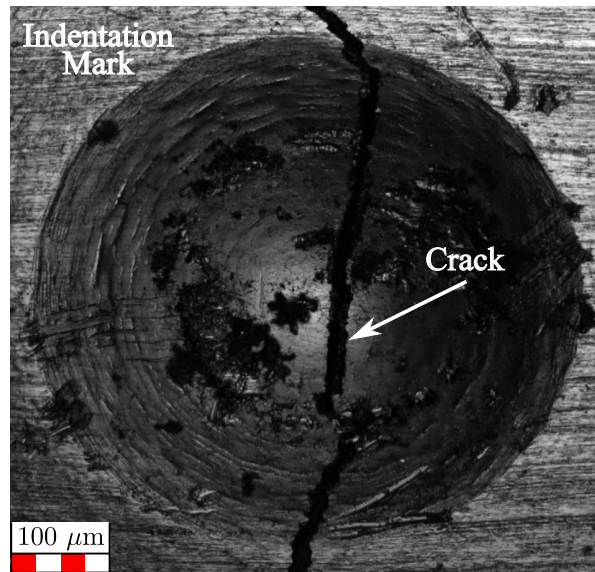


Figure 3.6 Failure at the indentation mark made on specimen 4A2, which was tested at room temperature under uniaxial loading. The indentation marks are used as a reference for positioning the extensometer on the specimen.

The drawback seen in this method was the difficulties in controlling the force when striking, causing its replicability to be unreliable. Aiming to prevent this situation, an alternative procedure was developed to standardize the indentation process. The new method consists of fixing the indentation tool in a specimen with a rubber band, using a bench vise to press one against the other. The replicability was guaranteed by turning the auger screw of the vise at a specific angle so that the same indentation mark could be replicated in different specimens. A protractor was used to measure the rotation angle of the vise crank, while the geometries of the generated indentation mark were determined with an Olympus LEXT OLS4100 3D laser measuring microscope in order to establish a relation between the applied angle and the size of the indentation mark. Fig. 3.7 presents a schematic image of the attachment of the indentation tool on a specimen and its assembly in a bench vise during the indentation procedure. After the first fatigue tests, it was observed that a rotation of the vise crank at an angle of 8° resulted in a reliable indentation mark with a depth of approximately $25 \mu\text{m}$, capable of being used to safely position the extensometer. However, it is not guaranteed that there will be no indentation failure, although unexpected.

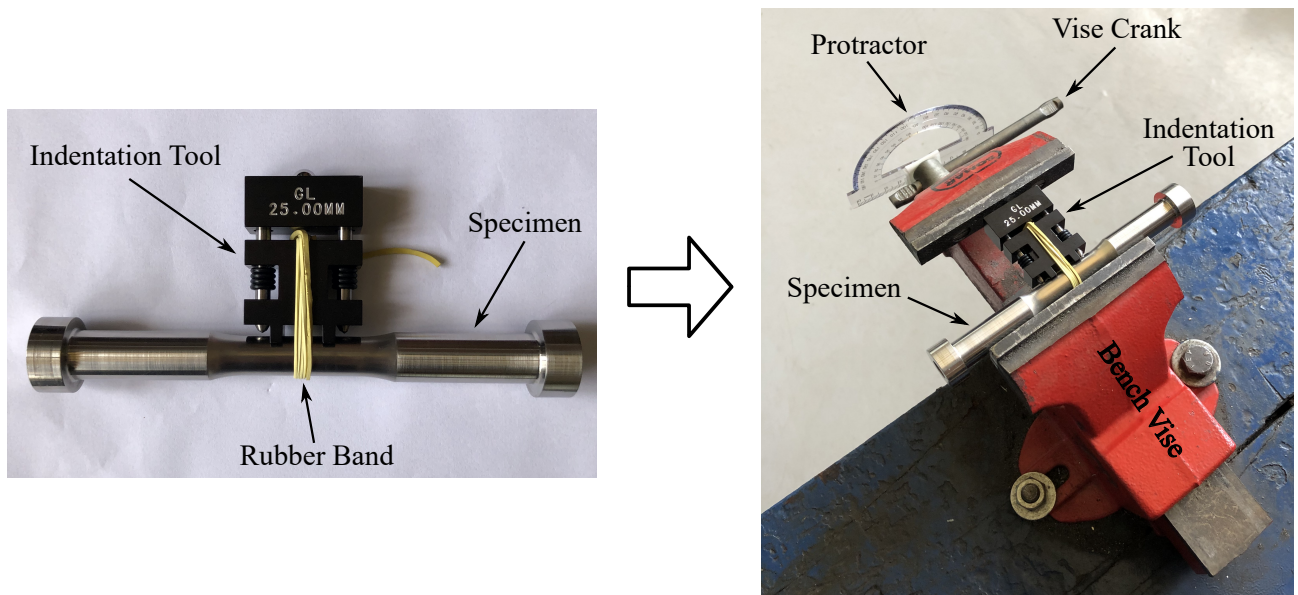


Figure 3.7 Photos of the attachment of the indentation tool on the specimen and its assembly in the bench vise.

3.3 Procedure for calibration of the test temperature

The high-temperature tests were conducted at 450 °C, meaning that this was the desired temperature at the gauge length of the specimen. Preliminary tests were carried out on a dummy Inconel 718 specimen to calibrate its temperature with the furnace temperature control. The furnace temperature was controlled by using fixed K-type thermocouples (Fig. 3.8) while the specimen temperature was monitored by K-type thermocouples welded on its gauge section and gauge ends, the latter being the position just after the gauge transition radius (Fig. 3.9).

The test temperature was achieved before the beginning of the fatigue test, with a 15-minute temperature ramp followed by a 30-minute isotherm. It was concluded that it would be necessary to impose a furnace temperature of 550 °C to reach the desired test temperature at the gauge length. The measurements of each thermocouple along the gauge region were registered after the temperatures have achieved steady-state values and are presented in Table 3.2. It should be noted that there is a thermal gradient in the gauge region, but its average temperature is 450 °C. A deviation of 6% between the temperatures measured at the UG, MG, and LG points of the gauge length is observed. Furthermore, a difference of 25% between the average temperature at gauge length (average between temperatures measured at the UG, MG, and LG points) and the average temperature measured at both gauge ends (UE and LE points) was noted, setting

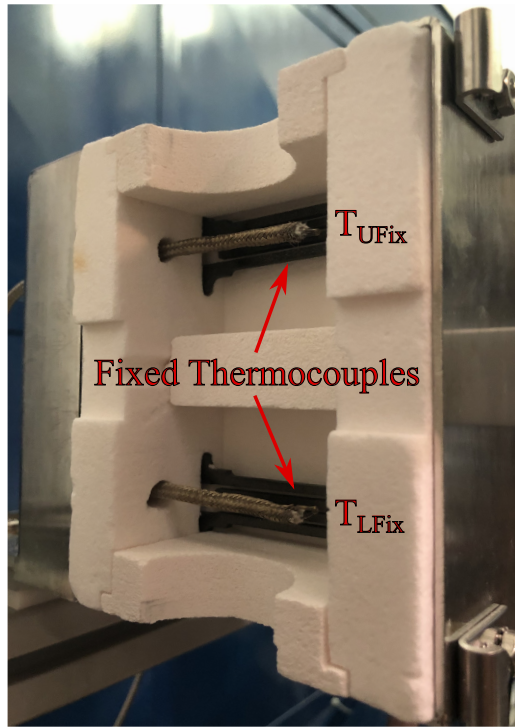


Figure 3.8 Fixed K-type thermocouple used to control temperature during tests.

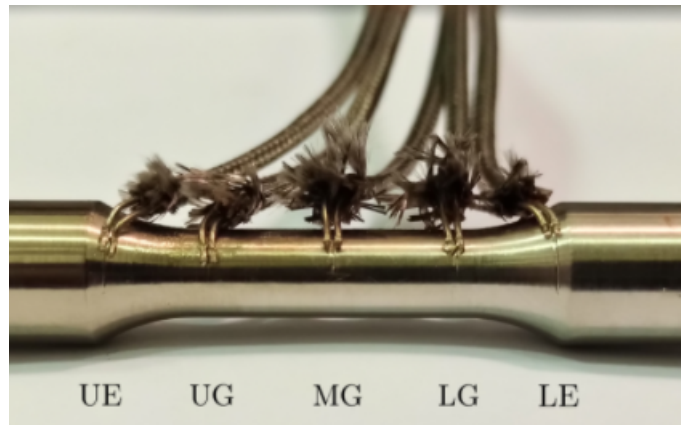


Figure 3.9 Position of the K-type thermocouples welded into the specimen: Upper End (UE), Upper Gauge (UG), Middle Gauge (MG), Lower Gauge (LG), and Lower End (LE).

up a relation between the temperatures at the two specimen sections.

Table 3.2 Temperature [$^{\circ}\text{C}$] measured by the fixed (T_{UFix} and T_{LFix}) and welded (T_{UE} , T_{UG} , T_{MG} , T_{LG} , and T_{LE}) thermocouples for a furnace temperature control of 550°C .

T_{UFix}	T_{UE}	T_{UG}	T_{MG}	T_{LG}	T_{LE}	T_{LFix}
550	378	439	467	440	354	550

It is important to mention that no thermocouple was welded at the gauge length of the specimens during fatigue testing. The procedure mentioned previously was adopted only once, aiming to establish a relation between the furnace temperature and the temperature of the

welded thermocouples. Welding at the gauge region would probably generate weak points in the specimen, leading to shorter fatigue lives. Therefore, in order to conduct the fatigue tests with accurate test temperature and avoid affecting the fatigue results, thermocouples were welded only at the Upper End (UE) and Lower End (LE) positions of the specimen. Based on Table 3.2, there is a difference of 50% between the average temperatures measured by the control thermocouples (T_{UFix} and T_{LFix}) and the ones welded on the gauge ends (T_{UE} and T_{LE}). This difference was set as a check parameter observed before the fatigue test to ensure that the test will be performed under the correct temperature conditions.

It is worth noting that during the heating period, described by the 45 minutes spent on the temperature ramp and the isotherm, the thermal expansion of the specimen was not restricted to avoid residual forces prior to the fatigue test. This expansion was measured by the extensometer after the end of the isotherm, always resulting in a dilatation of 0.6%. This value was used as another check parameter to ensure that the gauge section achieved the correct testing temperature, guaranteeing the replication of the temperature conditions in all tests.

3.4 Fatigue test procedure

The fatigue behavior of the Inconel 718 extracted from an as-forged turbine disk was assessed in the experimental campaign. Traction, torsion, and proportional traction-torsion fatigue tests were carried out at room temperature and 450 °C. In a rotating disk, the tangential stress component is significant, a condition that can be reproduced by pure traction tests conducted on specimens taken from the disk's tangential direction. Moreover, some parts can be exposed to a multiaxial stress state similar to that obtained in traction-torsion tests. Therefore, three loading paths were chosen for representing the stress states experienced by the component of interest in this study. The loading paths are shown in Fig. 3.10 in a $\varepsilon - \gamma/\sqrt{3}$ space, where ε is the axial strain and γ is the shear strain at the specimen surface. A strain ratio $R_\varepsilon = R_\gamma = 0$ was used in all tests.

After installing the specimen and positioning the extensometer, the test procedure was divided into three consecutive steps: 1) installation verification, 2) specimen heating, and 3) fatigue test. The first step was to check if the extensometer was correctly mounted on the

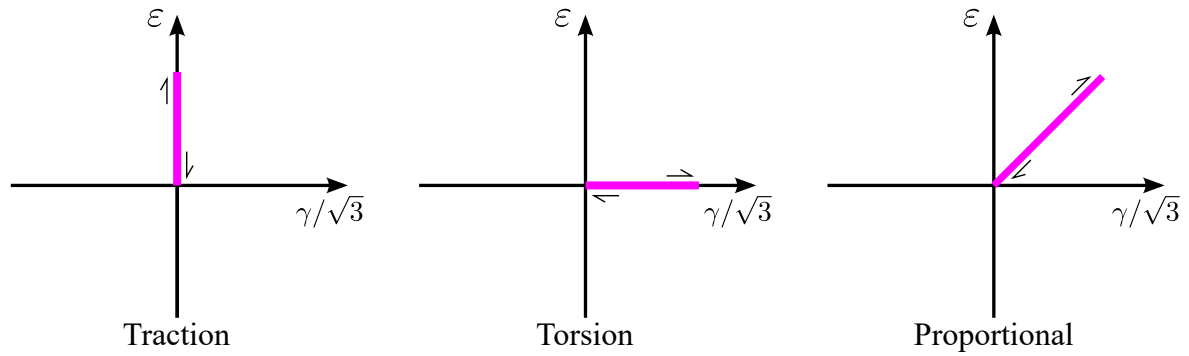


Figure 3.10 Loading paths used in the fatigue tests.

specimen. An axial fatigue load with a maximum value equal to 6 kN was cycled 20 times, followed by a torque of 10 N·m that also lasted 20 cycles. Loads applied during this step were within the elastic domain and were small compared to the loads to be tested, thus not affecting the mechanical behavior evaluation of each specimen. The second step was only adopted for the high-temperature tests. In this step, the control thermocouples were gradually heated from room temperature to 550 °C in a temperature ramp of 15 minutes. Then, the temperature was maintained in this isotherm for 30 minutes, which was enough time for the target temperature of 450 °C to be stabilized in the gauge length of the specimen. The system was kept under zero force control during this step so that the specimen did not suffer loads associated with the effect of its thermal expansion. This procedure was used to guarantee that only the stresses generated by the mechanical loads would cause fatigue damage.

Lastly, the fatigue test is started. Since elastic shakedown was observed in the material response after the first loading cycle, it was decided to change the control mode to force/torque after the initial transient regime and to use the maximum and minimum force/torque values recorded after stabilization. The elastic shakedown behavior is exemplified in Fig. 3.11, which shows the stress-strain hysteresis loops of a uniaxial test conducted at a strain amplitude $\varepsilon_a = 0.35\%$ and $R_\varepsilon = 0$. The change in the control mode was motivated by the possibility of using higher loading frequencies, thus enabling to reduce the test duration. Based on these considerations, the fatigue test was divided into two phases: the strain-controlled phase, followed by the load-controlled phase. The strain values used in each test during the strain-controlled stage were chosen to obtain a life between 10^4 and 10^6 cycles, which is a typical order of magnitude for the fatigue life of the component of interest in this study. Actually, the prescribed

strains were obtained from pseudo-stresses previously defined by Safran (undisclosed due to industrial secrecy) to impose equal or similar conditions of loading levels on the three loading paths studied. This approach assumes the presence of purely elastic behavior of the material, which is suitable with the cyclic behavior of Inconel 718 since elastic shakedown was observed for all applied strain levels [23]. Therefore, the prescribed axial and shear strains were calculated by dividing the corresponding pseudo-stresses by the appropriate elastic moduli.

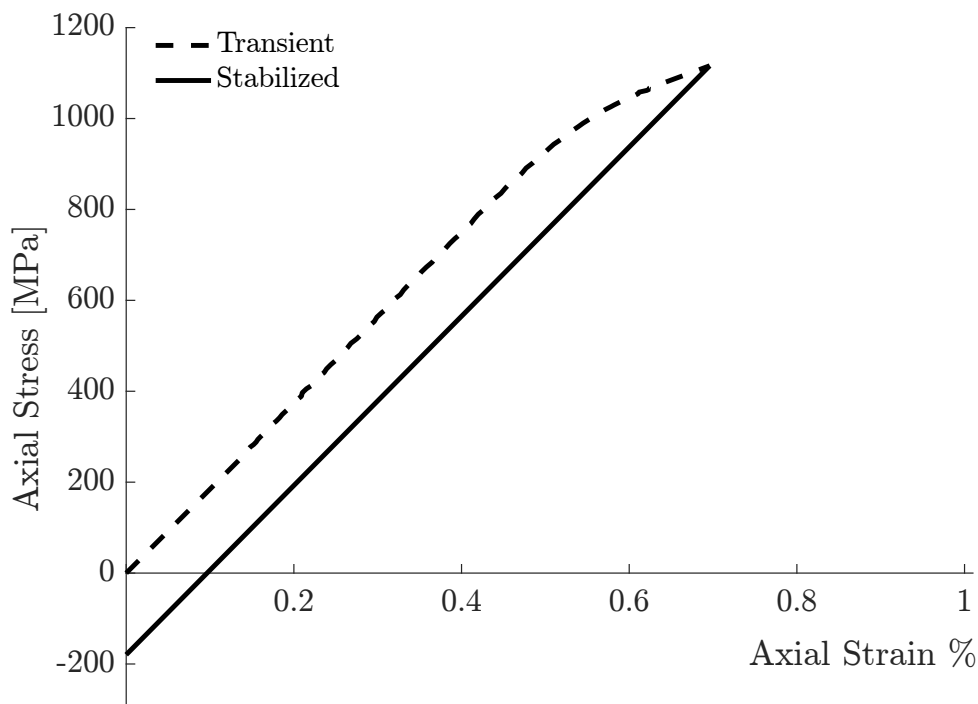


Figure 3.11 Stress-strain response of a uniaxial test conducted at $\varepsilon_a = 0.35\%$ and $R_\varepsilon = 0$, which shows elastic shakedown after the first loading cycle.

Each test condition was replicated at least one time to assess the dispersion of the fatigue lives. The loads were applied in the form of sine waves, having a 0.5 Hz frequency during the strain-controlled phase and 0.5 to 5 Hz in the load-controlled stage. The stopping criterion of the strain-controlled tests was a drop in the stabilized loading magnitude. In tests controlled by force or torque, this criterion was a minimal variation in the stabilized axial/angular displacement of the collet of the machine, which is the component that attaches the specimen to its servo-hydraulic piston. After a test was stopped, a macroscopic (millimeter scale) crack was observed on the surface of the specimen. Fig. 3.12 illustrates the stopping criterion for a strain-controlled test and the subsequent detection of a superficial crack, characterizing the failure of the specimen.

As a consequence of transient effects related to the testing control, the stress response of the first cycles was omitted since it does not represent the material behavior.

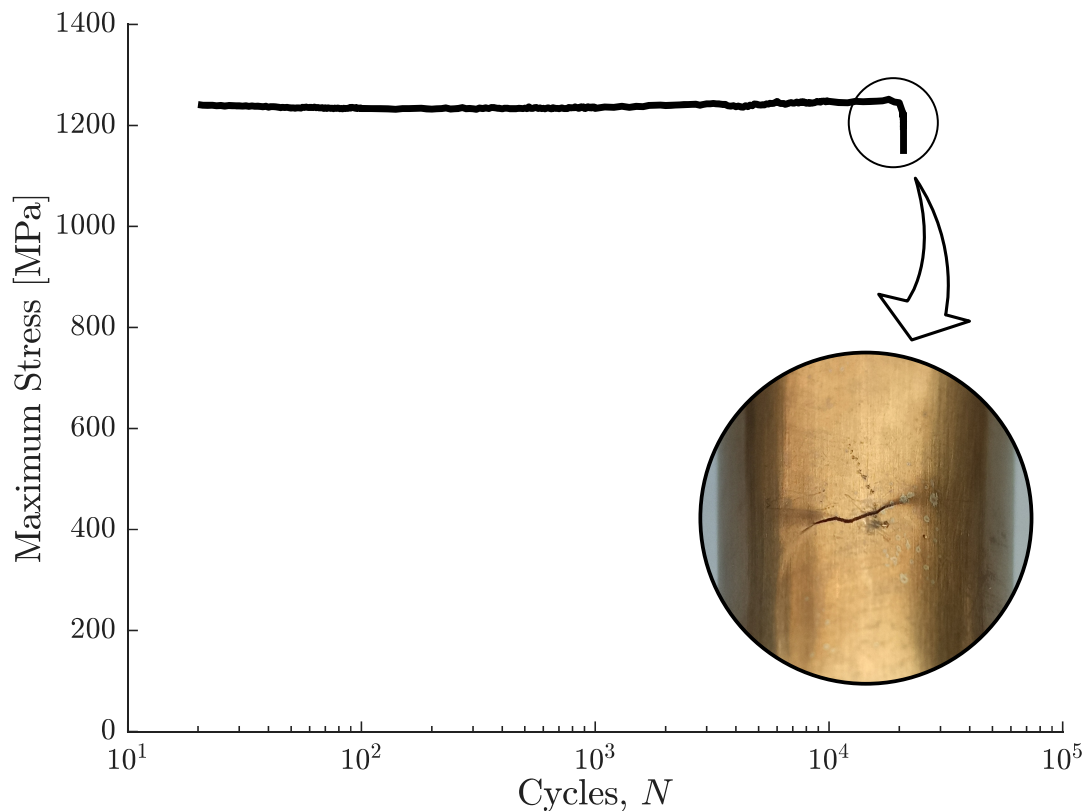


Figure 3.12 Schematic of the load-drop criterion used to stop a strain-controlled fatigue test. The inset shows the crack observed in the specimen after the interruption of the test.

The strain-controlled tests were performed with a tool that enables the automation of tasks in the fatigue tests, called MTS TestSuitTM Multipurpose Elite. This software allowed the interconnection of all steps of the test routine so that they automatically proceeded one after the other. Thus, after confirming the correct installation of the extensometer, the furnace is turned on to heat the specimen and, finally, start the fatigue test in an automated manner. In tests with mixed control mode, the force/torque-controlled phase was performed with the MTS Basic TestWareTM tool, which is an interface that allows to create test programs that do not require complex loading histories.

4 | Results and discussion

4.1 Fatigue test results

The experimental data obtained by testing the thin-walled tubular specimens at room temperature and 450 °C are summarized in Table 4.1. Note that all stress and strain values presented were normalized due to industrial secrecy. The stress quantities shown in this table were determined from the stabilized stress response of the material. The number of loading cycles to failure, N_f , was automatically recorded considering a load-drop criterion in the strain-controlled tests and a displacement-increase criterion in the force-controlled tests. In both cases, a visible crack was detected at the specimen surface at the end of the test. It is worth mentioning that some cracks nucleated at the indentation mark used to position the extensometer, invalidating the test. The stress quantities reported are the average axial stress and the average shear stress, which were calculated by assuming uniform axial and shear stress distributions over the wall thickness. All tests were replicated under different loading frequencies aiming to assess its influence on the fatigue response of Inconel 718. Minimal differences were observed in fatigue lives from tests conducted at both temperatures. Therefore, it was concluded that the fatigue response of this material is rate-independent within the tested loading frequencies, which ranged from 0.5 to 5 Hz.

Figure 4.1 shows the fatigue life data for all the loading paths and temperatures investigated in terms of the equivalent von Mises strain amplitude defined as $\Delta\varepsilon_{eq}/2 = \sqrt{(\Delta\varepsilon/2)^2 + (\Delta\gamma/2)^2}/3$. This parameter is widely used for presenting strain-life curves under multiaxial loading conditions [52, 53]. Note that only valid tests were plotted since the fatigue life obtained from tests that failed at the indentation mark may be biased. The results in Fig. 4.1 indicate that for the same loading path and the same (or nearly the same) equivalent strain amplitude, the fatigue lives of the tests at 450 °C are longer than those of the tests at room temperature. The difference

observed is up to four times in traction, six times in torsion, and three times in proportional tests. Although these results are unprecedented for the torsion and proportional tests, the traction ones are consistent with literature data [8, 12]. In general, it was found that the torsion tests had the longest lives for both temperatures in all strain amplitudes considered, followed by the proportional and traction tests. This trend was easily observed in the results at room temperature, although not so clear for data at 450 °C, which were more scattered.

The fatigue life data was also presented in terms of the equivalent pseudo-von Mises stress amplitude defined as $\Delta\sigma_{eq}/2 = \sqrt{(\Delta\sigma/2)^2 + 3(\Delta\tau/2)^2}$, as shown in Fig. 4.2. This approach is only possible when considering that the material presents a linear elastic behavior. In this case, the normal and shear stress amplitudes are determined by multiplying the prescribed axial and shear strains amplitudes by their respective elastic moduli. Observing the stress-strain response of Inconel 718, in which elastic shakedown occurs after the first cycle, it is convenient to use such an approach to correlate the fatigue lives of this material. Due to its simplicity and effectiveness, the industry commonly uses this method to determine the stresses state of components made of Inconel 718. Looking for the results presented in Fig. 4.2, the trend observed was that torsion tests lasted more for a given pseudo-von Mises stress amplitude, regardless of the test temperature. Again, this conclusion is clear when considering only data of room temperature tests. In addition, for the same pseudo stress, little difference was noted when comparing the fatigue lives of the traction tests of both temperatures. The same was observed in the torsion tests, although the fatigue lives of room temperature proportional tests were shorter than at 450 °C under this point of view.

It is interesting to note that the two approaches used to represent the strain-life curves led to a different conclusion about the fatigue response of this material when considering each of the loading paths at both temperatures. In view of the equivalent von Mises strain amplitude approach, the fatigue lives of the room temperature test were shorter than at 450 °C regardless of the loading path, which was not observed when using the pseudo-von Mises stress amplitude. Despite that, it can also be noted that neither the equivalent strain amplitude nor the pseudo-von Mises stress amplitude is an appropriate parameter to correlate test data at the same temperature. This is because different loading paths having the same (or nearly the same) equivalent strain/stress amplitude yielded significantly different fatigue lives.

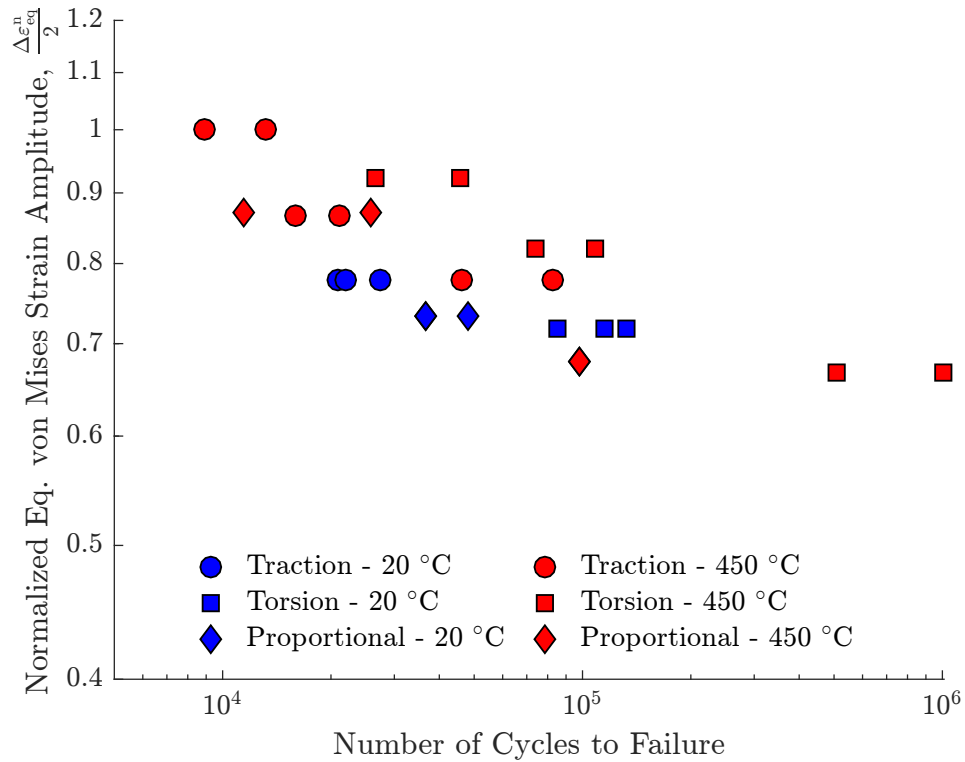


Figure 4.1 Normalized strain-life data of Inconel 718 under different axial/torsional loading paths, at room temperature and 450 °C.

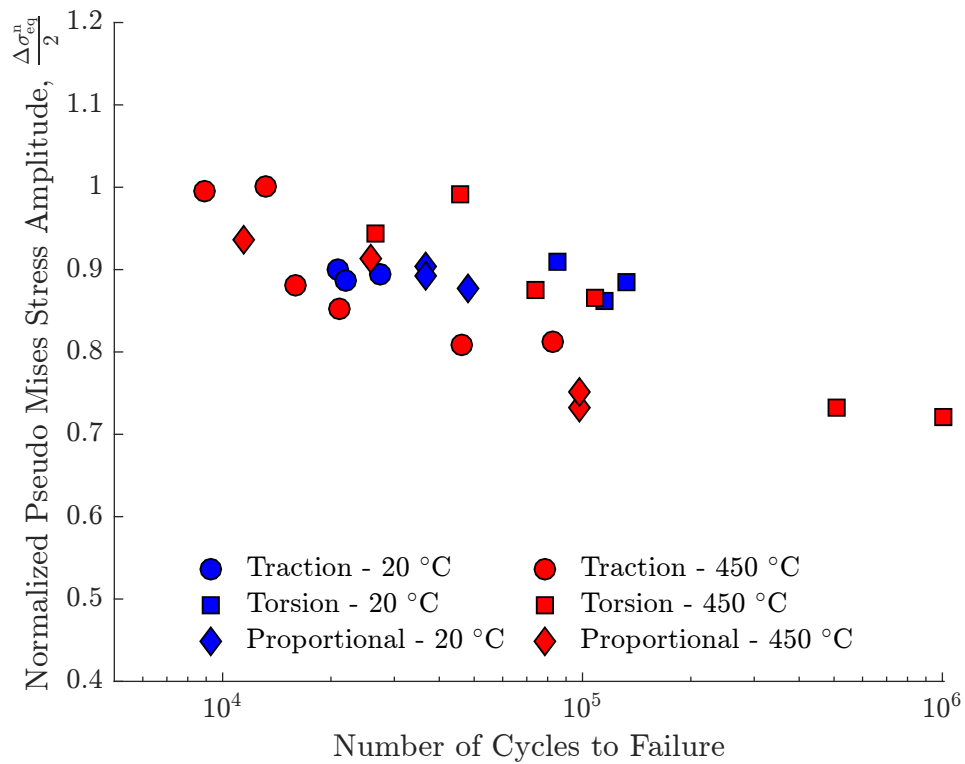


Figure 4.2 Normalized pseudo stress-life data of Inconel 718 under different axial/torsional loading paths, at room temperature and 450 °C.

Table 4.1 Inconel 718 fatigue test data.

Loading Type	Spec. ID	Control Mode	Temp. [°C]	Control parameters						Stabilized stress quantities				N_f [Cycles]
				$\Delta\varepsilon^n/2$	$\Delta\gamma^n/2$	R_ε	R_γ	f_{strain} [Hz]	f_{load} [Hz]	σ_{max}^n	σ_{min}^n	τ_{max}^n	τ_{min}^n	
Traction	4A2	Strain	20	0.78	–	0	–	0.5	–	1.00	-0.14	–	–	14,000 ^a
	7A1	Strain	20	0.78	–	0	–	0.5	–	0.99	-0.15	–	–	20,864
	5A2	Strain	20	0.78	–	0	–	0.5	–	0.99	-0.15	–	–	22,000
	3D3	Strain/Load	20	0.78	–	0	–	0.5	3.0	0.95	-0.18	–	–	27,328
	5A3	Strain	450	1.00	–	0	–	0.5	–	0.92	-0.35	–	–	8,930
	2C1	Strain/Load	450	1.00	–	0	–	0.5	3.0	0.94	-0.34	–	–	13,183
	4C1	Strain/Load	450	0.87	–	0	–	0.5	3.0	0.89	-0.24	–	–	16,007
	5C2	Strain/Load	450	0.87	–	0	–	0.5	5.0	0.88	-0.20	–	–	21,024
	6C2	Strain/Load	450	0.87	–	0	–	0.5	3.0	0.88	-0.23	–	–	38,928 ^a
	1D2	Strain	450	0.87	–	0	–	0.5	–	0.90	-0.21	–	–	44,294 ^a
	6C1	Strain	450	0.78	–	0	–	0.5	–	0.89	-0.10	–	–	20,833 ^a
	2B1	Strain/Load	450	0.78	–	0	–	0.5	5.0	0.89	-0.14	–	–	46,384
4C3	Strain/Load	450	0.78	–	0	–	0.5	0.5/3.0	0.91	-0.13	–	–	82,916	
Torsion	5C1	Strain/Load	20	–	0.78	–	0	0.5	3.0	–	–	0.99	-0.23	72,953 ^a
	4B1	Strain/Load	20	–	0.78	–	0	0.5	5.0	–	–	1.00	-0.24	84,859
	7A3	Strain	20	–	0.78	–	0	0.5	–	–	–	0.84	-0.37	85,310 ^a
	3D1	Strain/Load	20	–	0.78	–	0	0.5	3.0	–	–	0.98	-0.20	114,903
	4A1	Strain	20	–	0.78	–	0	0.5	–	–	–	0.95	-0.14	131,850

$\Delta\varepsilon^n/2$, normalized axial strain amplitude; $\Delta\gamma^n/2$, normalized shear strain amplitude; R , strain ratio; f_{strain} , testing frequency under strain control; f_{load} , testing frequency under load control; σ_{max}^n , normalized maximum axial stress; σ_{min}^n , normalized minimum axial stress; τ_{max}^n , normalized maximum shear stress; τ_{min}^n , normalized minimum shear stress; N_f , number of cycles to failure.

^a Failure at the contact point between the specimen surface and the extensometer rod tip.

Inconel 718 fatigue test data (Continuation).

Loading Type	Spec. ID	Control Mode	Temp. [°C]	Control parameters						Stabilized stress quantities				N_f [Cycles]
				$\Delta\epsilon^n/2$	$\Delta\gamma^n/2$	R_ϵ	R_γ	f_{strain} [Hz]	f_{load} [Hz]	σ_{max}^n	σ_{min}^n	τ_{max}^n	τ_{min}^n	
Torsion	3D2	Strain/Load	450	–	1.00	–	0	0.5	2.0	–	–	0.95	-0.44	26,704
	3B1	Strain/Load	450	–	1.00	–	0	0.5	1.0	–	–	0.96	-0.42	45,720
	9A1	Strain/Load	450	–	0.89	–	0	0.5	3.0	–	–	0.94	-0.28	74,195
	3C1	Strain/Load	450	–	0.89	–	0	0.5	4.0	–	–	0.92	-0.29	108,572
	1D3	Strain/Load	450	–	0.72	–	0	0.5	3.0	–	–	0.88	-0.15	253,864 ^a
	5C3	Strain/Load	450	–	0.72	–	0	0.5	0.5/3.0	–	–	0.90	-0.17	333,594 ^a
	1B1	Strain/Load	450	–	0.72	–	0	0.5	5.0	–	–	0.89	-0.11	506,906
	3C2	Strain/Load	450	–	0.72	–	0	0.5	3.0	–	–	0.89	-0.15	1,010,427
Proportional Traction-Torsion	4C2	Strain/Load	20	0.38	0.68	0	0	0.5	3.0	0.49	-0.07	0.84	-0.25	36,639
	7A2	Strain/Load	20	0.38	0.68	0	0	0.5	1.0	0.50	-0.07	0.85	-0.21	36,670
	1C1	Strain/Load	20	0.38	0.68	0	0	0.5	0.5	0.52	-0.05	0.89	-0.16	47,875
	9A2	Strain/Load	450	0.51	0.76	0	0	0.5	2.0	0.53	-0.15	0.77	-0.29	11,392
	2D2	Strain/Load	450	0.51	0.76	0	0	0.5	0.5	0.53	-0.18	0.74	-0.29	24,933 ^a
	2D1	Strain/Load	450	0.51	0.76	0	0	0.5	3.0	0.51	-0.15	0.74	-0.34	25,827
	1C2	Strain/Load	450	0.51	0.76	0	0	0.5	0.5	0.53	-0.13	0.74	-0.33	48,134 ^a
	1D1	Strain/Load	450	0.38	0.61	0	0	0.5	3.0	0.45	-0.05	0.74	-0.13	97,598
	4B3	Strain/Load	450	0.38	0.61	0	0	0.5	5.0	0.47	-0.06	0.76	-0.11	98,008
4B2	Strain/Load	450	0.38	0.61	0	0	0.5	5.0	0.46	-0.04	0.70	-0.10	130,685 ^a	

$\Delta\epsilon^n/2$, normalized axial strain amplitude; $\Delta\gamma^n/2$, normalized shear strain amplitude; R , strain ratio; f_{strain} , testing frequency under strain control; f_{load} , testing frequency under load control; σ_{max}^n , normalized maximum axial stress; σ_{min}^n , normalized minimum axial stress; τ_{max}^n , normalized maximum shear stress; τ_{min}^n , normalized minimum shear stress; N_f , number of cycles to failure.

^a Failure at the contact point between the specimen surface and the extensometer rod tip.

4.2 Cyclic stress-strain behavior

The stress-strain hysteresis loops of the traction, torsion, and proportional tests are shown in Figs. 4.3, 4.4, and 4.5. For all tested conditions, elastic shakedown was observed during the strain-controlled phase of the loading program. The transition from the elastic-plastic regime to the purely elastic behavior took one cycle in all tests. As a consequence of the initial yielding of the material, the stress-strain curve stabilized with a negative minimum stress value. Therefore, the material experienced negative stress ratios although the prescribed strain ratios were zero. It is interesting to note that all tests presented non-null values of mean stress after stabilization. This was an expected phenomenon considering the stress-strain behavior of Inconel 718, which did not present high levels of plasticity during any tested loading condition. Actually, the elastic behavior of this material during the stabilized regime inhibited any possibility of mean stress relaxation, which occurs only in the presence of plastic deformations.

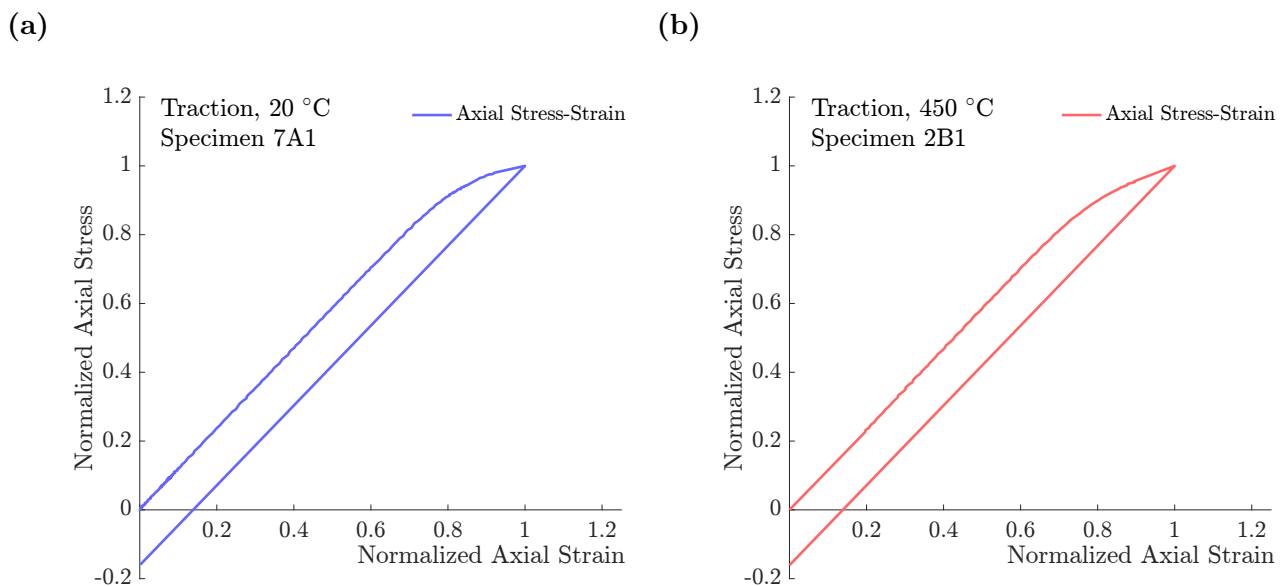


Figure 4.3 Normalized stress-strain hysteresis loops of traction tests at (a) 20 and (b) 450 °C.

The elastic moduli were determined from the stabilized stress-strain curve and decreased with increasing temperature, regardless of the applied loading condition. Table 4.2 summarizes the elastic moduli obtained for all loading types at room temperature and 450 °C. It can be seen that the mean value of the Young's modulus decreased from 205 GPa at room temperature to 184 GPa at 450 °C for traction, and from 212 to 190 GPa for proportional loading. The mean

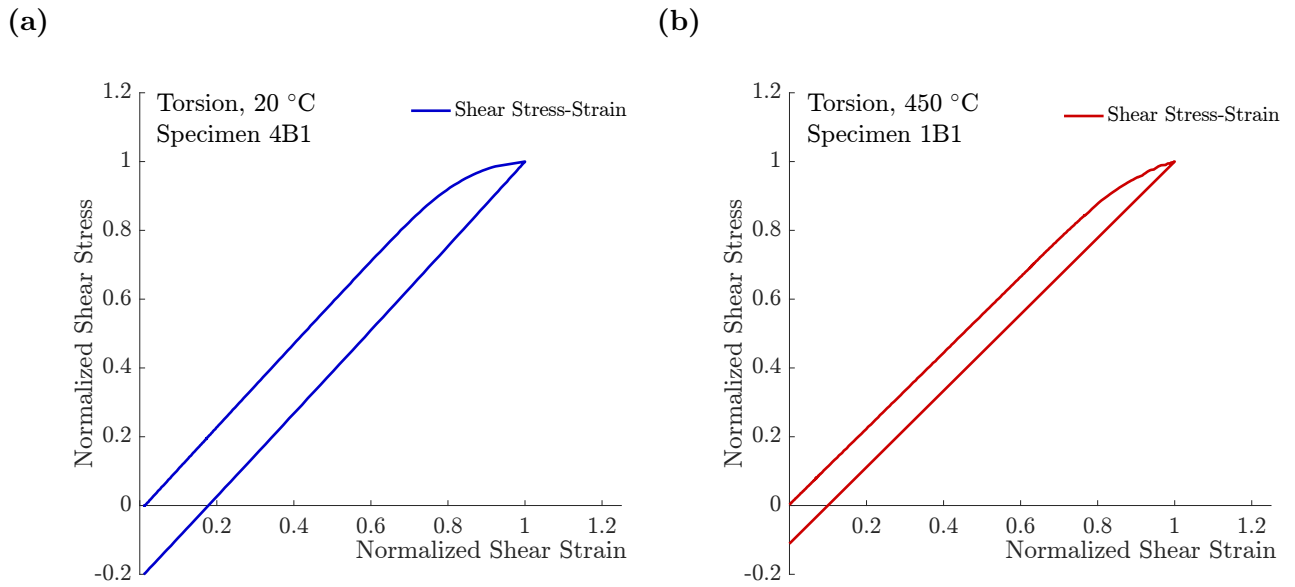


Figure 4.4 Normalized stress-strain hysteresis loops of torsion tests at (a) 20 and (b) 450 °C.

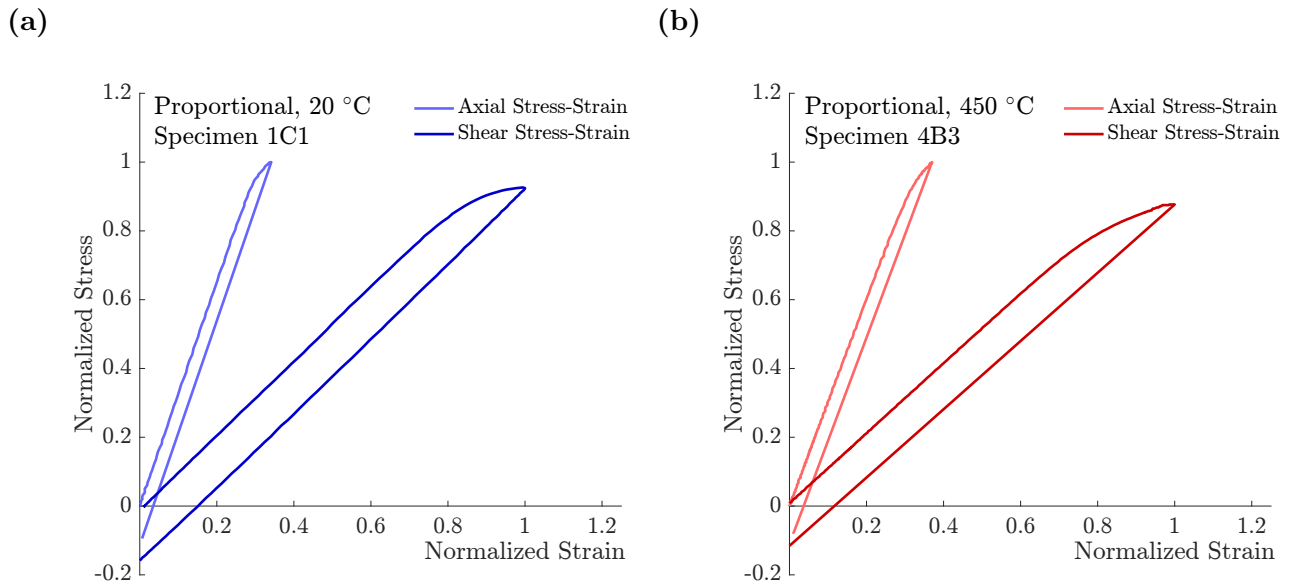


Figure 4.5 Normalized stress-strain hysteresis loops of proportional tests at (a) 20 and (b) 450 °C.

value of the shear modulus decreased from 74 GPa at room temperature to 65 GPa at 450 °C for torsion and from 73 to 64 GPa on proportional tests.

Table 4.2 Elastic moduli of Inconel 718 at room temperature and 450 °C. Units in GPa.

Loading type	Young's modulus, E		Shear modulus, G	
	20 °C	450 °C	20 °C	450 °C
Traction	205	184	–	–
Torsion	–	–	74	65
Proportional	212	190	73	64

4.3 Modeling of the constitutive behavior

The Chaboche plasticity model [25] was adopted in this study to describe the cyclic stress-strain behavior of Inconel 718. The choice for using this model was motivated by the results of previous investigations that indicated that models based on the Chaboche kinematic hardening rule can describe the behavior of Inconel 718 under a variety of loading and temperature conditions (see, e.g., Refs. [54, 55]). In this section, a brief outline of the framework used for cyclic plasticity modeling is presented. Then, the procedure to determine the material constants of the model is discussed, and finally simulated and observed stress-strain responses are compared.

Since the strain levels are small, the total strain can be decomposed into a sum of elastic and plastic components. The elastic behavior is described by the generalized Hooke's law, while the plastic strain rate is associated with a von Mises yield surface which is only allowed to translate, i.e., no isotropic hardening is considered. These conditions can be expressed mathematically as follows:

$$\boldsymbol{\varepsilon} = \boldsymbol{\varepsilon}^e + \boldsymbol{\varepsilon}^p, \quad (4.1)$$

$$\boldsymbol{\sigma} = \mathbb{C}\boldsymbol{\varepsilon}^e, \quad (4.2)$$

$$f = \sqrt{\frac{3}{2}}\|\boldsymbol{S} - \boldsymbol{\alpha}\| - \sigma_0 \leq 0, \quad (4.3)$$

$$\dot{\boldsymbol{\varepsilon}}^p = \dot{p} \frac{\partial f}{\partial \boldsymbol{\sigma}}, \quad (4.4)$$

where $\boldsymbol{\varepsilon}$, $\boldsymbol{\varepsilon}^e$ and $\boldsymbol{\varepsilon}^p$ are the total, elastic, and plastic strain tensors, respectively; $\boldsymbol{\sigma}$ and \mathbb{C} are the Cauchy stress and isotropic elasticity tensors, respectively; \boldsymbol{S} and $\boldsymbol{\alpha}$ are the deviatoric stress and backstress tensors, respectively, and σ_0 is the cyclic yield stress; \dot{p} is the equivalent plastic strain rate defined by $\dot{p} = \sqrt{2/3}\|\dot{\boldsymbol{\varepsilon}}^p\|$.

The backstress tensor $\boldsymbol{\alpha}$ associated with kinematic hardening is the center of the yield surface and is decomposed into a sum of M backstress tensors $\boldsymbol{\alpha}^i$, as proposed by Chaboche in 1979 [56]. Moreover, the evolution equation of each backstress tensor is governed by the same Armstrong–Frederick rule [57] with different material parameters. Stated mathematically,

$$\boldsymbol{\alpha} = \sum_{i=1}^M \alpha^{(i)}, \quad (4.5)$$

$$\dot{\boldsymbol{\alpha}}^{(i)} = \frac{2}{3} c^{(i)} \dot{\boldsymbol{\epsilon}}^p + \zeta^{(i)} \alpha^{(i)} \dot{p}, \quad (4.6)$$

$$\boldsymbol{\sigma} = \sum_{i=1}^M \left[\frac{c^{(i)}}{\zeta^{(i)}} \tanh(\zeta^{(i)} \boldsymbol{\epsilon}^p) \right] + \sigma_0, \quad (4.7)$$

where $c^{(i)}$, $\zeta^{(i)}$, and σ_0 are material parameters to be determined after a calibration process, fitting experimental data into Eq. (4.7), which is the analytical equation of the Chaboche cyclic plasticity model. To this end, data from traction tests at room temperature and 450 °C were used to obtain two different sets of constants for both temperatures. Due to the limited range of strain amplitudes tested, the values of stresses and plastic strains associated with the upper branch of the first loading cycle were used to perform the calibration procedure. Data from the test carried out on specimen 7A1 was used to obtain the set of room temperature constants, while data from the test conducted on specimen 2B1 generated the set of constants at 450 °C. This practice is feasible as long as the material displays Masing behavior, a phenomenon observed when the ascending parts of the hysteresis loops obtained at different maximum prescribed strains are the same. Therefore, based on data presented by Cook [9] and Sudarshan [58], it was considered that this material showed Masing behavior under these loading and temperature conditions. During the calibration procedure, it was observed that $M = 2$ accurately fitted the experimental data in the Chaboche model. Figs. 4.6 and 4.7 show experimental and simulated fatigue data from traction tests at room temperature and 450 °C during and after stabilization, showing that the model captures the initial plasticity and the subsequent elastic shakedown in both temperatures. The constants obtained for the Chaboche model are presented in Table 4.3.

Table 4.3 Constants of the Chaboche model for Inconel 718 at room temperature and 450 °C.

Temperature [°C]	$c^{(1)}$ [MPa]	$c^{(2)}$ [MPa]	$\zeta^{(1)}$	$\zeta^{(2)}$	σ_0 [MPa]
20	2.11×10^5	3.79×10^4	2219	1213	1121
450	4.39×10^4	8.63×10^5	508	7415	974

After the calibration procedure, the Chaboche model was computationally implemented using

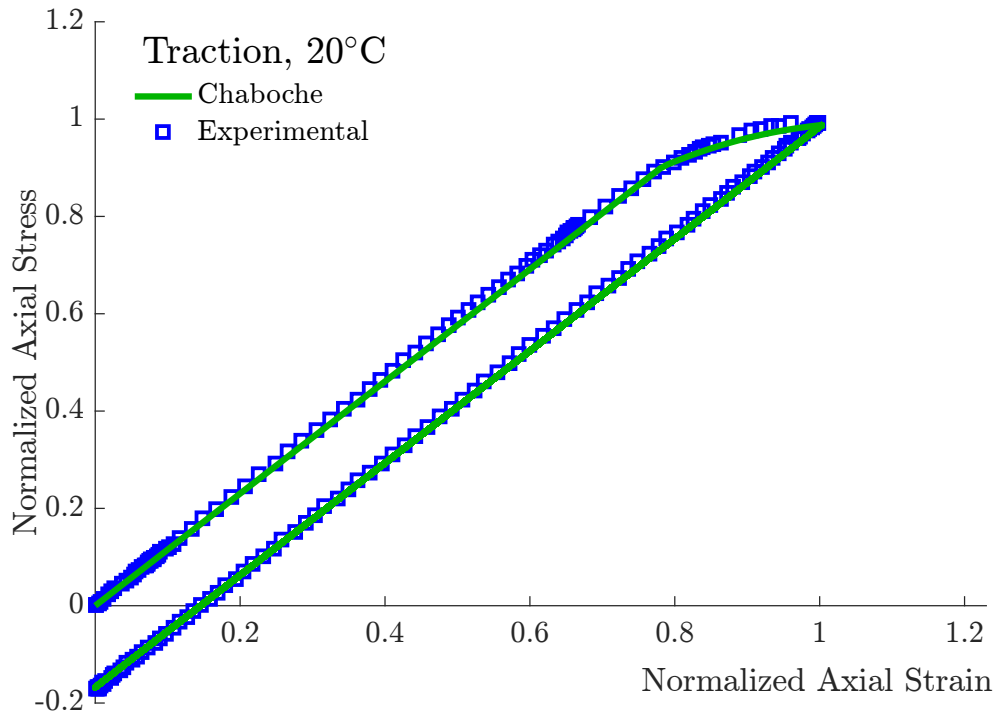


Figure 4.6 Normalized experimental data used to determine the Chaboche parameters at room temperature. Data was taken from a traction test carried out on specimen 7A1.

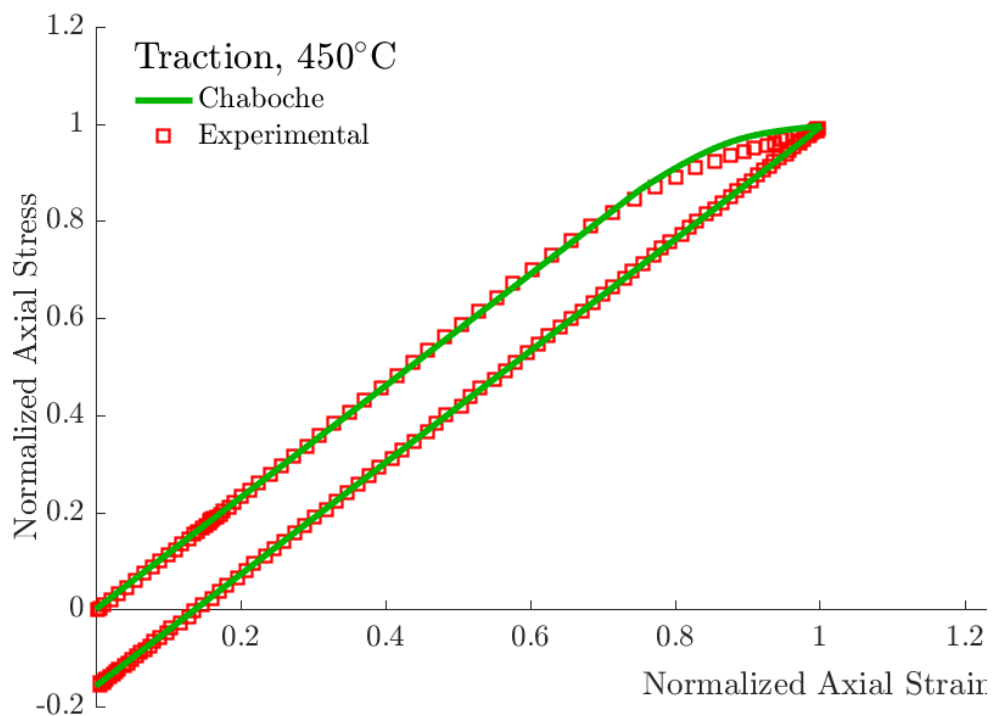


Figure 4.7 Normalized experimental data used to determine the Chaboche parameters at 450 °C. Data was taken from a traction test carried out on specimen 2B1.

a Matlab script to determine the stress-life response of all loading and temperature conditions tested. The results of the simulations are presented in Figs. 4.8, 4.9, and 4.10, which show the mean and amplitude components of the equivalent von Mises stress, defined as $\sigma_{eq} = \sqrt{\sigma^2 + 3\tau^2}$. For comparison purposes, the mean and amplitude components of the experimental stresses were also plotted, enabling an assessment of the calibration quality. As seen in Fig. 4.8, the stress-life behavior of the traction tests was precisely simulated for both temperatures, an expected result since the model was calibrated under these conditions. At room temperature, the simulated torsion behavior resulted in a deviation from the experimental data of 5% for the mean and amplitude components of the equivalent stress, while at 450 °C, this deviation was 5 and 0.5%, respectively. For the cases under proportional loading at room temperature, the deviations for the mean and amplitude components of the equivalent stress were 2 and 7%, respectively, while at 450 °C, these differences were 2 and 6%, respectively. The simulations lasted the same number of cycles observed on the strain-controlled phase of each test, noting that among the tests presented, the only one carried out to failure was the room temperature traction test, performed on specimen 7A1. The other tests changed the control mode a few cycles after stabilization. Observing the minimal percentage differences between the simulated and experimental equivalent stresses, it is possible to conclude that the Chaboche model successfully simulated the stress-life behavior of Inconel 718 under all imposed conditions.

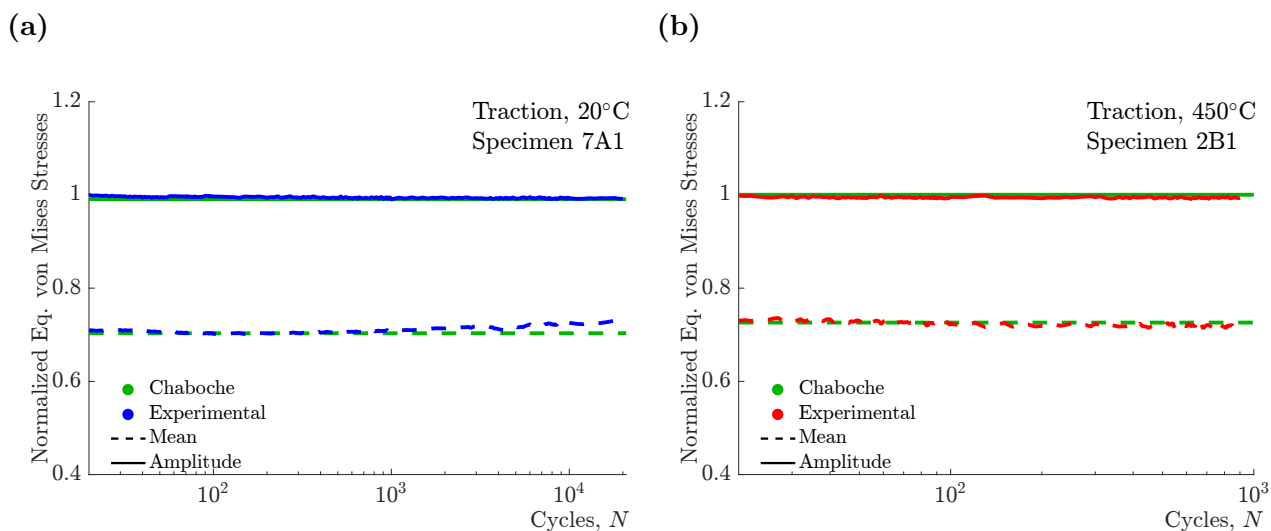


Figure 4.8 Simulated and experimental von Mises stress components from traction tests at (a) room temperature and (b) 450 °C. Stress values were normalized.

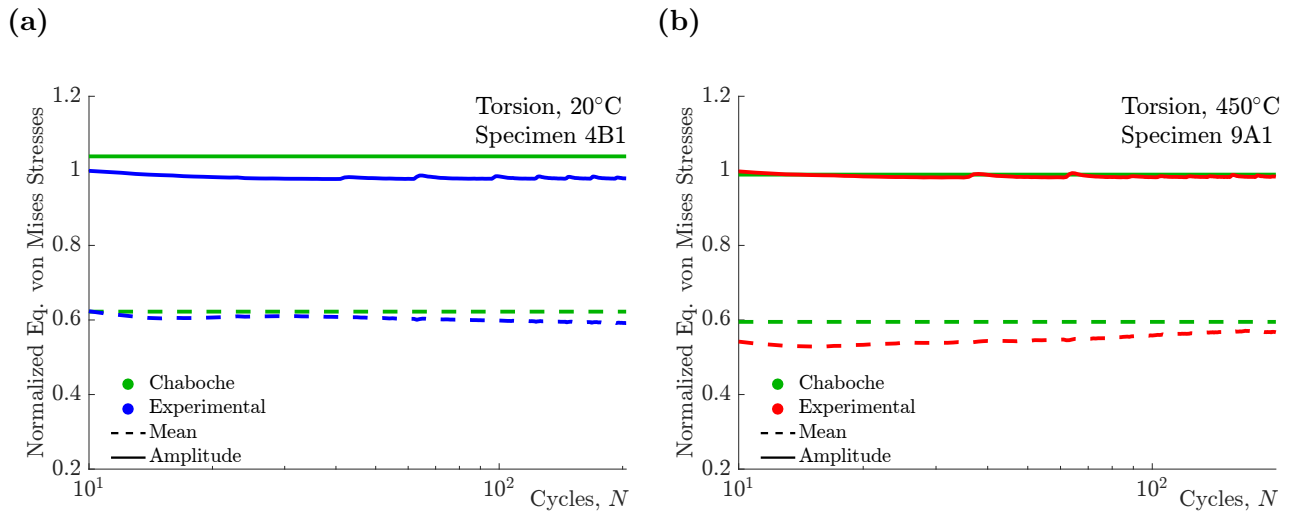


Figure 4.9 Simulated and experimental von Mises stress components from torsion tests at (a) room temperature and (b) 450 °C. Stress values were normalized.

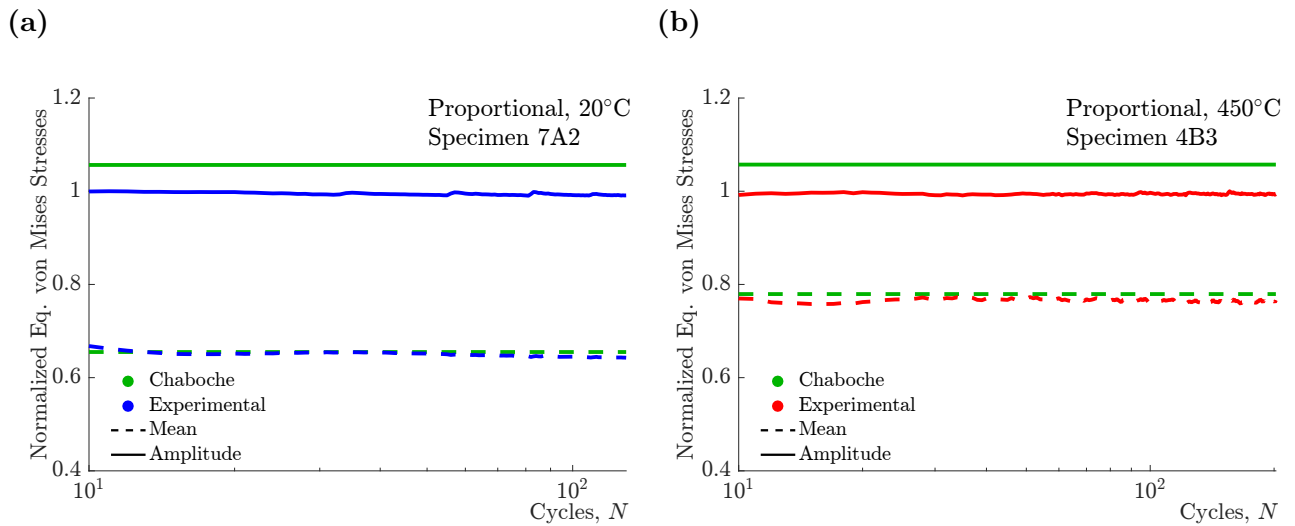


Figure 4.10 Simulated and experimental von Mises stress components from proportional tests at (a) room temperature and (b) 450 °C. Stress values were normalized.

4.4 Observation of macroscopic fatigue cracks

The orientation of a macroscopic crack is essential to understand the failure mechanism of a material under cyclic loading. Extensive experimental observations performed over the last decades have indicated that three types of cracking behavior can be distinguished [59]. Shear cracking behavior occurs when the fatigue crack is observed on the material plane of maximum shear stress/strain amplitude, and tensile cracking behavior when cracks are initiated on the plane of maximum normal stress/strain amplitude. A material may also exhibit mixed

cracking behavior, which is characterized by crack initiation on the maximum normal planes for tension-compression loading but on the maximum shear plane under pure shear loading. Once the basic failure mechanism of a material is known, the selection of a proper fatigue damage criterion can be carried out [27, 60].

In this study, a macroscopic crack was observed on the surface specimen after the interruption of each fatigue test. Subsequently, the crack angles were measured so as to assess the influence of the loading path and temperature on the cracking behavior. Fig. 4.11a shows the coordinate system adopted to measure the angles of the material plane where a crack was formed, the so-called critical plane, while the angles that define a material plane are indicated in Fig. 4.11b. The angle ϕ gives the inclination of the material plane with respect to the specimen surface, while the angle θ indicates the orientation of the plane-surface intersection. Examples of crack growth in critical planes perpendicular to the specimen surface (i.e. with $\phi = 90^\circ$) are illustrated in Fig. 4.11c.

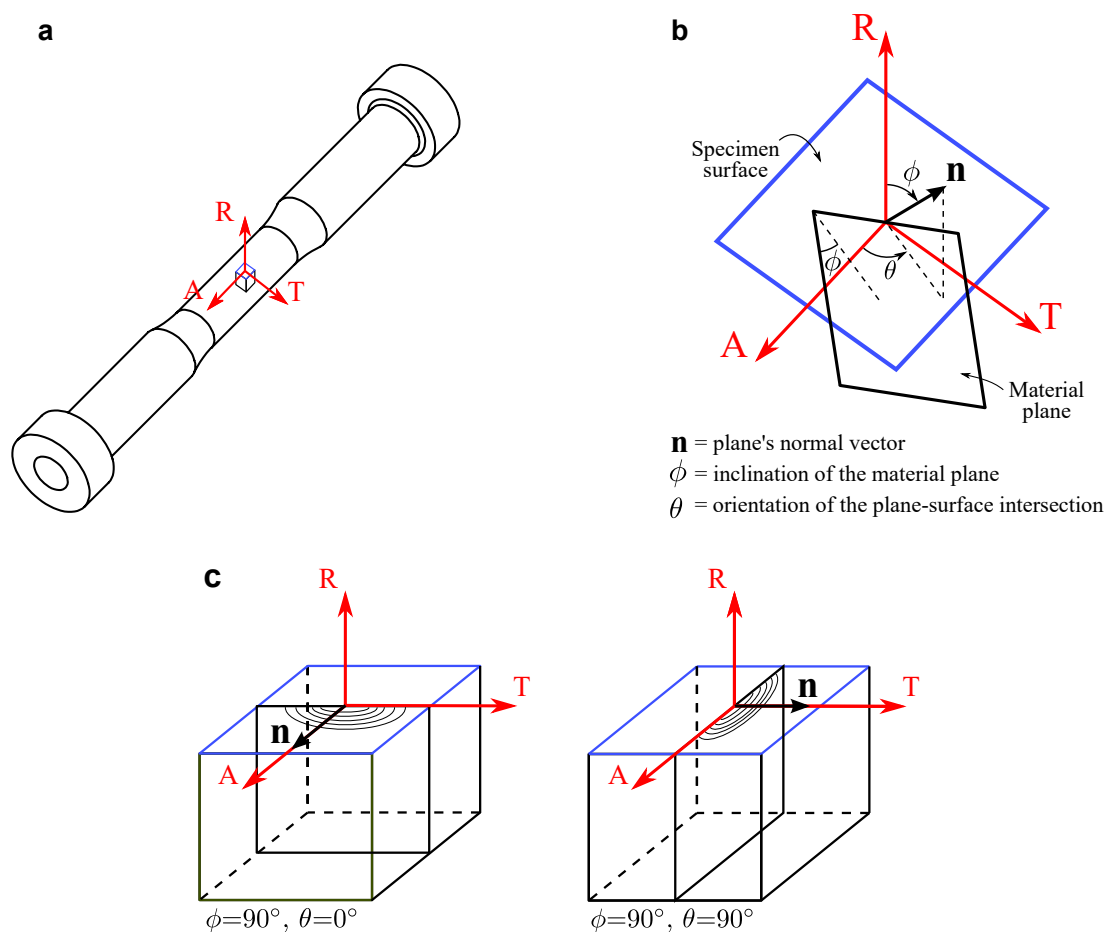


Figure 4.11 (a) Coordinate system attached to a representative volume of material of the thin-walled tubular specimen, (b) definition of the angles ϕ and θ , (c) examples of critical planes perpendicular to the surface.

The θ angle was determined from the surface cracks shown in Figures 4.12, 4.13, 4.14, and 4.15, while the ϕ angle was measured after the final failure of the cracked specimen. SEM analyses later confirmed the values obtained for both angles, considering the exact crack initiation site. Table 4.4 summarizes the crack orientation directions of all kinds of tests performed. According to the angles measured, the traction tests presented tensile cracks ($\phi = 90^\circ$ and $\theta = 0^\circ$), while shear cracks were visualized in the torsion and proportional tests ($\phi = 90^\circ$ and $\theta = 0^\circ$ or $\theta = 90^\circ$). This result indicates that this material presented mixed cracking behavior under the testing conditions considered. On the other hand, Socie [17] observed that the failure mode of Inconel 718 is the nucleation and growth of mode II shear cracks for axial, torsional, and proportional axial-torsional loading. However, under a macroscopic view, only the directions of the last two loading paths agreed with the conclusion proposed by Socie. Filippini et al. [23] pointed out that this material's early life is controlled by cracks that grow on planes perpendicular to the maximum principal stress and strain. This observation is consistent with the crack direction of the traction tests, considering the strain levels applied. Up to 450 °C, the temperature does not seem to influence the crack direction, as these were the same for both temperatures of the same strain path.

Table 4.4 Critical plane angles.

Loading type	Spec. ID	Temp. [°C]	ϕ [°]	θ [°]
Traction	7A1	20	90	0
	2B1	450	90	0
Torsion	3D1	20	90	90
	9A1	450	90	90
Proportional	4C2	20	90	90
	4B3	450	90	90

4.5 Fracture surface examination

The failure surface analysis of specimens submitted to all studied loading conditions was performed in a JEOL JSM-7100F Scanning Electron Microscope (SEM). The purpose of this investigation was to determine the initiation site of the crack that led to failure and its propagation mechanism, assessing the consequences of the temperature effect on each loading type tested. The fractography revealed that all cracks initiated at inclusions located at the external surface

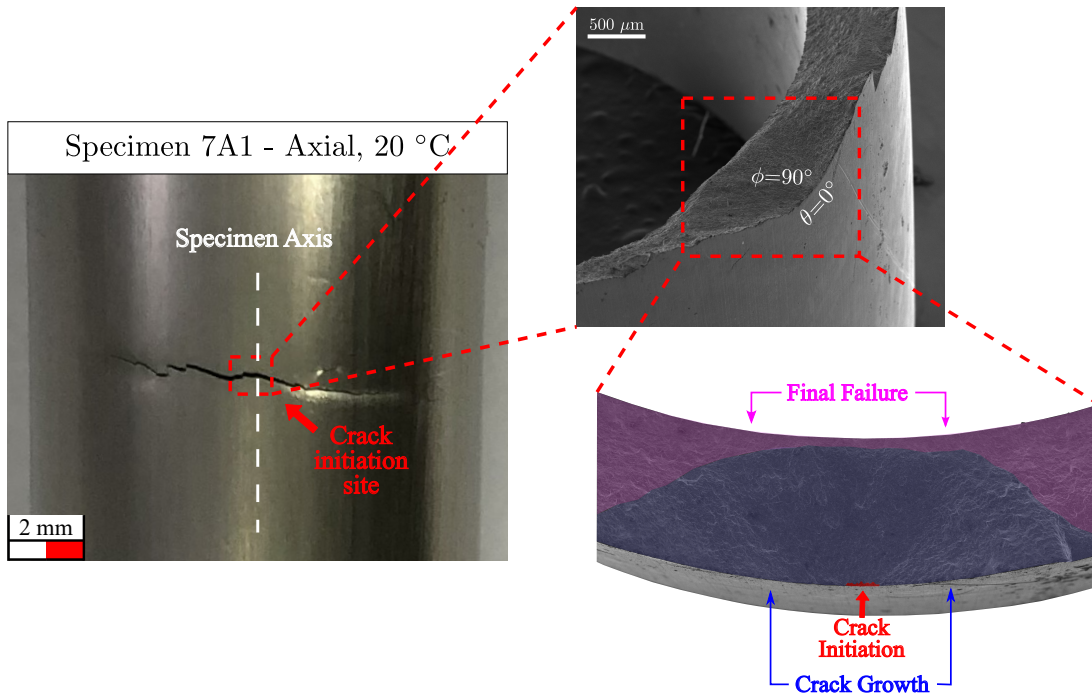


Figure 4.12 Macroscopic crack of a traction test conducted at room temperature on specimen 7A1. In detail, the angles observed in the crack propagation region, defined by the blue color.

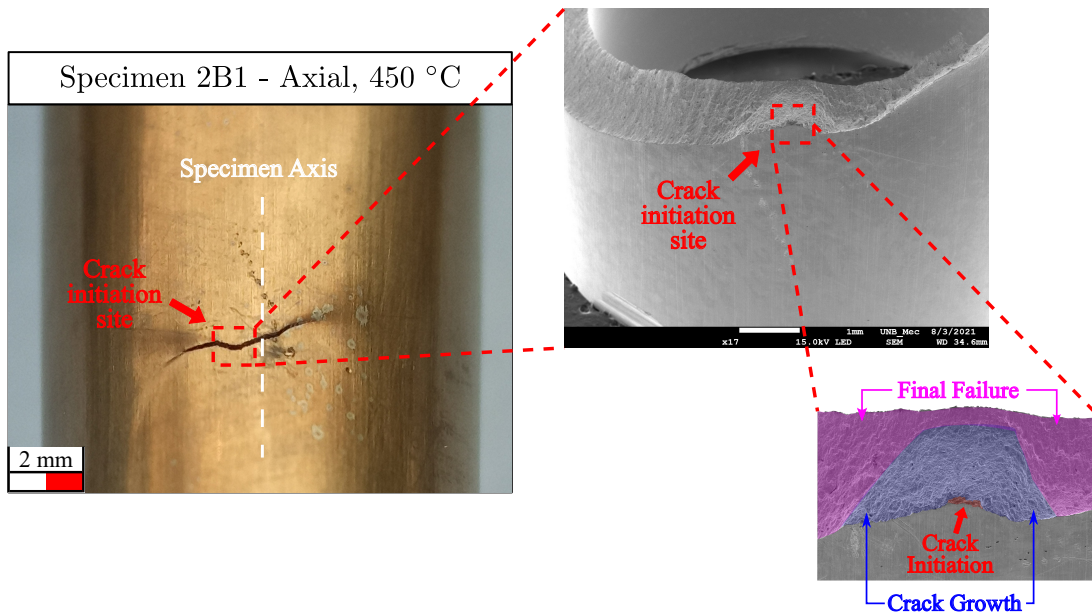


Figure 4.13 Macroscopic crack of a traction test conducted at 450 °C on specimen 2B1. In detail, the crack initiation, propagation, and final failure regions are defined by the colors red, blue, and pink, respectively.

or sub-surface of the specimen, regardless of the type of applied loading or temperature. Energy Dispersive Spectrometry (EDS) analysis carried out with a JEOL EX-230**BU EX-37001 showed that most of these particles were titanium and niobium-rich MC-type carbides, commonly found in the nickel matrix of a direct aged Inconel 718 [61]. These carbides can be both beneficial and

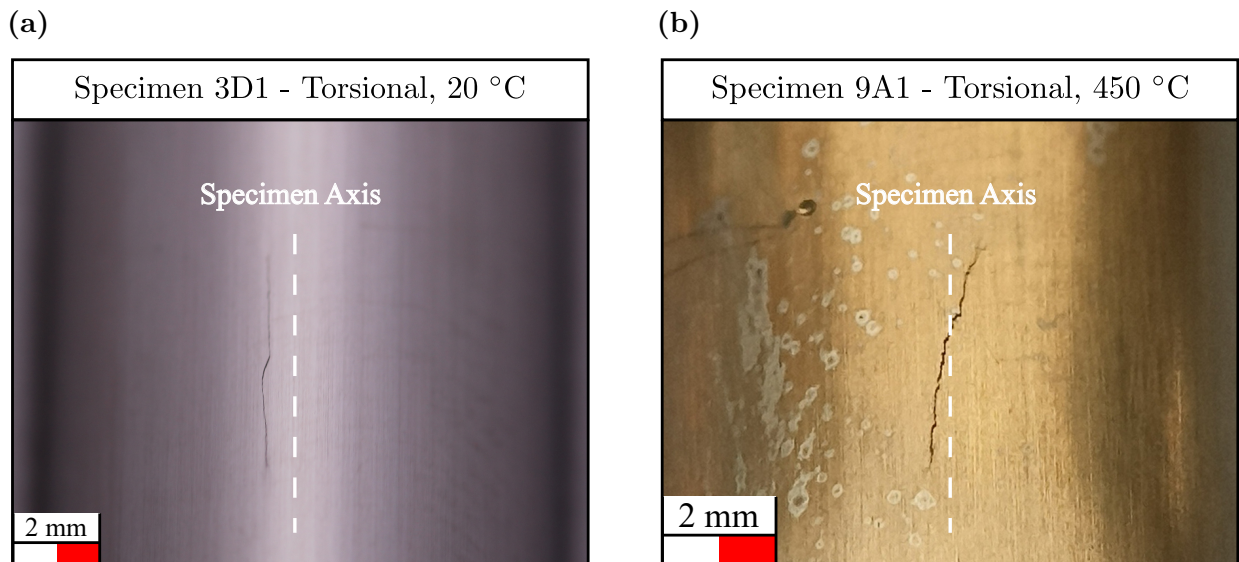


Figure 4.14 Macroscopic cracks of torsion tests at (a) room temperature and (b) 450 °C.

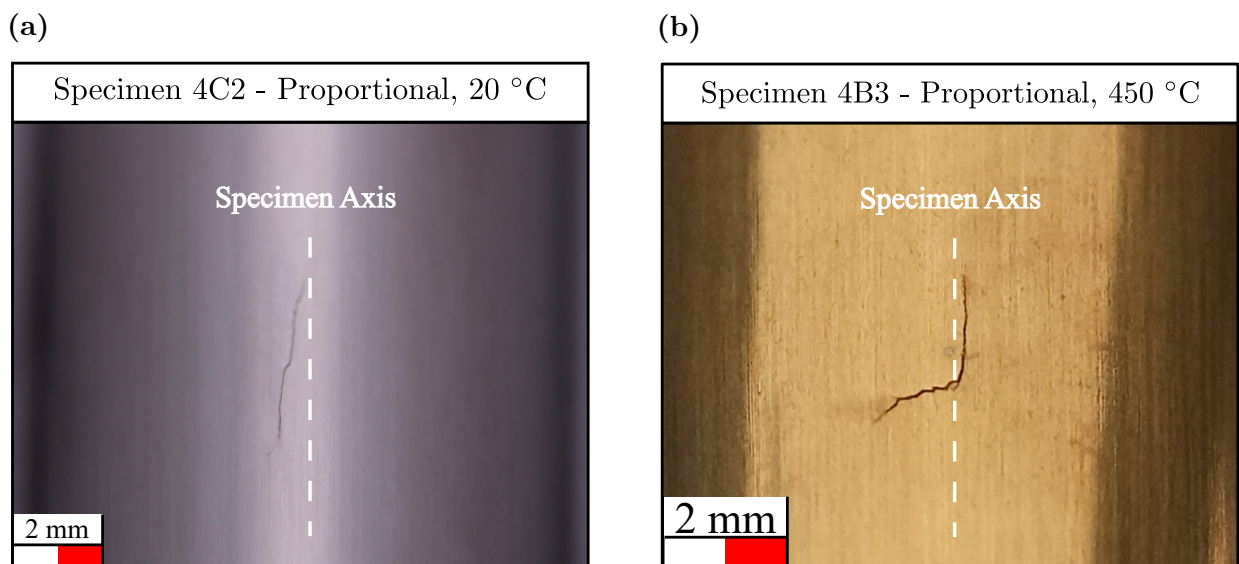


Figure 4.15 Macroscopic cracks of proportional traction-torsion tests at (a) room temperature and (b) 450 °C.

detrimental to the mechanical properties, depending on their size, distribution, and location in relation to the grains. When located on the surface of a component, they can be pre-cracked and oxidized if subjected to thermal stresses, generating a stress concentrator unfavorable to the fatigue properties [30]. Fig. 4.16 provides the titanium-rich carbide located on the outer surface of specimen 2B1, responsible for initiating the crack that led to the final failure of the high-temperature traction test. An EDS in the lower corner of the image confirms that this inclusion is primarily made of titanium.

The crack growth mechanism was also determined for each loading path in both temperatures

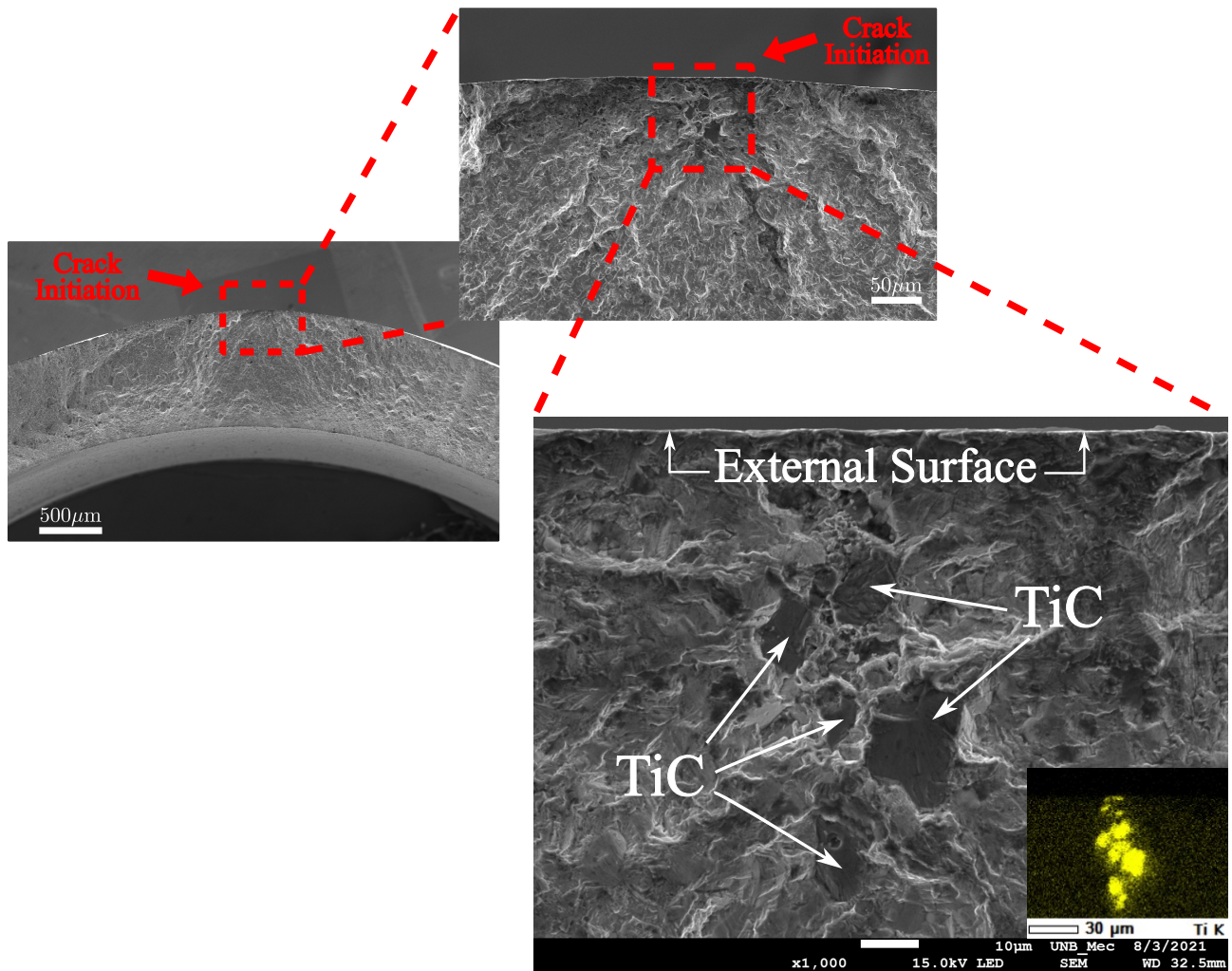


Figure 4.16 Ti-rich metal carbide at the crack initiation locus of specimen 2B1, used in a high-temperature traction test. An EDX image in the lower-left corner shows the titanium distribution in the figure.

via a failure surface morphology evaluation. First, it is important to characterize how cracks form and develop into the material surface, a process that takes place in two stages: In stage I, the crack starts on the surface of a grain and grows to another, subtly changing its direction due to the random orientations of the grains in the matrix; Stage II is observed when the crack is large enough to generate its plasticity, growing flat through the grains [62]. However, for all tested conditions on this material, cracks initiated at inclusions that were larger than the grains. As a consequence, the fatigue life was spent in stage II propagation from a crack whose initial size was equal to the length of an inclusion particle. This result is consistent with what Pineau et al. [63] observed in traction tests under similar testing conditions.

Planar areas with a strong crystallographic aspect were noted next to the inclusions responsible for initiate failure cracks, as illustrated in Fig. 4.17. These facets structures indicate the

transgranular propagation mode as the predominant mechanism of the three studied loading paths, regardless of the test temperature. Pineau and Clavel [64] had already observed this result, also only for axial cases. This conclusion is ratified by striation marks observed on the fracture surface of specimens submitted to all loading types, each with its particularities. In traction loading, the striations were well defined and perpendicular to the direction of crack growth, as seen in Fig. 4.18. Under torsion, striations were slightly erased due to contact between the crack surfaces during shear loading, but its direction remains perpendicular to the crack growth orientation, as shown in Fig. 4.19. For the case of proportional loading, striations were not as deformed as in torsion, and their direction undergoes great variability, not always being orthogonal to the crack growth direction, as presented in Fig. 4.20.

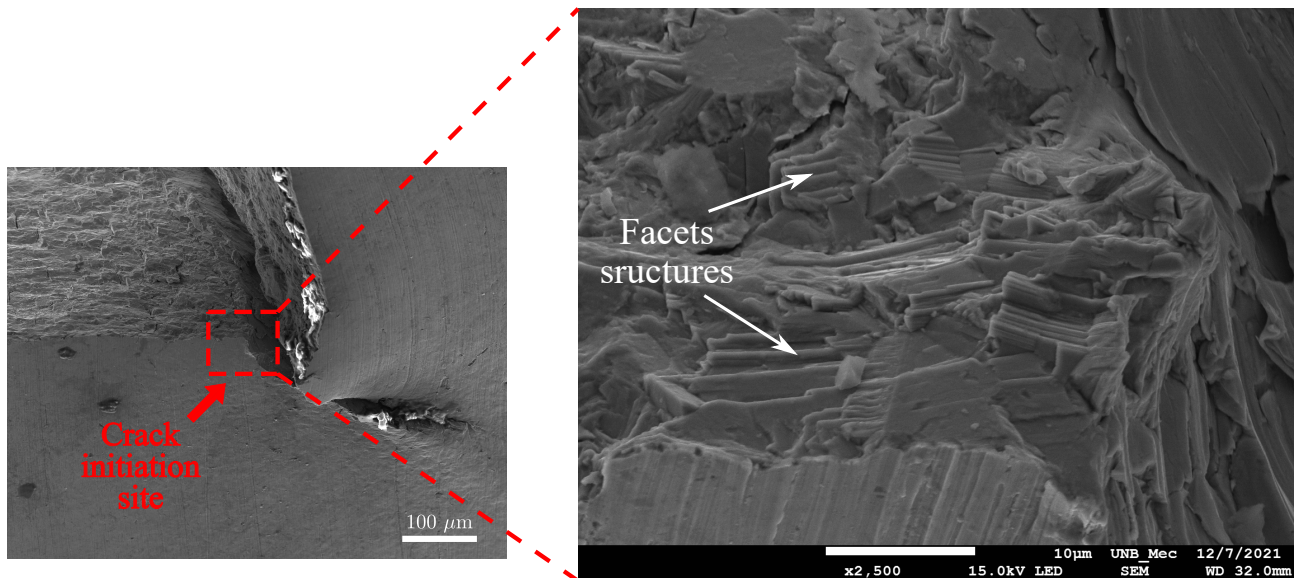


Figure 4.17 Scanning electron micrograph of facets structures near the failure initiation locus, indicating the transgranular propagation mode as the main crack growth mechanism from a room temperature torsion test performed on specimen 4B1.

It is important to highlight that some elements of intergranular fracture were occasionally identified close to the crack initiation site in the proportional tests, as illustrated in Fig. 4.21. Characterized by the presence of three-dimensional grain structures and proceeding along larger grain boundaries, this mechanism was more evident in the high-temperature tests, even not being the dominant propagation mode. Dimples were visualized in all cases in the final fracture region. Fig. 4.22 shows the moment of transition from the propagation phase to final failure, where widely spaced striations indicate the high growth rate of the crack while dimples characterize the final failure.

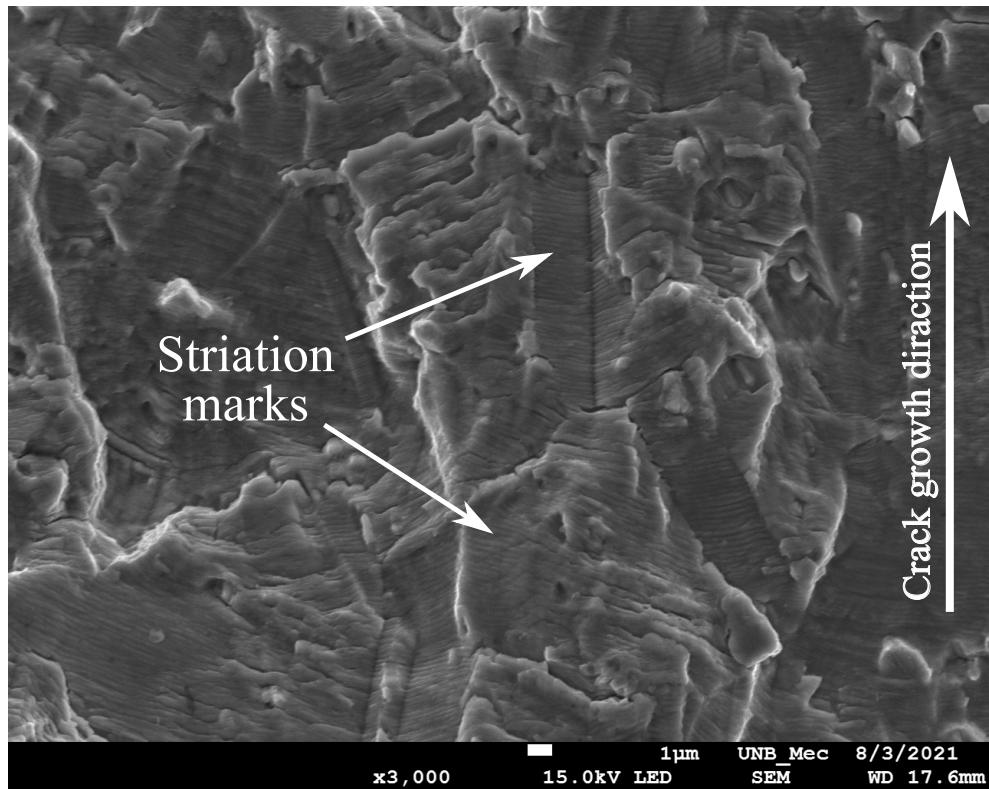


Figure 4.18 Striation marks were observed in a high-temperature traction test conducted on specimen 2B1.

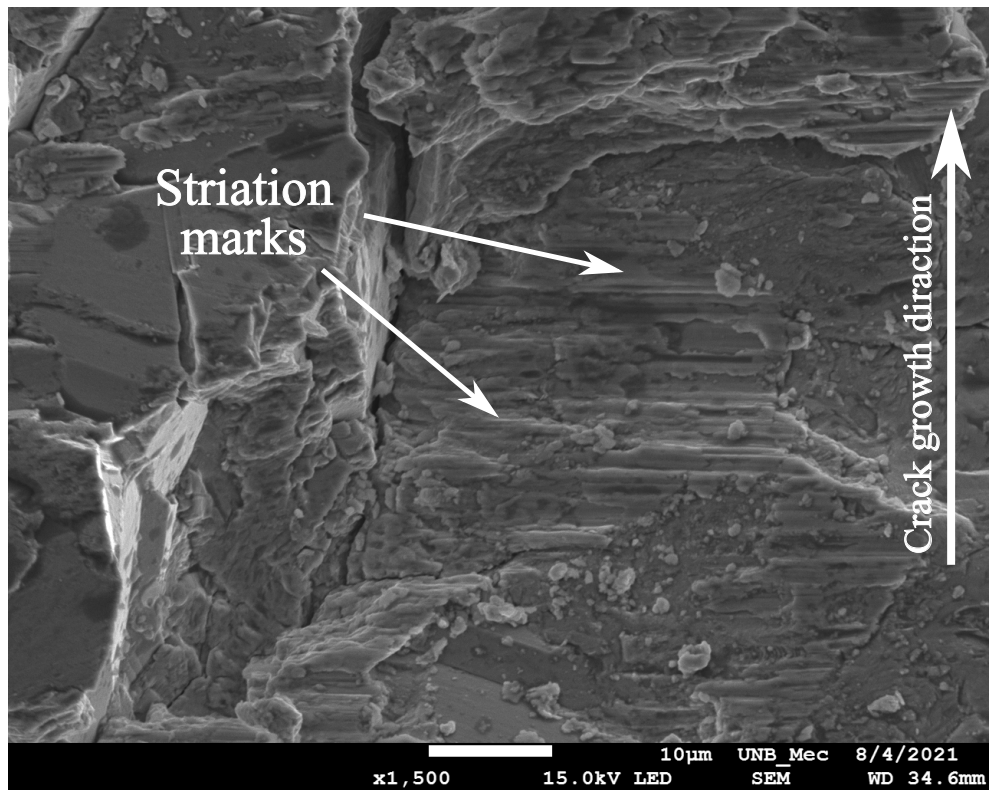


Figure 4.19 Striation marks were observed in a high-temperature torsion test conducted on specimen 9A1.

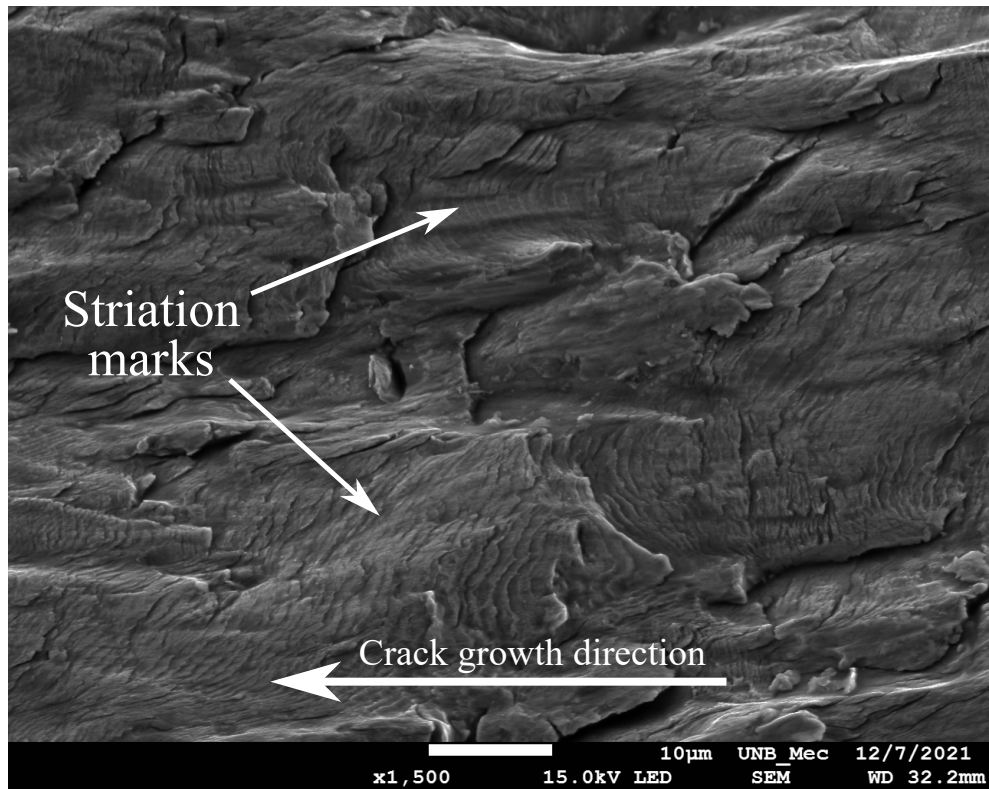


Figure 4.20 Striation marks were observed in a room temperature proportional traction-torsion test conducted on specimen 7A2.

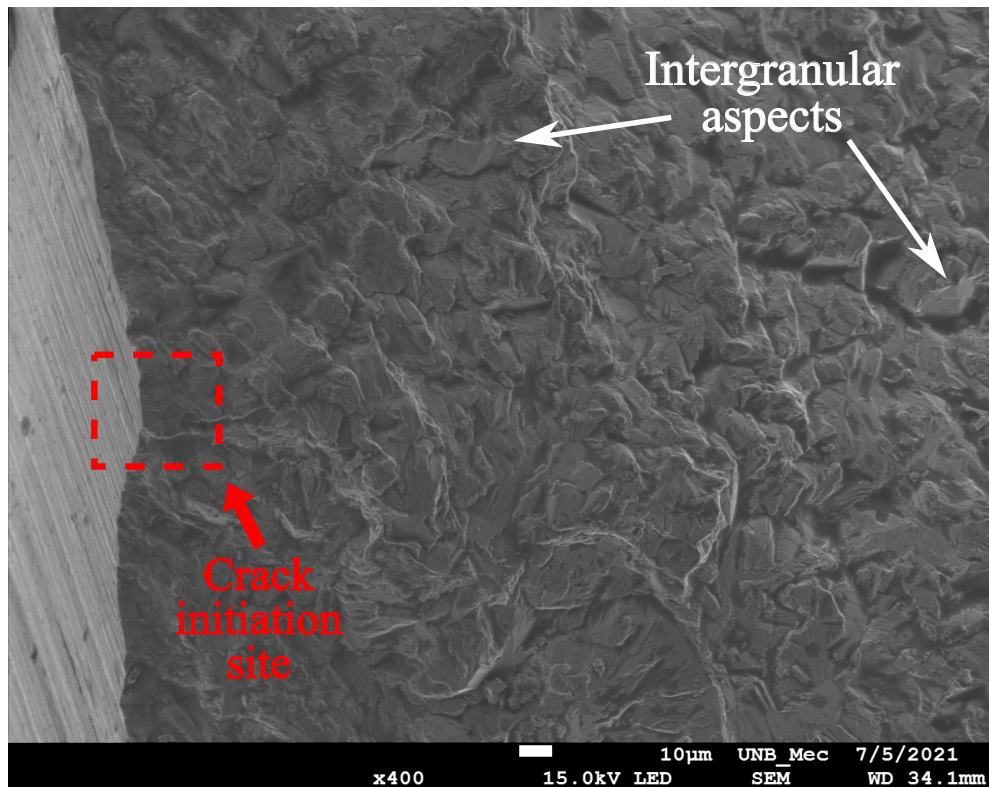


Figure 4.21 Intergranular propagation aspects of a high-temperature proportional traction-torsion test performed on specimen 4B3.

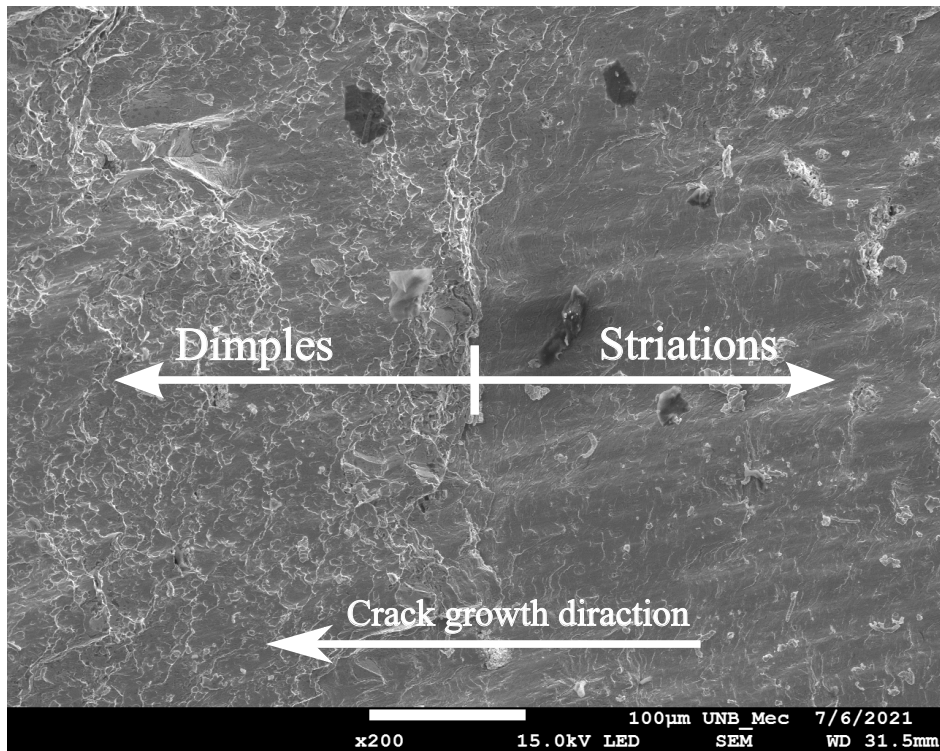


Figure 4.22 The transition from crack propagation to final failure of a high-temperature proportional test performed on specimen 4B3.

4.6 Evaluation of critical plane fatigue criteria

The fatigue life of Inconel 718 was estimated from fatigue criteria based on the critical plane approach. Such an approach admits that the fatigue cracking occurs on specific planes, which are sensitive to the material, stress state, and loading magnitude involved. The orientation of the cracks that cause fatigue failure is determined by the planes in which the fatigue damage accumulation reaches a limit. Therefore, the choice of the fatigue parameter should be consistent with the failure mechanism of the material under analysis [27, 59], highlighting that, in 1984, Socie [17] concluded that Inconel 718 exhibits mode II shear cracks in tension and torsion loading at room temperature. This observation suggests that the fatigue life prediction model proposed by Fatemi and Socie [19] (FS) should be employed since the physics of its failure mechanism is based on shear cracks. As observed in Section 4.4, Socie’s conclusion is consistent with results obtained in torsion and proportional tests at both temperatures tested. However, the traction tests failed with mode I cracks for the load and temperature conditions employed, suggesting the use of the multiaxial version of the Smith, Watson, and Topper (SWT) parameter [26], proposed by Socie [27].

Fatemi–Socie

Starting from the model developed by Brown and Miller [45], Fatemi and Socie proposed in 1988 [19] a fatigue parameter based on the critical plane approach that considered that fatigue cracks initiate and grow on planes where the shear strain amplitude reaches the maximum values. Among these planes, the critical plane that results in final failure will be the one where the maximum normal stress is observed. Mathematically, this model accounts for these considerations relating the maximum normal stress σ_{nmax} with the maximum shear strain amplitude $\Delta\gamma_{\text{max}}/2$, contained in the maximum shear plane, as shown in Eq. (4.8).

$$\text{FS} = \frac{\Delta\gamma_{\text{max}}}{2} \left(1 + k \frac{\sigma_{\text{nmax}}}{\sigma_y} \right) = f(N_f), \quad (4.8)$$

where σ_y is the yield strength, and $f(N_f)$ is a function of the fatigue life. The material constant k can be computed from axial and torsional data and was assumed to be a constant throughout the fatigue life in this work.

Smith–Watson–Topper

In 1970, Smith, Watson, and Topper [26] proposed a fatigue parameter applicable to uniaxial loading conditions with any stress ratio, thus including situations with non-zero mean stresses. The authors considered that the normal strain amplitude $\Delta\varepsilon_n/2$ and the maximum normal stress σ_{nmax} governed the fatigue crack initiation and propagation of various metals. Later, based on the critical plane approach, Socie [27] proposed the multiaxial version of this model, advising that it should be applied to materials that fail primarily due to mode I tensile cracking. The SWT parameter is described by the following expression:

$$\text{SWT} = \sigma_{\text{nmax}} \frac{\Delta\varepsilon_n}{2} = g(N_f), \quad (4.9)$$

where $g(N_f)$ is a function of the fatigue life. The critical plane will be the material plane where the product between the maximum normal stress and normal strain amplitude is maximum.

4.6.1 Determination of material constants

The function used to correlate the FS fatigue parameter with life was the Coffin-Manson strain-life relation, described by the right-hand side of the equation bellow,

$$\frac{\Delta\gamma_{\max}}{2} \left(1 + k \frac{\sigma_{\text{nmax}}}{\sigma_y} \right) = \frac{A}{G} (2N_f)^B + C (2N_f)^D, \quad (4.10)$$

where G is the shear modulus, $2N_f$ is the number of reversals to failure, and A , B , C , D are material constants to be determined after fitting the experimental data in Eq. (4.10). Pure traction and torsion fatigue data were used to calibrate these constants and the material parameter k of the F-S model. The calibration process proceeded as follows: sets of constants of the Coffin-Manson relation were adjusted with different values of k , that ranged from 0 to 2, and used to make fatigue life predictions; the set of constants that minimizes the logarithmic difference between estimated and experimental fatigue lives were defined as the calibration constants. This procedure was carried out for both temperatures tested in this work in a way that two sets of constants were determined for Inconel 718, at 20 and 450 °C, calibrated with fatigue data related to the corresponding temperature. Table 4.5 shows the FS model constants obtained in each temperature, highlighting the values of $k_{20} = 1.5$ and $k_{450} = 0.9$ at room and high-temperature conditions, respectively.

Table 4.5 Material constants of the Fatemi–Socie strain-life relation (Eq. 4.10) obtained after the calibration process that used pure traction and torsion fatigue data at room temperature and 450 °C.

Symbol	Unit	Temperature	
		20 °C	450 °C
k	–	1.5	0.9
A	MPa	3685	2125
B	–	-0.16	-0.13
C	–	0.001	0.000
D	–	-3.01	-1.43

Using the fitted constants, Eq. (4.10) was plotted for a determined range of fatigue life and compared with traction and torsion experimental data used during the calibration, as shown in Figs. 4.23 and 4.24. In both temperatures, it was observed that all data were within a factor of 2, represented by the dashed lines, indicating that the calibrated constants successfully captured the fatigue life behavior of every point used in the fitting process. Despite the non-linearity seen in the Coffin–Manson relation, it is interesting to note that the curves obtained are almost linear. Looking closely, this result is justified by the second term of the right-hand side of Eq.

(4.10), which is negligible. Observing that this term is associated with plastic deformations, the linearity of the curves turns consistent considering the elastic behavior seen in the stabilized stress-strain regime at the two temperatures tested. As a result, a straight line is observed when looking at a logarithmic scale.

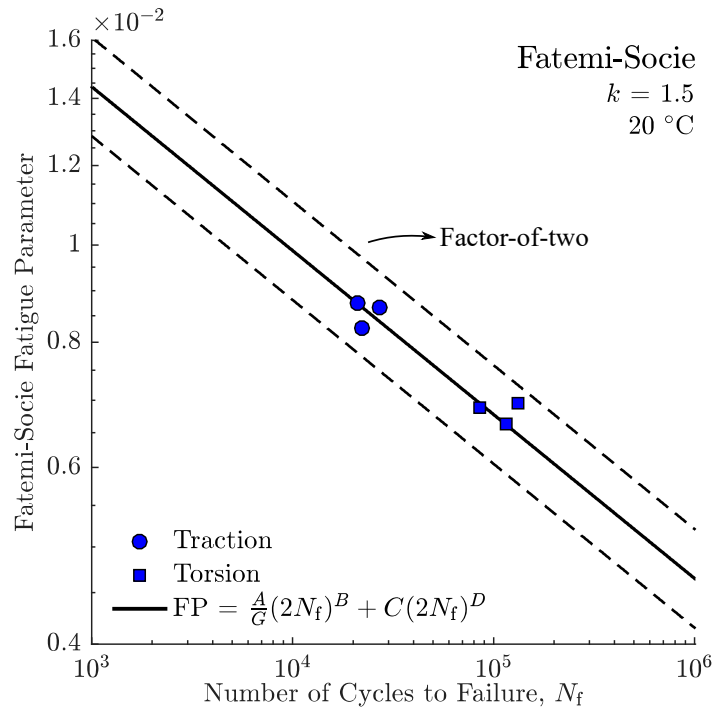


Figure 4.23 Calibration of Fatemi–Socie model using room temperature fatigue data.

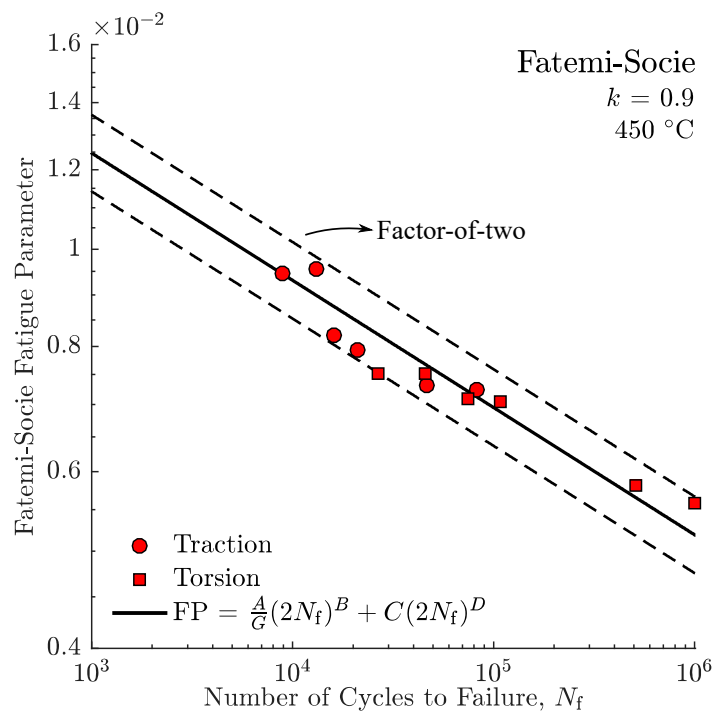


Figure 4.24 Calibration of Fatemi–Socie model using high-temperature fatigue data.

The SWT fatigue parameter was correlated with life using a strain-life relation generated from tensile testing, described by the right-hand side of the following equation,

$$\sigma_{\text{max}} \frac{\Delta \varepsilon_n}{2} = \frac{a^2}{E} (2N_f)^{2b} + ac(2N_f)^{b+d}, \quad (4.11)$$

where E is the Young's modulus, $2N_f$ is the number of reversals to failure, and a, b, c, d are material constants determined after fitting experimental data in Eq. (4.11). Pure traction and torsion fatigue data were also used to calibrate the constants of the SWT model. Therefore, the same data was used to calibrate both fatigue models considered, enabling a fairer comparison in assessing which one best predicts the fatigue life of Inconel 718. The constants of the SWT model were also obtained at room temperature and 450 °C and are shown in Table 4.6.

Table 4.6 Material constants of the Smith–Watson–Topper strain-life relation (Eq. 4.11) obtained from traction and torsion fatigue data at room temperature and 450 °C.

Symbol	Unit	Temperature	
		20 °C	450 °C
a	MPa	1059	1078
b	–	-1.46	-0.99
c	–	0.459	0.094
d	–	1.01	0.68

Proceeding as done after calibrating the FS model, the fitted constants of the SWT model were used to plot Eq. (4.11) over the range of 10^3 to 10^6 cycles. Fig. 4.25 shows the SWT model calibrated with room temperature constants, while Fig. 4.26 presents the curve obtained using the 450 °C constants. Aiming to assess the quality of the SWT model calibrated constants, the experimental data used during the calibration process was also plotted for comparison purposes. The room temperature constants successfully correlated the experimental data, which were all within a factor of 2, represented by the dashed lines. On the other hand, high-temperature constants did not have the same effectiveness, resulting in fatigue data outside the factor of 2. Once again, linear curves were obtained despite the non-linearity of Eq. (4.11). In this case, the first term of the right-hand side of this equation is the responsible, being negligible along all the fatigue life under analysis. Physically, the understanding of this phenomenon is not as intuitive as that observed in the FS model strain-life relation. The high degree of non-linearity seen in the formulation of the STW parameter makes the physics behind its terms very abstract.

In addition, it should be noted that the linearity of the curves is independent of the temperature at which the model constants were determined.

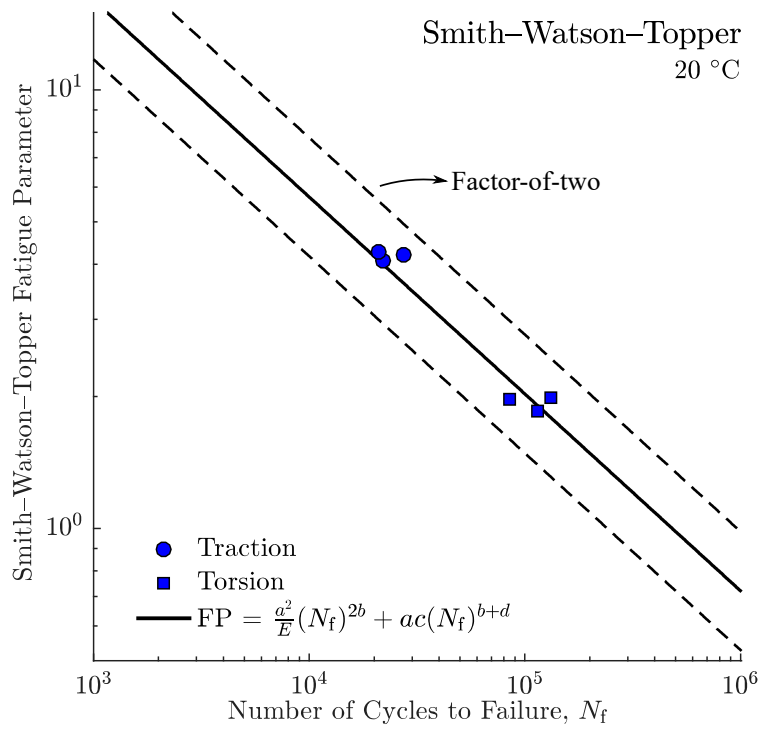


Figure 4.25 Calibration of Smith–Watson–Topper model using room temperature fatigue data.

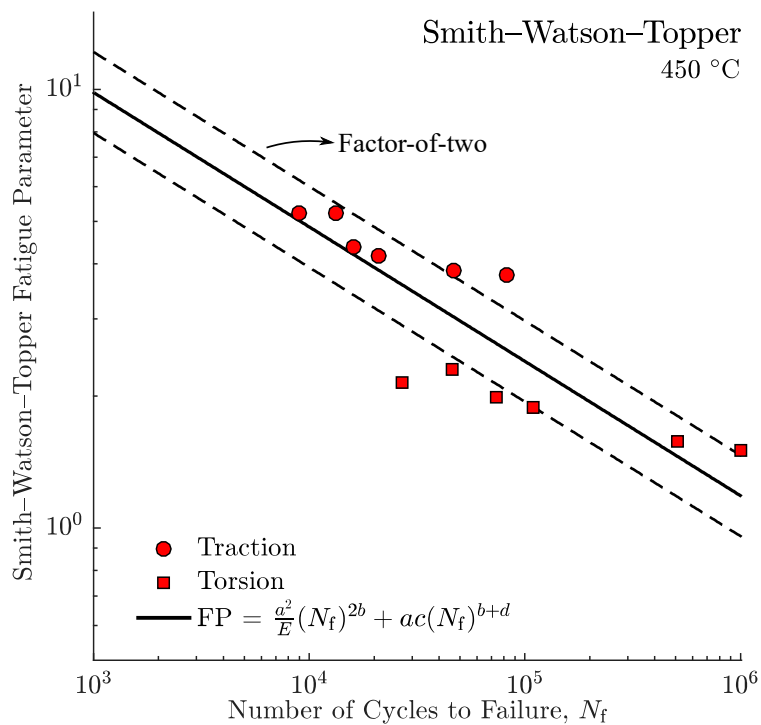


Figure 4.26 Calibration of Smith–Watson–Topper model using high-temperature fatigue data.

4.6.2 Fatigue life predictions

The Fatemi-Socie parameter was used to predict the fatigue life of the proportional tests aiming to assess the robustness of the calibration when simulating different loading conditions. The results are presented in Fig. 4.27, which summarizes, on a plot of observed versus predicted lives, the fatigue life of all tests carried out during the fatigue campaign in comparison with its counterparts estimated with the FS model. Given the loading and temperature conditions imposed in this work, the conclusion is that this fatigue parameter successfully estimates the fatigue life of Inconel 718, a fact confirmed by the observation that all data were within a factor of two boundaries considering tests both at room temperature and 450 °C. It must be highlighted that the proportional loading condition was precisely prescribed using the fitted constants obtained on the calibration process.

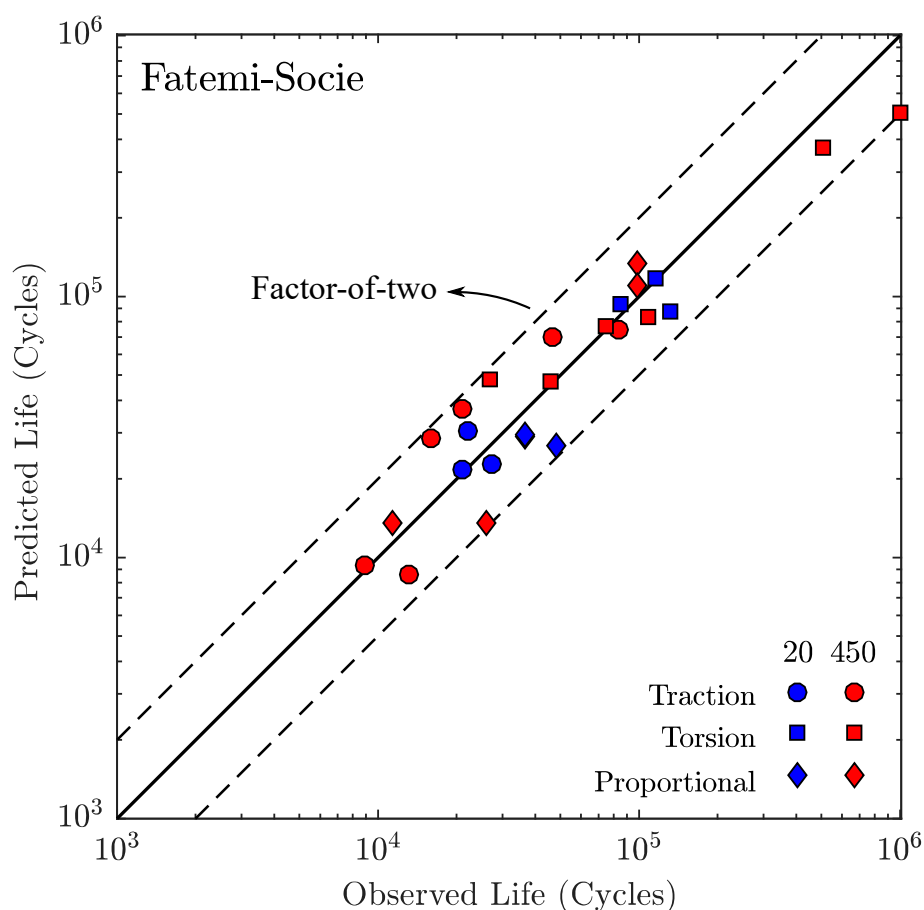


Figure 4.27 Observed lives vs. predictions made using the Fatemi–Socie criterion, considering Inconel 718 test data at room temperature and 450 °C.

The fatigue life of the proportional loading condition was also estimated using the SWT model, as shown in the observed versus predicted life plot presented in Fig. 4.28. Data used

during the calibration process were included. Predictions related to room temperature data were all within a factor of 2, consolidating the effectiveness of this model in describing the fatigue life of Inconel 718 under these test conditions. Regarding the life predictions of the tests conducted at 450 °C, it was observed that the experimental data were more scattered, an expected result considering the calibration of the SWT model under this temperature condition. Still, the life predictions of the high-temperature proportional tests were within a factor 4 when using this fatigue criterion.

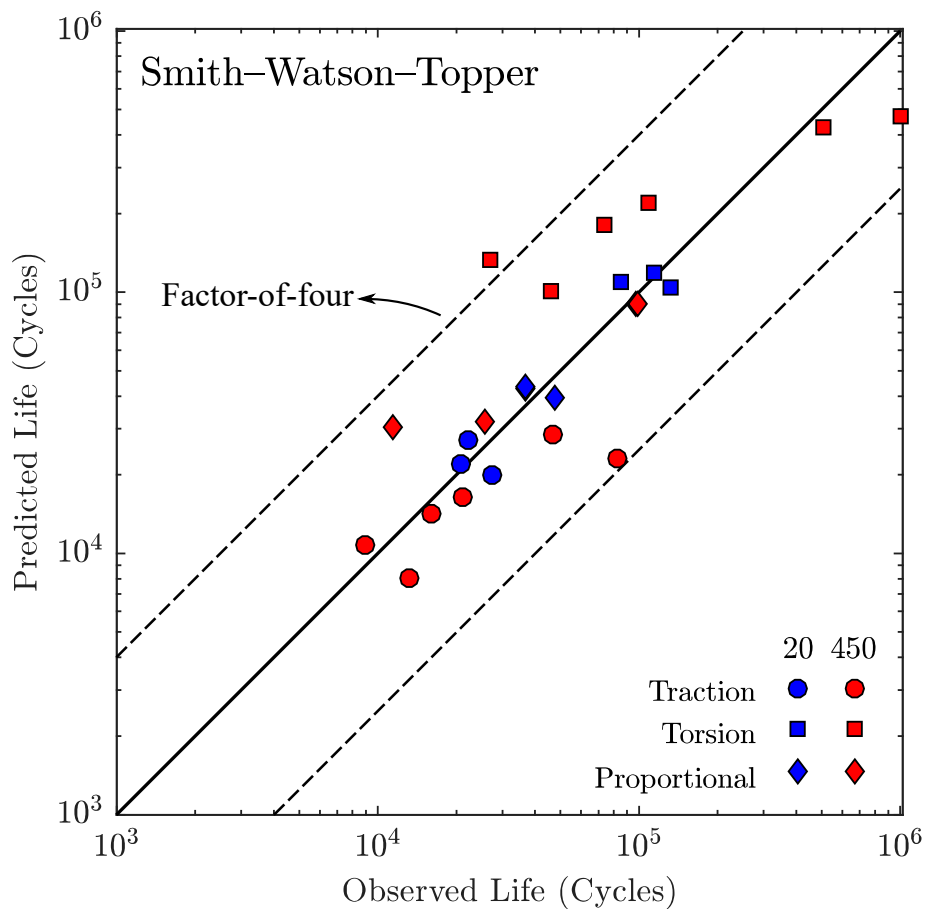


Figure 4.28 Observed lives vs. predictions made using the Smith–Watson–Topper criterion, considering Inconel 718 test data at room temperature and 450 °C.

It is interesting to remember that all tests presented non-null values of mean stress after stabilization. Based on this, a possible justification for the accuracy of life predictions may lie in the fact that both models account for mean stresses effects. Such effects are represented by the maximum normal stress term, which is computed by a sum of the stress amplitude and mean stress components. In addition, note that Inconel 718 predominantly presented shear cracking behavior under the tested conditions considered. The only exception was the traction loading,

which was governed by tensile cracking at both temperatures. In this way, these facts may explain the higher accuracies observed in the life predictions made by the FS model compared to the SWT model since the former assumes the hypothesis that the material fails by Mode II, while the latter considers that the failure occurs by Mode I tensile cracks.

4.6.3 Critical plane orientations

A fatigue criterion based on the critical plane approach must predict not only the fatigue life of a given loading condition but also be consistent in the determination of the plane in which the failure crack nucleates and grows. As introduced earlier, one important hypothesis assumed by Fatemi and Socie during the formulation of their fatigue model was relative to cracking behavior, in which it was considered that the material under analysis fails with shear cracks regardless of the loading condition to which it is submitted. In this sense, it was observed that under pure torsional loading, the maximum shear plane occurs at $\phi = 90^\circ$ and $\theta = 0^\circ$ or $\phi = 90^\circ$ and $\theta = 90^\circ$. For axial loading, it occurs at $\phi = 90^\circ$ and $\theta = \pm 45^\circ$ or $\phi = \pm 45^\circ$ and $\theta = 90^\circ$. On the other hand, the criterion proposed by Smith, Watson, and Topper considers that the material fails by tensile cracks in any situation. For this model, the critical planes in torsional loading occur at $\phi = 90^\circ$ and $\theta = \pm 45^\circ$, while in axial loading, they are observed at $\phi = 90^\circ$ and $\theta = 0^\circ$.

Centered on this and aiming to enrich the evaluation of the FS and SWT models in describing the fatigue behavior of Inconel 718, the critical planes of all tested conditions were estimated using both fatigue criteria. The cracking direction of each loading condition was characterized and presented in section 4.4. However, to validate the estimations made by the models, the directions of the fatigue cracks of the valid tests performed during the fatigue campaign were determined. Photographs of the final crack of each test are shown in Appendix A. Table 4.7 presents the results relative to the observed and estimated directions of the critical plane of all valid fatigue tests. The temperature did not seem to influence the directions of the cracks simulated by the models. As expected, the SWT model precisely predicted the orientation of the cracks in the traction tests, in which tensile cracking was always observed. Moreover, the cracking behavior of the torsion tests was correctly described by the FS parameter, noting that only shear cracks were registered after failure. Finally, it is interesting to note that none of the

models accurately predicted the directions of the proportional tests. That way, despite the good accuracy of the life predictions, neither of the two models correctly predicted the critical plane angles in all tested situations.

Table 4.7 Observed and estimated critical plane directions of the valid tests carried out in the fatigue campaign.

Loading Type	Spec. ID	Temp. [°C]	Observed		FS		SWT	
			ϕ_{obs} [°]	θ_{obs} [°]	ϕ_{FS} [°]	θ_{FS} [°]	ϕ_{SWT} [°]	θ_{SWT} [°]
Traction	7A1	20	90	0	90	40	90	0
	5A2	20	90	0	90	40	90	0
	3D3	20	90	0	90	40	90	0
	5A3	450	90	0	90	-40	90	0
	2C1	450	90	0	90	40	90	0
	4C1	450	90	0	90	40	90	0
	5C2	450	90	0	90	-40	90	0
	2B1	450	90	0	90	-40	90	0
	4C3	450	90	0	90	40	90	0
Torsion	4B1	20	90	90	90	5	90	45
	3D1	20	90	90	90	5	90	45
	4A1	20	90	0	90	5	90	45
	3D2	450	90	90	90	0	90	45
	3B1	450	90	0	90	0	90	45
	9A1	450	90	90	90	85	90	45
	3C1	450	90	0	90	5	90	45
	1B1	450	90	90	90	85	90	45
	3C2	450	90	0	90	5	90	45
Proportional Traction-Torsion	4C2	20	90	90	90	-10	90	30
	7A2	20	90	90	90	-10	90	30
	1C1	20	90	-15	90	-10	90	30
	9A2	450	90	75	90	-10	90	30
	2D1	450	90	0	90	-10	90	30
	1D1	450	90	-15	90	-10	90	30
	4B3	450	90	90	90	-10	90	30

5 | Conclusions

In this work, the fatigue behavior of forged Inconel 718 was investigated under axial/torsional loading conditions at room temperature and 450 °C. The fatigue tests were conducted on thin-walled tubular specimens subjected to traction, torsion, and proportional loading. Scanning electron microscopy analysis was employed to identify the failure mechanism and crack initiation site for each test condition. Fatigue lives and critical plane angles predicted by the Fatemi–Socie criterion and the multiaxial version of the Smith–Watson–Topper parameter were evaluated. The main findings are summarized as follows:

- (1) For a given loading path and equivalent strain amplitude, the fatigue lives of tests at 450 °C were longer than the room temperature tests. The differences observed were up to four times in traction, six times in torsion, and three times in proportional tests. In addition, regardless of the temperature, the longest lives were observed in the torsion tests, followed by the proportional and traction tests in all equivalent strain amplitude tested.
- (2) During the strain-controlled phase, elastic shakedown was observed in all tests after the first loading cycle. The increase of the temperature from 20 to 450 °C resulted in decreases of the Young’s and shear moduli of approximately 10% and 12%, respectively.
- (3) Regardless of the temperature, the cyclic plasticity model proposed by Chaboche successfully simulated the stress-strain behavior of Inconel 718 under all imposed loading conditions. The model was calibrated with traction test data and resulted in deviations in the mean and amplitude components of the equivalent von Mises stress under 5% for the torsion tests and 7% for the proportional tests.
- (4) Mode I tensile cracks were seen in traction tests, while Mode II shear cracks were observed in the torsion and proportional tests. As a consequence, this material presented mixed

cracking behavior under the testing conditions considered. Up to 450 °C, the temperature does not seem to influence the crack direction.

- (5) The fractography analysis revealed that all cracks initiated at inclusions located at the external surface or sub-surface of the specimen, regardless of the applied loading or temperature. Moreover, it was concluded that the transgranular propagation mode was the predominant failure mechanism of the three studied loading paths, regardless of the temperature. Despite that, elements of intergranular fracture were occasionally identified close to the crack initiation site in the proportional tests.
- (6) The Fatemi–Socie and the multiaxial version of the Smith–Watson–Topper fatigue criteria predicted the fatigue life of Inconel 718 within a factor-of-two and a factor-of-four, respectively. The crack directions were also determined by both critical plane models and compared with the orientation of the experimental cracks. The SWT model correctly predicted the crack direction of the traction tests, while the FS model better determined the orientation of the cracks under torsional loading, at room and high-temperature. None of the two models correctly predicted the critical plane angles under all tested loading conditions.

Future Works

Based on the results and discussions presented throughout this work, we would like to suggest some future works that are described in the following topics:

- (1) To predict fatigue life and critical planes using a fatigue model that accounts for different cracking behavior, including mixed mode, like the model proposed by Jiang [65].
- (2) To finish SEM analysis for the remaining specimens to determine whether the cracking initiation site of all tests was in carbides.
- (3) To investigate the size distribution of the inclusions, assessing whether the largest precipitates located on the outer surface of the specimens were responsible for initiating the failure crack.

References

- [1] C. SIMS. “A history of superalloy metallurgy for superalloy metallurgists.” In: *Superalloys* (1984), pp. 399–419.
- [2] J. BARKER. *The Initial Years of Alloy 718: A GE Perspective*. Tech. rep. 1989. DOI: 10.7449/1989/superalloys_1989_269_277.
- [3] A. LINGENFELTER. “Welding of Inconel Alloy 718: A Historical Overview.” In: *Superalloy 718: Metallurgy and Applications* (1989), pp. 673–683.
- [4] P. STURESSON. “Sense , Actuate and Survive Ceramic Microsystems for High-Temperature.” PhD thesis. Uppsala University, 2018.
- [5] A. THAKUR and S. GANGOPADHYAY. “State-of-the-art in surface integrity in machining of nickel-based super alloys.” In: *International Journal of Machine Tools and Manufacture* 100 (2016), pp. 25–54. DOI: 10.1016/j.ijmachtools.2015.10.001.
- [6] H. F. MERRICK. “Low Cycle Fatigue of Three Wrought Nickel-Base Alloys.” In: *Metall Trans* 5.4 (1974), pp. 891–897. DOI: 10.1007/BF02643144.
- [7] D. FOURNIER and A. PINEAU. “Low cycle fatigue behavior of Inconel 718 at 298 K and 823 K.” In: *Metallurgical Transactions A* 8.7 (1977), pp. 1095–1105. DOI: 10.1007/BF02667395.
- [8] T. H. SANDERS, R. E. FRISHMUTH, and G. T. EMBLEY. “Temperature Dependent Deformation Mechanisms of Alloy 718 in Low Cycle Fatigue.” In: *Metallurgical transactions. A, Physical metallurgy and materials science* 12 A.6 (1981), pp. 1003–1010. DOI: 10.1007/BF02643481.
- [9] T. S. COOK. “Stress-strain behavior of Inconel 718 during low cycle fatigue.” In: *Journal of Engineering Materials and Technology, Transactions of the ASME* 104.3 (1982), pp. 186–191. DOI: 10.1115/1.3225063.
- [10] D. WORTHEM, F. ROBERTSON, F. LECKIE, D. SOCIE, and C. ALTSTETTER. “Inhomogeneous Deformation in INCONEL 718 during Monotonic and Cyclic Loadings.” In: *Metallurgical Transactions A* 21A (Dec. 1990), pp. 3215–3220.
- [11] K. RAO, S. KALLURI, G. HALFORD, and M. MCGAW. “Serrated Flow and Deformation Substructure at Room Temperature in Inconel 718 Superalloy During Strain Controlled Fatigue.” In: *Scripta Metallurgica et Materialia* 32.4 (1995), pp. 493–498.

- [12] J. WARREN and D. Y. WEI. “The cyclic fatigue behavior of direct age 718 at 149, 315, 454 and 538 °C.” In: *Materials Science and Engineering A* 428.1-2 (2006), pp. 106–115. DOI: 10.1016/j.msea.2006.04.091.
- [13] H. MADERBACHER, B. OBERWINKLER, H. P. GÄNSER, W. TAN, M. ROLLETT, and M. STOSCHKA. “The influence of microstructure and operating temperature on the fatigue endurance of hot forged Inconel® 718 components.” In: *Materials Science and Engineering A* 585 (2013), pp. 123–131. DOI: 10.1016/j.msea.2013.07.053.
- [14] K. PRASAD, R. SARKAR, P. GHOSAL, V. KUMAR, and M. SUNDARARAMAN. “High temperature low cycle fatigue deformation behaviour of forged IN 718 superalloy turbine disc.” In: *Materials Science and Engineering A* 568 (2013), pp. 239–245. DOI: 10.1016/j.msea.2012.12.069.
- [15] Z. HUANG, W. DENG, J. XU, Y. HU, and L. JIANG. “Isothermal and thermomechanical fatigue behavior of Inconel 718 superalloy.” In: *Materials Science and Engineering A* 742 (2019), pp. 813–819. DOI: 10.1016/j.msea.2018.11.052.
- [16] D. SOCIE, L. WAILL, and D. DITTMER. “Biaxial Fatigue of Inconel 718 Including Mean Stress Effects.” In: *Biaxial/Multiaxial Fatigue, eds. Miller and Brown, ASTM, STP 853* (1984), pp. 463–481.
- [17] D. F. SOCIE and T. W. SHIELD. “Mean stress effects in biaxial fatigue of Inconel 718.” In: *Journal of Engineering Materials and Technology, Transactions of the ASME* 106.3 (1984), pp. 227–232. DOI: 10.1115/1.3225707.
- [18] D. SOCIE, P. KURATH, and J. KOCH. “A Multiaxial Fatigue Damage Parameter.” In: *Biaxial and Multiaxial Fatigue, EGF 3 (Edited by Miller, K. and Brown, M.)* (1989), pp. 535–550.
- [19] A. FATEMI and D. F. SOCIE. “A Critical Plane Approach To Multiaxial Fatigue Damage Including Out-of-Phase Loading.” In: *Fatigue & Fracture of Engineering Materials & Structures* 11.3 (1988), pp. 149–165. DOI: 10.1111/j.1460-2695.1988.tb01169.x.
- [20] A. FATEMI and P. KURATH. “Multiaxial Fatigue Life Predictions Under the Influence of Mean-Stresses.” In: *Journal of Engineering Materials and Technology, Transactions of the ASME* 110 (1988), pp. 380–388.
- [21] J. SUN and H. YUAN. “Life assessment of multiaxial thermomechanical fatigue of a nickel-based superalloy Inconel 718.” In: *International Journal of Fatigue* 120.November 2018 (2019), pp. 228–240. DOI: 10.1016/j.ijfatigue.2018.11.018.
- [22] D. PETERSEN, R. LINK, C. GIL, C. LISSENDEN, and B. LERCH. “Yield of Inconel 718 by Axial-Torsional Loading at Temperatures up to 649°C.” In: *Journal of Testing and Evaluation* 27.5 (1999), p. 327. DOI: 10.1520/jte12233j.

- [23] M. FILIPPINI, S. FOLETTI, and G. PASQUERO. “Assessment of multiaxial fatigue life prediction methodologies for Inconel 718.” In: *Procedia Engineering* 2.1 (2010), pp. 2347–2356. DOI: 10.1016/j.proeng.2010.03.251.
- [24] H. KIM, K. S. KIM, and H. PARK. “Ratcheting Behavior of Inconel 718 at 649°C under Multiaxial Loading.” In: *Journal of Solid Mechanics and Materials Engineering* 4.1 (2010), pp. 39–50. DOI: 10.1299/jmmp.4.39.
- [25] J. L. CHABOCHE. “Time-independent constitutive theories for cyclic plasticity.” In: *International Journal of Plasticity* 2 (1986), pp. 149–188.
- [26] K. K. SMITH, P. WATSON, T. H. TOPPER, and P. WATSON. “Stress-Strain Function for the Fatigue of Metals.” In: *Journal of Materials* 5 (1970), pp. 767–778.
- [27] D. SOCIE. “Multiaxial Fatigue Damage Models.” In: *Journal of Engineering Materials and Technology* 109.4 (1987), p. 293. DOI: 10.1115/1.3225980.
- [28] AMS. “Nickel Alloy, Corrosion and Heat-Resistance, Bars, Forgings, and Rings.” In: *SAE Aerospace* (2004), pp. 1–11.
- [29] J. SUN and H. YUAN. “Cyclic plasticity modeling of nickel-based superalloy Inconel 718 under multi-axial thermo-mechanical fatigue loading conditions.” In: *International Journal of Fatigue* 119.September 2018 (2019), pp. 89–101. DOI: 10.1016/j.ijfatigue.2018.09.017.
- [30] M. J. DONACHIE and S. J. DONACHIE. *Superalloys: a technical guide*. ASM International, 2002.
- [31] D. PAULONIS, J. OBLAK, and D. DUVALL. “Precipitation in Nickel-base Alloy 718.” In: *American Society for Metals* 62 (1969), pp. 611–622.
- [32] J. COLLIER, S. WONG, J. PHILLIPS, and J. TIEN. “The Effect of Varying Al, Ti, and Nb Content on the Phase Stability of INCONEL 718.” In: *Metallurgical Transactions A* 19 (1988), pp. 1657–1666.
- [33] A. CHAMANFAR, L. SARRAT, M. JAHAZI, M. ASADI, A. WECK, and A. KOUL. “Microstructural characteristics of forged and heat treated Inconel-718 disks.” In: *Materials and Design* 52 (2013), pp. 791–800.
- [34] S. AZADIAN, L. WEI, and R. WARREN. “Delta phase precipitation in Inconel 718.” In: *Materials Characterization* 53 (2004), pp. 7–16. DOI: 10.1016/j.matchar.2004.07.004.
- [35] X. XIE, J. DONG, G. WANG, and W. YOU. “The Effect of Nb, Ti, Al on Precipitation and Strengthening Behavior of 718 Type Superalloys.” In: *Superalloys 718,625,706 and Various Derivatives* (2005), pp. 287–298.
- [36] B. PIERAGGI and J. UGINET. “Fatigue and Creep Properties in Relation with Alloy 718 Microstructure.” In: *Superalloys 718,625,706 and Various Derivatives* (1994), pp. 535–544.

- [37] B. LI, J. ZHUANG, J. YANG, Q. DENG, and J. DU. “The Effect of δ -phase on Crack Propagation Under Creep and Fatigue Conditions in Alloy 718.” In: *Superalloys 718,625,706 and Various Derivatives* (1994), pp. 545–555.
- [38] J. BELAN. “High frequency fatigue test of IN 718 alloy – microstructure and fractography evaluation.” In: *Metallurgija* 54 (2015), pp. 59–62.
- [39] M. SUNDARARAMAN, P. MUKHOPADHYAY, and S. BANERJEE. “Carbide Precipitation in Nickel Base Superalloys 718 and 625 and Their Effect on Mechanical Properties.” In: *Superalloys 718,625,706 and Various Derivatives* (1997), pp. 367–378.
- [40] C. KUO, Y. YANG, H. BOR, C. WEI, and C. TAI. “Aging effects on the microstructure and creep behavior of Inconel 718 superalloy.” In: *Materials Science and Engineering A* 510-511 (2009), pp. 289–294. DOI: 10.1016/j.msea.2008.04.097.
- [41] M. CIESLAK, G. KNOROVSKY, T. HEADLEY, and A. ROMIG. “The Solidification Metallurgy of Alloy 718 and Other Nb-Containing Superalloys.” In: *Superalloy 718: Metallurgy and Applications* (1989), pp. 59–68.
- [42] J. SCHIRRA, R. CALESS, and R. HATALA. “The Effect of Laves Phase on the Mechanical Properties of Wrought and Cast + HIP Inconel 718.” In: *Superalloys 718,625 and Various Derivatives* (1991), pp. 375–388.
- [43] F. LIU, F. LYU, F. LIU, X. LIN, and C. HUANG. “Laves phase control of Inconel 718 superalloy fabricated by laser direct energy deposition via δ aging and solution treatment.” In: *Journal of Materials Research and Technology* 9 (2020), pp. 9753–9765. DOI: 10.1016/j.jmrt.2020.06.061.
- [44] F. KANDIL, M. BROWN, and K. MILLER. “Biaxial low-cycle fatigue failure of 316 stainless steel at elevated temperatures.” In: *The Metals Society* 280 (1982), pp. 203–210.
- [45] M. BROWN and K. MILLER. “A theory for fatigue failure under multiaxial stress-strain conditions.” In: *Proceedings of the Institution of Mechanical Engineers* 187.1 (1973), pp. 745–755.
- [46] B. PIERAGGI and J. UGINET. “A Method Based on Virtual Strain-Energy Parameters for Multiaxial Fatigue Life Prediction.” In: *Advances in Multiaxial Fatigue* STP 1191 (1993), pp. 67–84. DOI: 10.1520/STP24796S.
- [47] ASTM. “E2207 - Standard Practice for Strain-Controlled Axial-Torsional Fatigue Testing with Thin-Walled Tubular Specimens.” In: *ASTM International* (2013), pp. 1–8.
- [48] ASM. *Metallography and Microstructures*. Vol. 9. ASM International, 2004.
- [49] ASTM. “E112 - Standard Test Methods for Determining Average Grain Size.” In: *ASTM International* (2013), pp. 1–28.
- [50] S. FLOREEN, F. GERHARD, and Y. WALTER. “The Metallurgy of Alloy 625.” In: *Superalloys 718,625,706 and Various Derivatives* (1994), pp. 13–37.

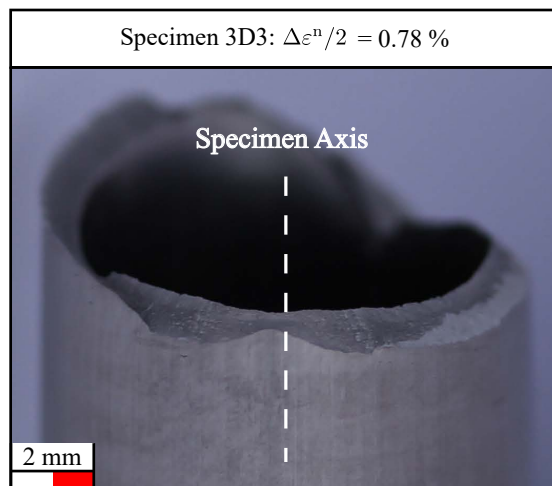
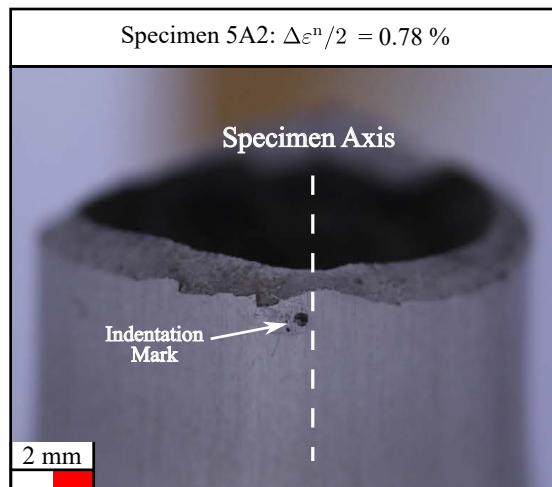
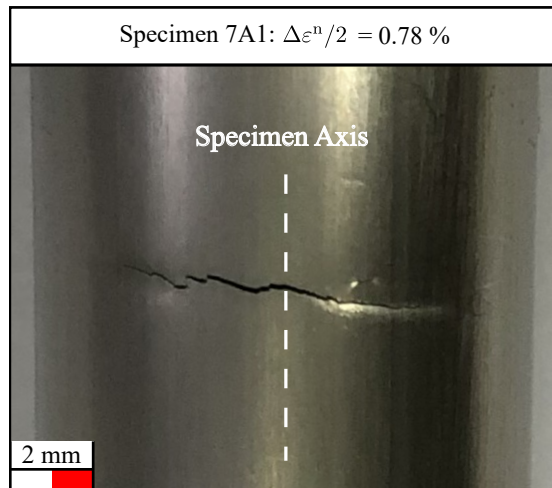
- [51] T. CONNOLLEY, P. REED, and M. STARINK. “Short crack initiation and growth at 600 °C in notched specimens of Inconel 718.” In: *Material Science and Engineering A* 340 (2003), pp. 139–154.
- [52] C. BEMFICA, L. CARNEIRO, E. N. MAMIYA, and F. C. CASTRO. “Fatigue and cyclic plasticity of 304L stainless steel under axial-torsional loading at room temperature.” In: *International Journal of Fatigue* 125 (Aug. 2019), pp. 349–361. DOI: 10.1016/j.ijfatigue.2019.04.009.
- [53] S. KALNAUS and Y. JIANG. “Fatigue of AL6XN stainless steel.” In: *Journal of Engineering Materials and Technology, Transactions of the ASME* 130.3 (2008), pp. 0310131–03101312. DOI: 10.1115/1.2931154.
- [54] D. GUSTAFSSON, J. J. MOVERARE, K. SIMONSSON, and S. SJÖSTRÖM. “Modeling of the constitutive behavior of Inconel 718 at intermediate temperatures.” In: *Journal of Engineering for Gas Turbines and Power* 133.9 (2011), pp. 1–4. DOI: 10.1115/1.4002913.
- [55] M. ALGARNI, Y. CHOI, and Y. BAI. “A unified material model for multiaxial ductile fracture and extremely low cycle fatigue of Inconel 718.” In: *International Journal of Fatigue* 96 (2017), pp. 162–177. DOI: 10.1016/j.ijfatigue.2016.11.033.
- [56] J. L. CHABOCHE, K. DAN VAN, and G. CORDIER. “Modelization of the strain memory effect on the cyclic hardening of 316 stainless steel.” In: *Transactions of the International Conference on Structural Mechanics in Reactor Technology L* (1979).
- [57] P. ARMSTRONG and C. FREDERICK. “A Mathematical Representation of the Multiaxial Bauschinger Effect.” In: 731 (1966).
- [58] G. SUDARSHAN, J. SHARMA, K. THARIAN, P. RAMESH, K. SREEKUMAR, and P. SINHA. “Study of LCF Behavior of IN718 Superalloy at Room Temperature.” In: *Materials Science Forum* 710 (2012), pp. 445–450. DOI: 10.4028/www.scientific.net/MSF.710.445.
- [59] Y. JIANG, O. HERTEL, and M. VORMWALD. “An experimental evaluation of three critical plane multiaxial fatigue criteria.” In: *International Journal of Fatigue* 29.8 (Aug. 2007), pp. 1490–1502. DOI: 10.1016/j.ijfatigue.2006.10.028.
- [60] A. FATEMI and N. SHAMSAEI. “Multiaxial fatigue: An overview and some approximation models for life estimation.” In: *International Journal of Fatigue* 33 (2011), pp. 948–958. DOI: 10.1016/j.ijfatigue.2011.01.003.
- [61] Y. FAYMAN. “Microstructural Characterization and Elemental Partitioning in a Direct-aged Superalloy (DA 718).” In: *Materials Science and Engineering* 92 (1987), pp. 159–171.
- [62] D. F. SOCIE and G. B. MARQUIS. *Multiaxial Fatigue*. Society of Automotive Engineers, 1997. DOI: 10.1016/B0-08-043749-4/04030-1.

- [63] A. PINEAU, S. DEYBER, and F. ALEXANDRE. “Modelling the optimum grain size on the low cycle fatigue life of a Ni based superalloy in the presence of two possible crack initiation sites.” In: *Scripta Materialia* 50 (2004), pp. 25–30. DOI: 10.1016/j.scriptamat.2003.09.043.
- [64] M. CLAVEL and A. PINEAU. “Frequency and Wave-Form Effects on the Fatigue Crack Growth Behavior of Alloy 718 At 298 K and 823 K.” In: *Metall Trans A* 9 A.4 (1978), pp. 471–480. DOI: 10.1007/BF02646402.
- [65] Y. JIANG. “Fatigue criterion for general multiaxial loading.” In: *Fatigue and Fracture of Engineering Materials and Structures* 23.1 (Jan. 2000), pp. 19–32. DOI: 10.1046/j.1460-2695.2000.00247.x.

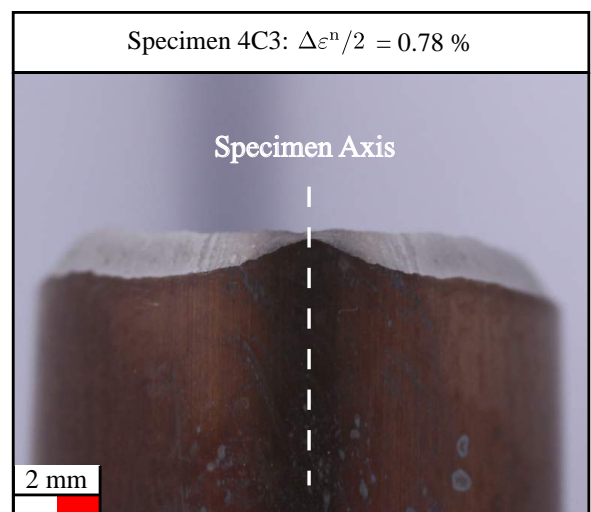
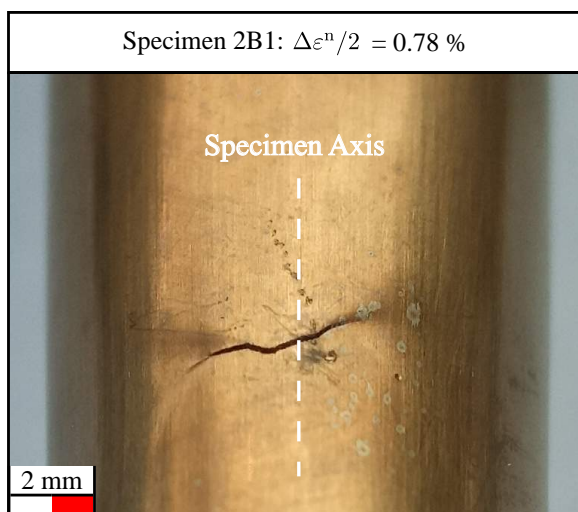
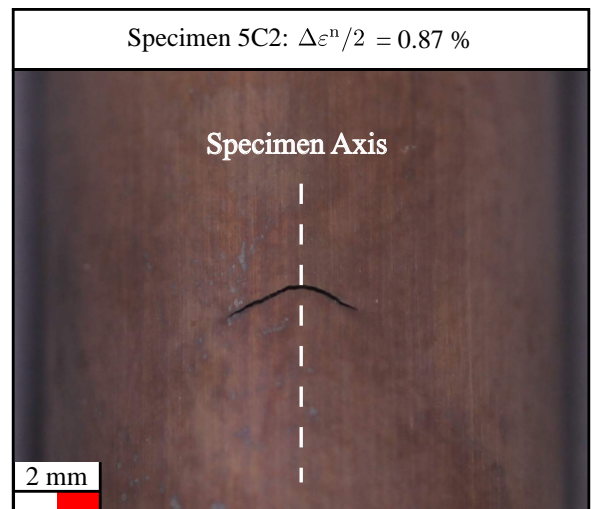
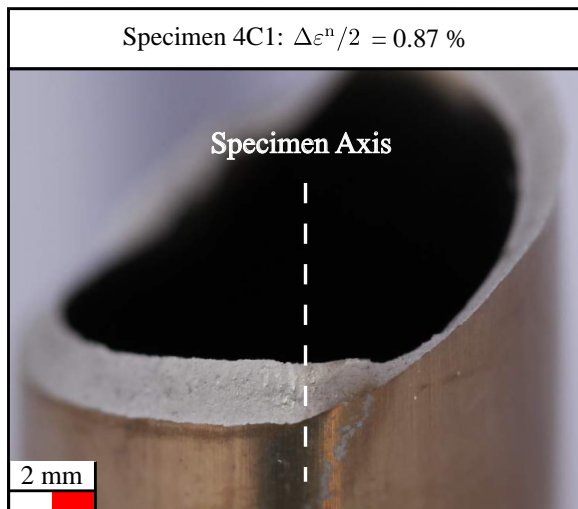
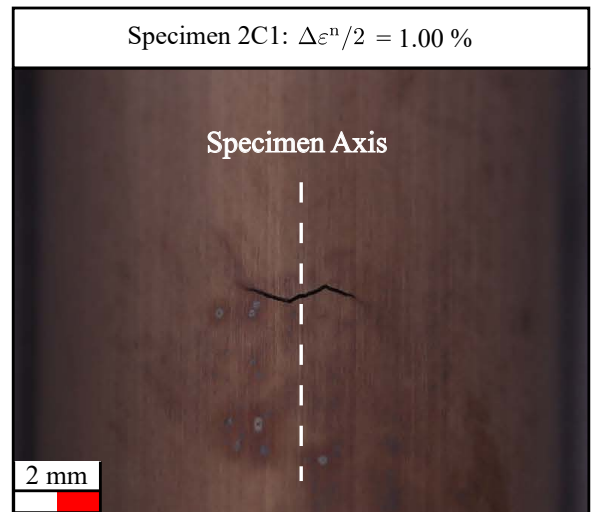
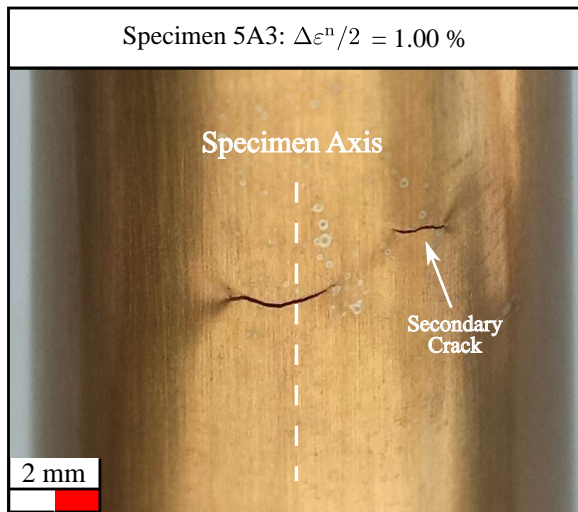
Appendices

A | Observed Fatigue Cracks

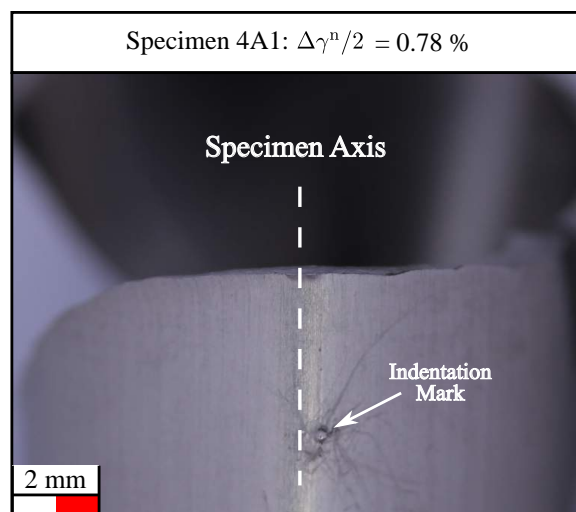
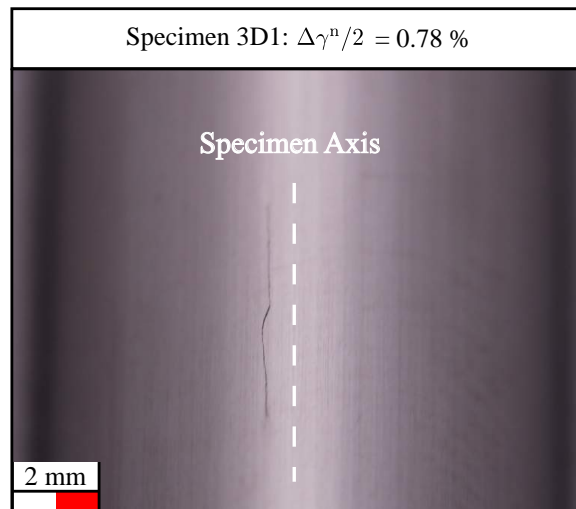
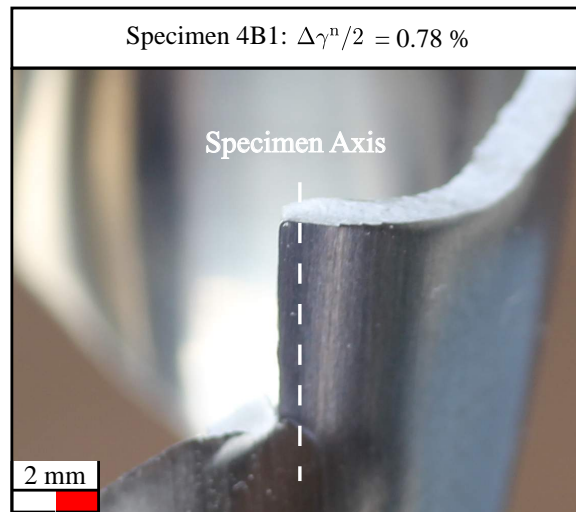
A.1 Traction, 20 °C



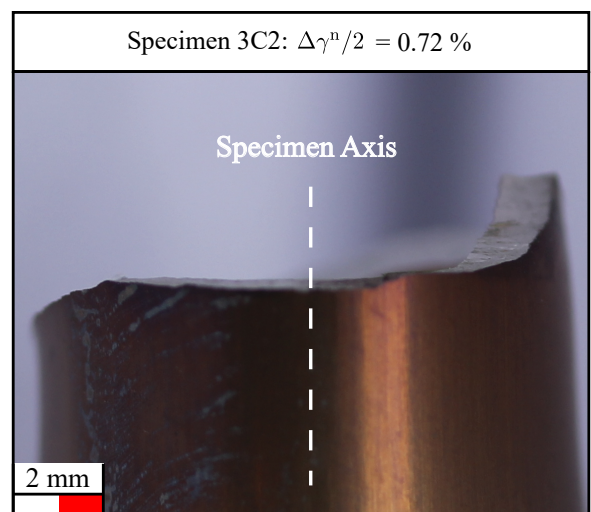
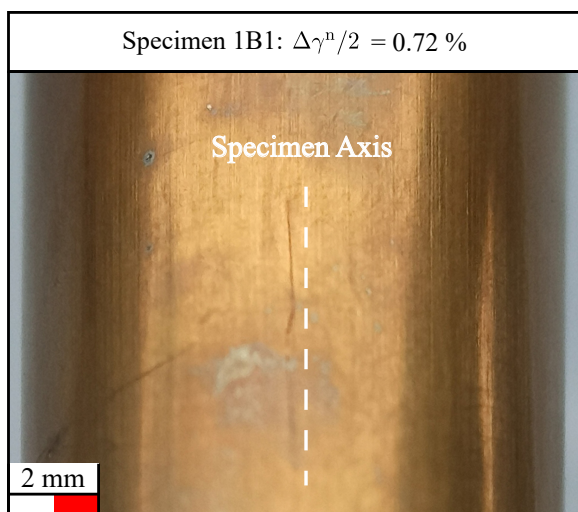
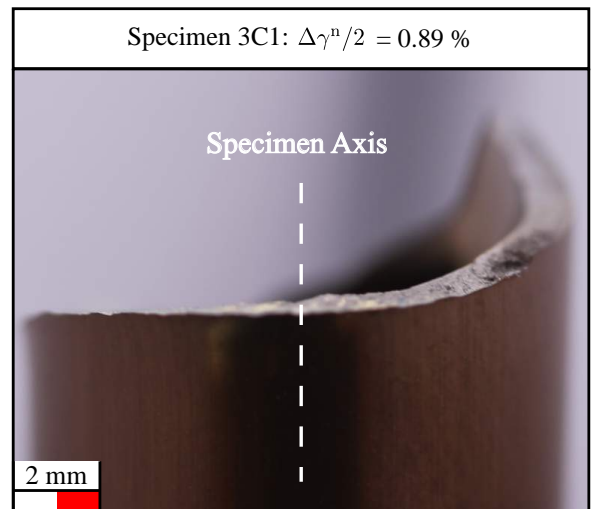
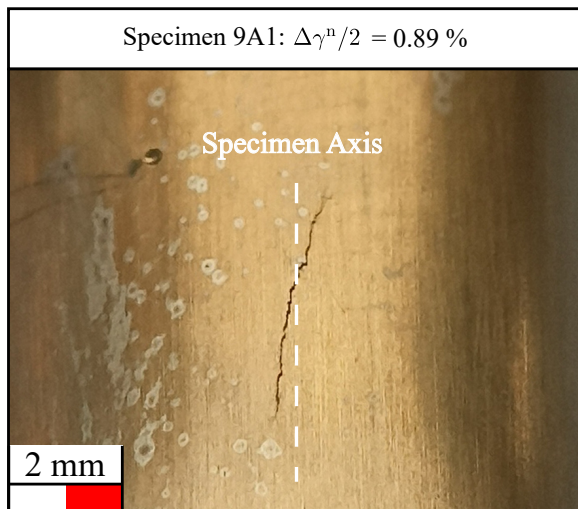
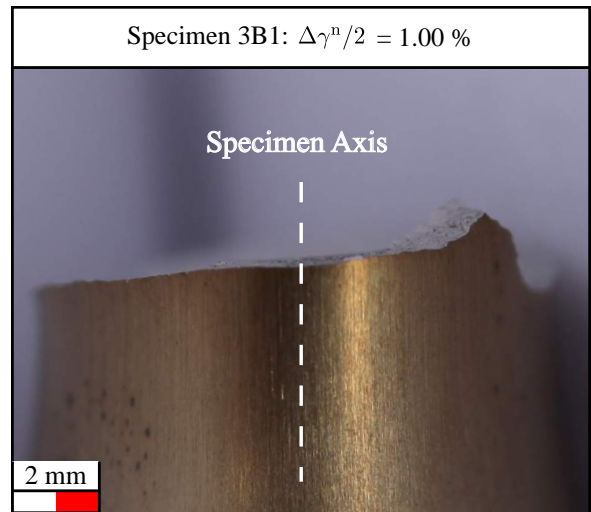
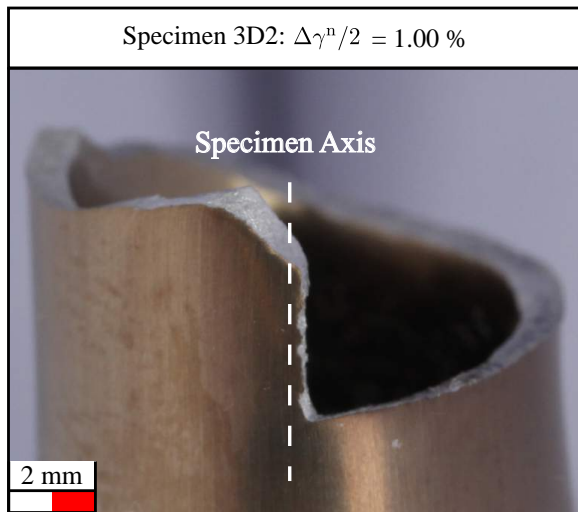
A.2 Traction, 450 °C



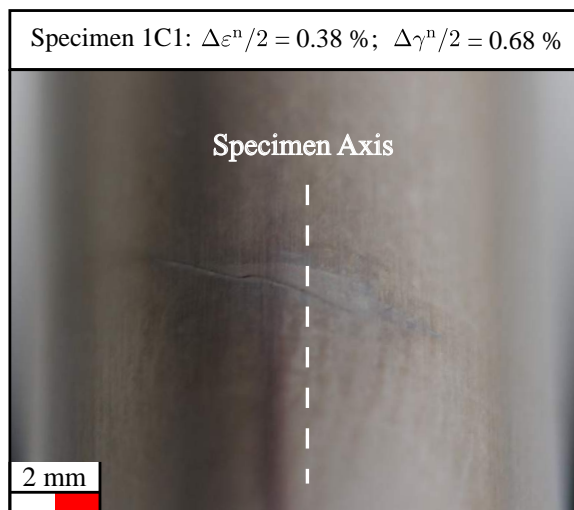
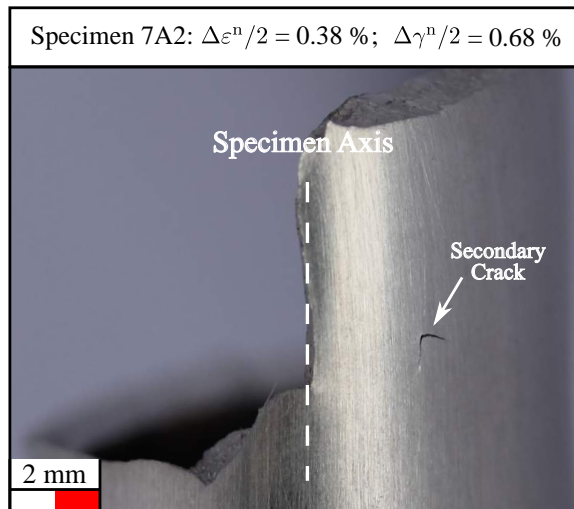
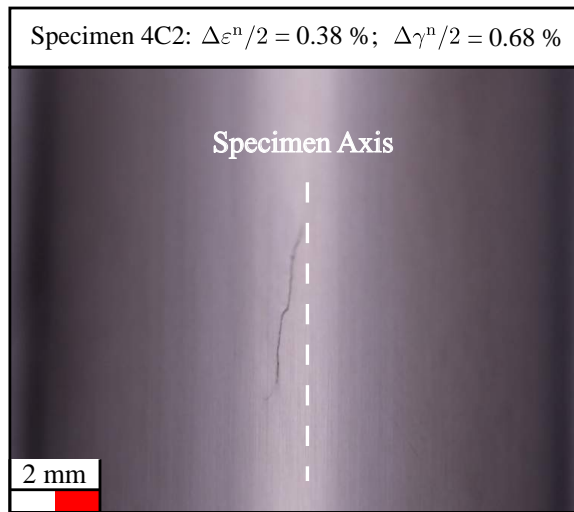
A.3 Torsion, 20 °C



A.4 Torsion, 450 °C



A.5 Proportional, 20 °C



A.6 Proportional, 450 °C

